Photonic Structures for Systems with Silicon Solar Cells and Upconverters

Dissertation submitted for the degree of Doctor of Natural Sciences
Dr. rer. nat.

Presented by
Barbara Herter

at the

Universität Konstanz

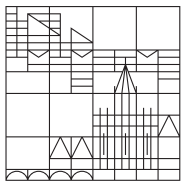

Faculty of Sciences
Department of Physics

Date of the oral examination:	18.07.2014
First referee:	Prof. Dr. Gerhard Willeke
Second referee:	Prof. Dr. Elke Scheer

This dissertation was elaborated at the
Fraunhofer Institut für Solare Energiesysteme,
Freiburg im Breisgau, Germany.

Contents

List of Figures

List of Tables

Abstract

Within the scope of this work photonic structures were developed for systems combining solar cells and upconverters. The approaches can be separated into two different categories: the use of photonic structures as filter structures for light-guiding as well as the embedding of upconverter material directly into photonic structures are investigated.

For the light-guiding approach, filter structures were simulated with the transfer matrix approach and optimized by applying an evolutionary algorithm. The optimized structures as well as Bragg-structures were fabricated based on amorphous silicon carbide. Within this material system, the refractive index can be tuned with the silicon to carbon ratio. The layers were deposited by plasma-enhanced chemical vapor deposition based on either coupled microwave and radio frequency processes or on pulsed microwave processes. Using these processes, filters with reflectances above 95 % and transmittances in the range of 85 % - 90 % were produced in the respective spectral regions.

For the second approach, upconversion processes are influenced by two different mechanisms. First, the local irradiance for the absorption wavelength at 1523 nm is varied and can be increased at the upconverter positions; and second, the local density of photonic states is altered, influencing

the spontaneous emission probabilities. These two influences were quantified in simulations and accounted for in a rate-equation model for the upconverter β-$NaYF_4$:Er^{3+}. Using this model, the effects of the photonic structure environment on the upconversion processes were investigated for four different structures: a cavity structure, an interdigitated Bragg-structure, a grating structure and a grating-waveguide structure. For all structures, considerable improvements in the upconversion luminescence and quantum yield could be achieved for optimized parameters.

Subsequently, the optimized cavity and grating structures were produced using β-$NaYF_4$:25 % Er^{3+}-nanoparticles embedded in poly-methylmethacrylate. For the cavity structure, the luminescence could be increased by a factor of 1.8 under monochromatic excitation at a wavelength of 1523 nm with an irradiance of 4337 W/m^2. For the optimized linear grating structure, an even higher luminescence enhancement of 3.1 could be achieved. The trend of the luminescence enhancement is very well predicted by the simulations.

Within this work, a first combined simulation approach has been developed to quantify the effects of a photonic structure environment on upconversion processes. Using this model system, structure parameters could be optimized and these optimized structures could be realized using a material similar to the one described by the rate-equation model. Within these structures, a considerable increase in the luminescence signal could be shown.

Zusammenfassung

In dieser Arbeit wurden photonische Strukturen für zwei unterschiedliche Ansätze untersucht: zum einen der Einsatz photonischer Strukturen als Filter für ein System, das Hochkonvertermaterialien mit einer Siliciumsolarzelle verbindet, zum anderen der direkte Einbau von Hochkonvertermaterialien in photonische Strukturen.

Für den ersten Ansatz wurden Schichten aus amorphem Siliciumkarbid mittels plasmaunterstützter Gasphasenabscheidung hergestellt. In diesem Materialsystem lässt sich der Brechungsindex mit dem Verhältnis von Silicium zu Kohlenstoff einstellen. Für die Abscheidung wurden sowohl gekoppelte Hochfrequenz- und Mikrowellenprozesse als auch gepulste Mikrowellenprozesse verwendet. Die Filter wurden mit der Transfermatrix-Methode simuliert. Hierbei wurden die Schichtdicken durch einen evolutionären Algorithmus angepasst, um die Filtereigenschaften zu verbessern. Mit diesen Methoden konnten Filterstrukturen hergestellt werden, die eine Reflexion von über 95 % sowie eine Transmission von $85 - 90$ % in den entsprechenden Wellenlängenbereichen zeigten.

Für den zweiten Ansatz wurde der Einfluss von photonischen Strukturen auf den Hochkonversionsprozess selbst untersucht. Die Einbettung in photonische Strukturen bewirkt beeinflusst den Prozess auf zwei Arten: die lokale Bestrahlungsstärke wird durch die photonische Struktur variiert;

zusätzlich wird die lokale photonische Zustandsdichte verändert, wodurch die spontanen Emissionswahrscheinlichkeiten beeinflusst werden. Mithilfe von Simulationen wurden diese Effekte quantifiziert und in einem Ratengleichungsmodell für den Hochkonverter β-$NaYF_4$:25 % Er^{3+} berücksichtigt. Mithilfe dieses Ansatzes war es möglich, den Einfluss der photonischen Struktur auf die Hochkonversions-Lumineszenz, sowie die Hochkonversions-Quantenausbeute zu quantifizieren. Hierbei wurden unterschiedliche Strukturen untersucht: eine eindimensionale Resonatorstruktur, eine Doppelbragg-Struktur, eine Gitter-Struktur sowie eine Gitter-Wellenleiterstruktur. Die Parameter dieser Strukturen konnten mithilfe der Simulationen optimiert werden. Am vielversprechendsten zeigten sich die Resonatorstruktur und die Gitter-Struktur.

Diese wurden im nächsten Schritt mit optimierten Strukturparametern hergestellt. Hierfür wurden Hochkonverter-Nanopartikel in Polymethylmethacrylat eingebettet. Für eine monochromatische Bestrahlung bei einer Wellenlänge von 1523 nm unter einer Bestrahlungsstärke von 4337 W/m^2 konnte für die Resonatorstruktur eine Lumineszenzerhöhung um den Faktor 1.8 gemessen werden. Für die optimierte Gitterstruktur konnte die Lumineszenz bei gleicher Bestrahlungsstärke sogar um einen Faktor 3.1 erhöht werden. Der Trend der gemessenen Lumineszenzerhöhung konnte sehr gut durch die Simulationsergebnisse reproduziert werden.

Im Rahmen dieser Arbeit wurde eine Simulationsmethode entwickelt, die es ermöglicht, die Effekte einer photonischen Struktur auf darin eingebettete Hochkonverter zu quantifizieren. Mithilfe dieses Ansatzes, konnten die Parameter der photonischen Strukturen optimiert werden. Zudem konnten die so optimierten Strukturen hergestellt werden. Es wurde gezeigt, dass die Hochkonverter-Lumineszenz durch diese Strukturen erheblich erhöht werden kann.

1 Introduction

1.1 Motivation

Since the beginning of the Industrial Revolution in the 19$^{\text{th}}$ century, fossil fuels like oil, coal and gas are the main sources of energy. This has two main disadvantages. First of all, these energy sources have been built for millions of years and are therefore limited. Even according to British petrol (BP), the oil reserves known at the end of 2012 will only cover the oil production for another 52.9 years [1]. Second, the combustion of all these materials has led to an enormous increase in the emission of greenhouse gases, mainly of carbon dioxide (CO_2) into the atmosphere. These greenhouse gases are responsible for global warming [2]. Between 1880 and 2012, the global temperature rose by 0.85 °C (0.65 °C to 1.06 °C) [2].

According to the international energy agency (IEA), the global energy consumption per capita will rise by another 30 % between 2011 and 2035 [3]. To cover this increase in energy demands, a mix of renewable energy sources is required, whereupon photovoltaics as the only technology which directly converts our primary source of energy, the solar radiation, into electricity, plays a major role. Comparing the energy emitted by the sun

to the amount of primary energy consumed on earth, it has been found that the emission of solar irradiance coming from only $0.2\,\mathrm{km}^2$ of the sun's surface covers the global energy needs [4]. Looking at Germany in 2013, 29.7 TWh of energy have been produced by photovoltaics. This already amounts to 5.3 % of the total net-electricity consumption [5].

The power generation in a solar cell is based on the excitation of an electron from a valence band and a conduction band. The difference between these two bands, the so-called band gap provides a limit for the maximum separation of the quasi-Fermi-levels [6]. Only photons with energies above the band gap energy can contribute to the current produced by the cell, thus, the lower the band gap energy the higher the maximum short-circuit current. On the other hand, the smaller the band gap, the smaller the potential for the separation of the quasi Fermi levels and with this splitting, the open-circuit voltage. In consequence, there is a trade-off between potential open-circuit voltage and short-circuit current.

The solar spectrum covers a very broad wavelength range, hence, only a small fraction of photons have exactly the amount of energy that is required to overcome the band gap of a specific semiconductor material. However, these photons are the ones that are most efficiently used in a solar cell, all photons with lower energy (larger wavelength) can not contribute to the current generation and photons with higher energy (smaller wavelength) do contribute to the current generation, but their additional energy is lost by thermalization. These two loss mechanisms and their importance for a silicon solar cell under illumination with the AM1.5G solar spectrum are shown in Figure 1.1.

Considering these loss mechanisms and radiative recombination, in 1961 Shockley and Queisser investigated the theoretical efficiency maximum for a single junction solar cell with arbitrary band gap under black-body radiation in a thermodynamic approach [7]. They found a maximum efficiency

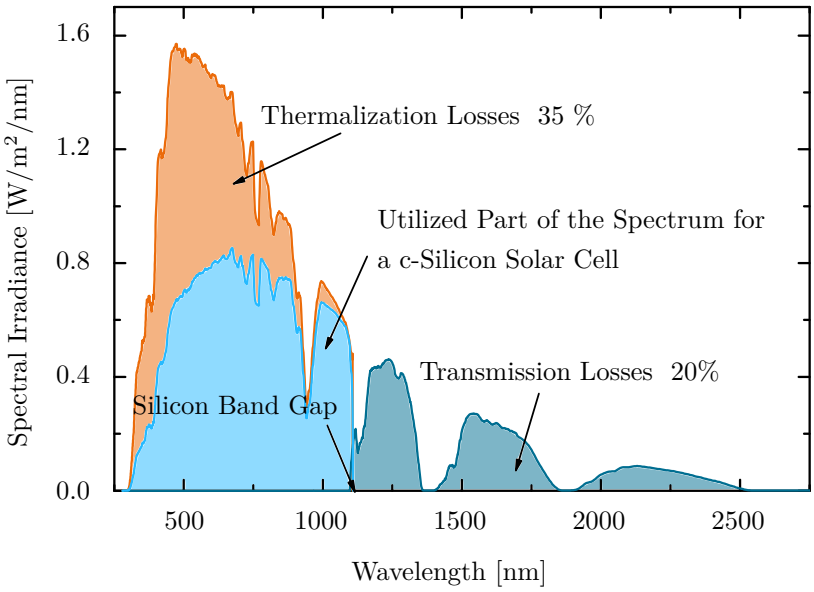

Figure 1.1: AM1.5G spectrum and sketch of the part of the spectrum that can be utilized by a crystalline silicon solar cell, whereas the orange part of the spectrum is lost by thermalization. The dark blue part is not absorbed by the silicon.

of 30% for an optimal band gap of 1.1 eV. Crystalline silicon, with its band gap of 1.12 eV is very close to this theoretical maximum, furthermore, silicon solar cells[1] with their record efficiencies of 25 % [8] are already close to the theoretical limit.

However, still 20% of the incident energy are lost due to the transmission of low-energy photons [9] for silicon solar cells (see Figure 1.1). Upconversion of these low-energy photons presents a possibility to overcome the Shockley-Queisser limit. In an upconversion process, two or more photons with energies too small to excite electron-hole-pairs, are converted

[1] In the following, the term silicon solar cell always refers to crystalline silicon.

into photons with energies above the band gap. The emitted photon can subsequently be utilitzed in the silicon solar cell. Theoretical calculations have shown that using upconversion the efficiency limit for a silicon solar cell can be pushed from 30 % [7] to 40.2 % [10].

Therefore, upconversion presents a mechanism to significantly reduce sub-band-gap losses without interfering with the electrical properties of the solar cell, hence, all upconverted photons reaching the solar cell can cause a true gain in current. The only requirements for the solar cell are a good transmission of sub-band-gap photons and the cell has to be bifacial, meaning that it can be illuminated as well from the rear side. Although a positive effect of upconversion in erbium-doped hexagonal sodium yttrium tetrafluoride (β-$NaYF_4$) for silicon-photovoltaics has already been shown [11–13], these effects are still relatively small with a maximum relative efficiency enhancement of 0.35% [13].

The main problem is the relatively low upconversion quantum yield. One approach to improve this quantity is to apply metallic nanoparticles close to the upconverter material and benefit from the plasmonic resonance within the nanoparticles [14–16]. The disadvantage of this procedure is that the application of a metal induces a non-radiative decay path due to the absorption within the metal. A second approach, which is followed in this work, is to embed the upconverter material into photonic structures. With this approach, two levers can be applied to increase upconversion quantum yields: first, the local irradiance can be enhanced within the structure in certain regions; second, the local density of states (LDOS) is altered [17]. When speaking of the density of states (DOS) or the LDOS, in this work, I refer to the photonic density of states. As upconversion is a non-linear process, an increase in the local irradiance also increases the upconversion quantum yield (UCQY). Furthermore, the LDOS-modification can have a beneficial effect if the probability for the upconversion emis-

sion can be enhanced or the direct re-emission from the first excited state can be suppressed. In this work, I present findings for the theoretical and experimental investigation of the influence of photonic structures on upconversion processes.

1.2 Objective of this work

The aim of this work was to beneficially influence upconverter material using photonic structures. Here, the most important parameter to be optimized is the UCQY. To be able to quantify the effects on upconversion, a simulation method was required. Using this method, the photonic structures could be optimized. These optimized structures should be fabricated and characterized to quantify the effects.

Within this work, photonic structures were produced for two main approaches to improve the effect of upconversion for silicon solar cells. The first approach is based on a macroscopic system, where the solar cell is combined with an upconverter material and additional Nanocrystalline Quantum Dots (NQDs) [18]. These NQDs absorb photons between the absorption edge of the solar cell and the absorption edge of the upconverter and re-emit photons that can be absorbed by the upconverter material. This concept is called spectral concentration [18, 19]. Additionally, geometric concentration is applied as the upconverter material does not cover the whole rear surfacebr of the solar cellbr. In order to realize this system, photonic structures are required as filters to efficiently guide photons according to their energy to the parts of the system, where they can be utilized most efficiently. The filter structures were produced from hydrogenated amorphous silicon carbide (a-Si_xC_{1-x}:H) in a plasma-enhanced chemical vapor deposition (PECVD)-process, where the refractive index

can be tuned with the silicon to carbon ratio. To achieve thin, homogeneous layers of variable refractive index, existing processes were adapted and new processes based on pulsed microwave sources were developed. Using the transfer matrix method (TMM), the filter structures were simulated and improved for the application using an evolutionary algorithm. Subsequently, the sensitivity of the structures against unavoidable process variations was tested in a Monte Carlo simulation and compared to simple Bragg structures.

The second approach investigated in this work was to directly embed upconverter material into photonic structures to benefit from a local irradiance enhancement and a varied local density of states. A simulation approach was developed to quantify both effects and account for these variations in a rate-equation model for the upconverter material. Using this model system, structures could be optimized for a maximum effect on the upconversion quantum yield. Different types of structures were investigated including a cavity structure, an interdigitated Bragg structure, a grating structure and a grating-waveguide structure.

An optimized cavity structure as well as optimized grating structures have subsequently been fabricated based on hexagonal sodium yttrium tetrafluoride doped with trivalent erbium (β-$NaYF_4$:Er^{3+})-nanoparticles embedded in polymethylmethacrylate (PMMA). The PMMA-layers were produced by spin-coating and combined with cavity filters fabricated by PECVD for the first structure. For the second structure, a grating was embossed into the spin-coated PMMA-layer using a stamp produced from a master structure fabricated by electron-beam lithography.

The simulation and experimental results were subsequently compared, which showed that the experimental results were very well predicted by the simulation approach.

1.3 Structure of this work

The introduction is followed by a description of the background of upconversion processes. Chapter 3 presents a survey of the theoretical background which describes the basics of photonic crystals and the different interaction mechanisms of electromagnetic fields and atoms.

In the forth chapter, the different simulation methods used in this work are described. Various different methods have been applied ranging from transfer matrix calculations via the scattering matrix method, band structure calculations and rigorous coupled wave analysis to finite-difference time-domain simulations. The latter corresponds to the most general method used in this work as it does not impose any limitations on the structure dimensionality or periodicity.

The fifth chapter gives an overview of the most important sample preparation methods, PECVD and spin-coating. Furthermore, the main characterization methods are described: the working principle of ellipsometry is explained and a brief description of the photoluminescence setup is given.

Chapter 6 describes the simulation results obtained first for the filter structures and in the following sections for the system in which upconverter material was embedded in photonic structures. Here, the results obtained for a cavity system, a Bragg structure, grating structures and grating waveguide structures are described.

In Chapter 7, the results obtained for the a-Si_xC_{1-x}:H-filter structures are described first, followed by the results obtained for the cavity structure and then those for the grating structure.

This chapter is followed by a conclusion and an outlook.

2 Background on Upconversion

The term upconversion describes anti-Stokes processes, thus, emission of photons with higher energies than the absorbed photons, where the energy difference exceeds $10\ k_BT - 100\ k_BT$. *This additional energy cannot be provided by phonons, thus, the processes rely on the conversion of two or more photons. The concept of such processes can be traced back to the* 1950*s, where Bloembergen had the idea of an infrared (IR) quantum counter based on subsequent absorption of IR-photons via excited state absorption (ESA) [20]. In* 2004*, Auzel gave a very detailed review about different upconversion processes [21]. To be useful for photovoltaic applications, upconversion has to be possible for incoherent radiation, thus for example processes based on second-harmonic generation cannot be applied. This chapter gives an overview over different upconversion mechanisms and materials showing upconversion properties. Furthermore, a definition of the upconversion quantum yield is given and the potential of upconversion for photovoltaics is described. The last section summarizes different approaches to improve the upconversion quantum yield.*

2.1 Upconversion Mechanisms

For incoherent radiation, there are two relatively efficient upconversion mechanisms [21]. The first and most simple one is ESA, where an electron in an excited state absorbs a second photon promoting the electron to an even higher state. The second process is energy transfer upconversion (ETU) where two ions[1] in their excited state interact and one relaxes back to the ground state transferring the energy to a second ion, which then is excited to a higher excited state [21]. This process is the most efficient upconversion mechanism for lanthanide-doped solids, whereas ESA is the second most probable mechanism. These two processes are sketched in Figure 2.1. Further upconversion mechanisms exist, which occur with a much lower probability for the upconverter system used here. These processes are cooperative sensitization, cooperative luminescence, second harmonic generation and 2-photon absorption excitation [21].

energy transfer (ET) requires resonant energy level distances, meaning that the energy differences between the first excited state and the ground state should differ by a maximum of a few k_BT from the energy difference between the higher excited state and the first one. ESA only requires this resonance if the excitation is monochromatic, for broad-band excitation, an excitation with two different photon energies is also possible.

As mentioned above, all upconversion processes are based on the absorption of two or more photons, hence, the upconversion luminescence shows a non-linear dependence on the irradiance that depends on the number of photons involved in the upconversion process for low excitation. For high excitations, this converges to a linear dependence as shown in [22–24]. In this work two-photon processes are most relevant where the upconversion

[1] In principle upconversion is also possible for molecules, but as this work concentrates on upconversion in Er^{3+}, here we talk about ions, only.

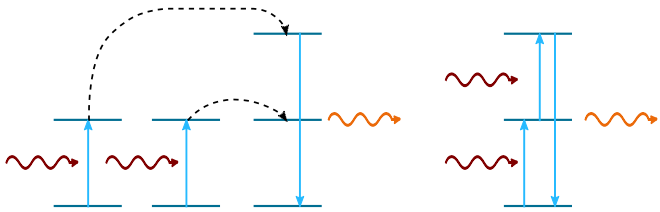

Figure 2.1: Most efficient upconversion mechanisms: energy transfer upconversion where two neighboring ions are excited to a first excited state by absorbing the incident photons (red curved arrows), this energy is transferred to a third ion (shown by the black dashed arrows), which leads to the population of a higher state. On the right, excited state absorption is shown, where a subsequent absorption of photons leads to the population of higher-energy states. These higher excited states can radiatively relax back to the ground state by emission of a higher-energy photon (orange curved arrows).

signal increases approximately with the second power of the irradiance for low excitation powers.

For β-$NaYF_4$:Er^{3+}, the material used here, the most efficient process is ETU, based on Förster energy transfer, which means that a virtual photon carries the energy from the donor to the acceptor ion and both ions can be treated as dipoles [25]. This type of interaction decreases with the sixth power of the distance between the ions. Thus, the host crystal and the doping concentration play a major role for the upconversion performance.

2.2 Upconverting Materials

There are different material classes that have been found to show upconversion, including lanthanide and uranide f-ions and transition metal d-ions embedded in solids [21].

Er^{3+} was the first ion to show upconversion properties [26] and is still one of the materials studied most [21]. This trivalent ion has a [Xe]$4f^{11}$ electron configuration, thus, an incomplete 4f-shell, that is shielded by filled 5s- and 5p-shells. This leads to rather sharp transitions of the 4f-electrons [27]. In a free ion, these transitions are forbidden for electric dipole transitions by the parity selection rule, thus, they are only allowed due to the interaction with the host crystal and the resulting crystal field [27].

One reason for the popularity of erbium-ions for upconversion is the fact that their energy-levels are conveniently spaced for the application in combination with silicon solar cells: photons in the near infrared (NIR) around a wavelength of 1523 nm can be absorbed and photons above the band gap of silicon at a wavelength of around 980 nm can be emitted. An electron can be lifted from the $^4I_{15/2}$ ground state to the $^4I_{13/2}$ first excited state by a first photon at a wavelength of 1523 nm. Subsequent absorption of a second photon or energy transfer can lift the electron to the $^4I_{9/2}$ state. From this state the electron can recombine radiatively back to the ground state, which leads to the emission of a photon at a wavelength of 800 nm. The more probable process, however, is multi-phonon relaxation (MPR) to the $^4I_{11/2}$ state and subsequent emission of a photon at 980 nm. Either way, the emitted photons can be utilized in a silicon solar cell. This is sketched in Figure 2.2.

One of the most promising host materials that has been investigated so far is β-$NaYF_4$ [21]. More details on this material system are given in

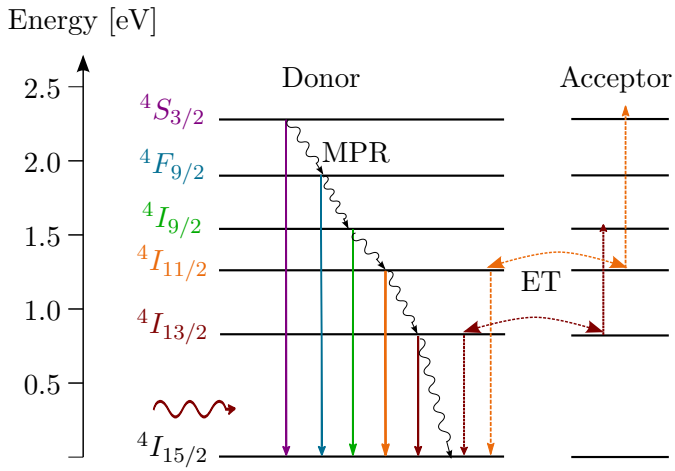

Figure 2.2: Energy levels of a trivalent erbium ion [28]. The absorption of a photon at 1523 nm as shown on the left promotes electrons to the $^4I_{13/2}$-state. Energy transfer processes denoted by the dark red and orange dotted arrows or excited state absorption lead to the population of even higher states. The colored arrows denote spontaneous emission processes from the respective energy levels to the ground state. The most important upconversion emission from the $^4I_{11/2}$-state is denoted by the bold orange arrow. The thin black curved arrows denote MPR-steps between neighboring energy levels.

[29] and the synthesis of the erbium-doped material for upconversion in a micro-crystalline form has been described by Krämer *et al.* [30]. Here the erbium-ion is embedded in the hexagonal host crystal, which shows very beneficial properties for upconversion. One of the most important properties of the host material is its phonon energy as the transitions are not perfectly in resonance and mediated by phonons. However, multi-phonon processes can also de-populate excited states, so too large phonon

energies are also detrimental to the process.

As the aim of this work is to embed upconverter material into photonic structures, the micro-crystalline β-$NaYF_4$:Er^{3+} is not really an option as the crystals are typically in the range of $1\mu m - 3\mu m$ and form even larger agglomerates [30] and are, therefore, too large to be embedded into a nano-scale photonic structure. Hence, for a photonic structure sizes below $1.5\mu m$ are required, which is smaller than the size of a single crystal. One approach that could be used for the combination with photonic structures is ion-implantation of erbium into already existing photonic structures as shown in [31–33]. However, the UCQY of the erbium ions in this configuration is expected to be rather low as the distance between the ions is not fixed as in a crystalline lattice, leading to non-optimized energy transfer processes. The second possibility is the use of upconverter nanoparticles, where a lot of progress has been made in recent years [34, 35]. Several groups showed upconversion signals from nano-crystalline β-$NaYF_4$ doped with different lanthanides [36–41]. Most synthesis routes rely on wet chemistry, but also different approaches like a mechano-chemical approach and combustion synthesis were investigated [42]. These nanoparticles can subsequently be embedded into a polymer like for example PMMA [43], the nanoparticles can be additionally stabilized with polyethylene glycol (PEG) [44].

To describe the upconversion characteristics of erbium-doped β-$NaYF_4$ under excitation at a wavelength of 1523 nm, a rate-equation model has been developed in our group [28, 45]. This model is based on experimentally determined Einstein coefficients and describes all relevant processes within the erbium ions taking into account the six lowest energy levels. The ground and excited state absorption of photons at a wavelength of 1523 nm and energy transfer processes lead to the population of higher levels. A de-excitation can occur by spontaneous or stimulated emission

or by multi-phonon relaxations. From the solution of the rate-equation model, the absorption as well as the luminescence and the UCQY from the various energy levels can be determined. This model is described in more detail in Section 4.6.

2.3 Definition of the Upconversion Quantum Yield

One of the most important properties of upconverter material is its upconversion quantum yield, which describes the efficiency of the upconversion processes. As this quantity is not always defined in the same way, here, we want to use the following definitions: we distinguish between the external upconversion quantum yield (eUCQY) and the internal upconversion quantum yield (iUCQY) according to:

$$eUCQY = \frac{\Phi_{UC}}{\Phi_{inc}}, \tag{2.1}$$

$$iUCQY = \frac{\Phi_{UC}}{\Phi_{Abs}}, \tag{2.2}$$

where Φ_{UC} corresponds to the flux of emitted photons with energies higher than those of the incident photons, Φ_{inc} describes the flux of incident photons and Φ_{Abs} the flux of absorbed photons. All fluxes are given in units of 1/s. With this definition of the UCQY, the maximum achievable internal quantum yield is 50 %, thus, using two incident photons to generate a single photon with higher energy.

Keeping the difference between these two quantities in mind becomes especially important when simulation and experimental results are compared, as the iUCQY is obtained from the simulations compared to the experimental results, where we are aiming for determining the eUCQY in

the context of this work. For the investigations shown here, we mainly restrict ourselves to the dominant emission in β-$NaYF_4$:Er^{3+} under an excitation at 1523 nm, which occurs at a wavelength of 980 nm.

2.4 Upconversion for Photovoltaics

As described above, upconversion offers the possibility to use photons with energies below the band gap of a semiconductor material for current generation in solar cells and can, therefore, be used to overcome the Shockley-Queisser efficiency limit for solar cells [7]. This becomes more and more interesting especially for mono-crystalline silicon solar cells, where record efficiencies of 25 % [8] have been reported, which are already very close to the theoretical limit of around 30 %. In order to increase the efficiency even further, new approaches like upconversion are required. Upconverter material can be applied to the rear side of a solar cell and absorbs the photons below the band gap that are transmitted through the bifacial cell. Thus, this material does not interfere neither with the optical nor the electrical properties of the solar cell and the only requirements to the cell are a high transmission in the infrared and that it has to be bifacial. If these requirements are met, all upconverted photons reaching the cell lead to a real gain in current.

The potential of upconversion for solar cells has been investigated by Trupke *et al.* first under black-body radiation and later under the AM1.5-spectrum [10, 46]. They found a maximum efficiency of 40.2 % for a solar-cell upconverter device. In 2012, this model was further extended to take the real absorption of silicon into account [47].

Experimentally, this concept has first been applied in 1996 to a gallium arsenide (GaAs)-solar cell [48] using a vitroceramic co-doped with ytterbium (Yb) and erbium (Er).

In 2007, Richards *et al.* applied the upconverter β-$NaYF_4$:Er^{3+} to a silicon solar cell and measured an external quantum efficiency (EQE) of 3.4 % under high laser excitation and in 2010 an EQE of 0.34 % was measured under a much lower excitation [12], both measured in the absorption range of the upconverter around 1523 nm. In 2013 an EQE of 1.79 % was measured for a system with an optimized bifacial solar cell and β-$NaYF_4$ doped with 25 % Er^{3+} under a monochromatic irradiance of $1000 W/m^2$ at a wavelength of 1508 nm [13]. Additionally, this system was investigated under broad-band excitation and an increase in short circuit density of $13.3\ mA/cm^2 \pm 3\ mA/cm^2$ was measured [13] under concentration. The upconverter absorbs two photons in the infrared, at a wavelength of around 1523 nm and a higher-energy photon at a wavelength of 980 nm or 800 nm is emitted. Both of these emitted photons can be absorbed in a silicon solar cell whereas silicon is transparent for the 1523 nm photons, apart from free-carrier absorption. The maximum relative increase in solar cell efficiency was reported to be 0.19% under 210 suns [13]. This effect is still very small. Thus, new approaches are required to increase the UCQY.

2.5 Approaches to Increase Upconversion Quantum Yields

Upconversion is a non-linear process, and consequently, the UCQY of the process increases with the irradiance [22, 24]. Therefore, it is beneficial to the upconversion process to concentrate those photons lying within the absorption range of the material onto rather small spots. This can be achieved either in a macroscopic setup using geometric concentration or in a microscopic way exploiting plasmonic or photonic structures. A second issue is that the absorption range of the upconverter used in this work only covers a wavelength range from about 1480 nm to around 1580 nm.

2.5.1 Geometric and Spectral Concentration

As there is a limited amount of photons within the absorption range of the upconverter in the solar spectrum and there is a rather broad range between the absorption edge of silicon and the absorption range of the upconverter, these intermediate photons can be utilized in the upconversion process if they are shifted to the absorption range of the upconverter by a luminescent material. This concept is called spectral concentration [49, 50]. A second approach to increase the photon flux on the upconverter material is geometric concentration, here, the upconverter only covers a part of the solar cell. A system design that uses these two approaches in a macroscopic way is shown in Figure 2.3.

The system consists of a bifacial silicon solar cell, upconverter material, NQDs, which are responsible for the spectral concentration and adapted filter structures. The incident photons can be divided into three categories according to their wavelength. The first part, which is marked by the blue arrows describes photons that are within the absorption range of the silicon solar cell, so the main part of the incident blue photons are absorbed within the cell. Those photons reaching the rear-side of the cell are reflected back into the cell by both filter structures. The upconverted photons (small blue arrows) which are also in this spectral range are guided into the solar cell, as well. The green arrows in Figure 2.3 correspond to photons with energies below the band gap of silicon but energetically above the absorption range of the upconverter. These photons have to reach the fluorescent concentrator consisting of NQDs where they are absorbed and re-emitted in the absorption range of the upconverter (red arrows). These photons have to be guided to the upconverter pads in order to be transformed into higher-energy photons (blue arrows) which then can be utilized again in the silicon solar cell.

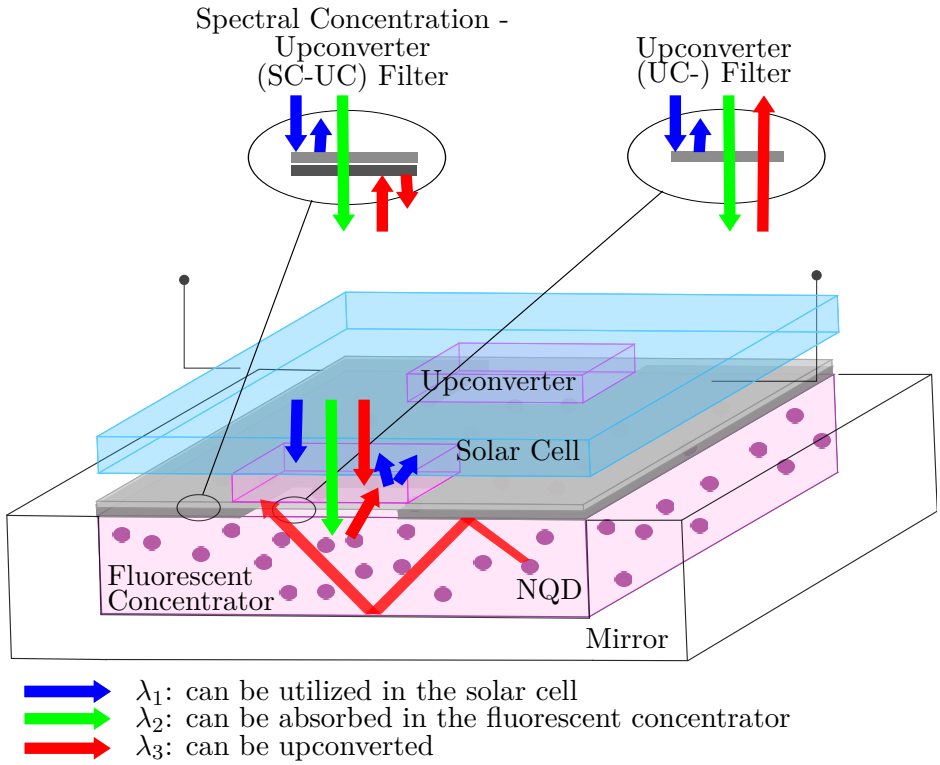

Figure 2.3: Concept for a system using a silicon solar cell and upconverter material. Furthermore, the intermediate photons (green arrows) are spectrally concentrated onto the upconverter using spectral concentration with a fluorescent concentrator based on NQDs. Two different filter types are required to distribute photons according to their wavelength [18, 45].

This system can only work effectively, if the photons are distributed according to their wavelength and each photon reaches the part of the system where it can be utilized most efficiently. To ensure this distribution, two different filter structures are required. The first filter reflects photons with energies above the band gap of silicon back into the solar cell.

As this filter is applied directly below the upconverter and as it ensures that upconverted photons are guided towards the solar cell, it is called upconversion (UC)-filter in the following. The second filter is responsible for guiding the low-energy photons (red arrow) to the upconverter pads. Thus, it has to reflect photons at a wavelength of around 1523 nm. Additionally, it also has to reflect photons in the absorption range of silicon (blue arrows) back into the cell. As this filter is a combination between a filter responsible for spectral concentration (spectral concentration (SC)-filter) and the UC-filter, it is called SC-UC-filter.

Below the upconverter pads, only the UC-filter is applied whereas the rest of the surface of the embedded NQDs is covered by the SC-UC-filter. These two filter structures have been developed within the scope of this work and the results are shown in Section 6.3 and Section 7.1. This system uses spectral and geometric concentration on a macroscopic scale.

2.5.2 Exploiting Plasmonic Effects

One possibility to obtain a local irradiance enhancement on a microscopic scale is to exploit plasmon resonances around metallic nanoparticles. These plasmon resonances can lead to quite considerable local irradiance enhancements which could drastically improve the upconversion processes. However, this is not the only effect, as the transition rates within the erbium ion are varied due to alterations in the LDOS. This can either be a beneficial or a detrimental effect. Furthermore the presence of the absorbing metal provides an additional non-radiative decay path [51].

Simulations have been carried out using the same rate-equation model for the upconverter material as used in this work showing that the luminescence could be increased by a maximum factor of 4.3 [14, 16, 28, 52] due to the presence of a gold nanoparticle with optimized size.

This process has also been investigated experimentally, Schietinger *et al.* placed an upconverting nanoparticle into close proximity to a gold nanoparticle and measured a 3.8-fold increase in the luminescence if the upconverter is placed at an optimized position [53]. A similar enhancement factor of 3.4 could be obtained for upconverter nanoparticles embedded in PMMA on a structured gold surface [54]. Similar effects on upconversion processes could be determined by various other groups [55–58]. Furthermore, the effect on the photoluminescence of erbium has been investigated [32, 59].

2.5.3 Exploiting Photonic Effects

A second microscopic approach, which is investigated in more detail in this work, is to increase the local irradiance using photonic structures. Compared to the plasmonic effects, this approach has the advantage that no additional decay path is introduced as the structure consists of dielectrics, which show basically no absorption in the IR.

Embedding of upconverter material into a photonic structure environment has two effects:

1. The local irradiance within the structure is varied due to the photonic structure environment [60, 61].

2. The photonic LDOS is varied within the structure: this influences the spontaneous emission probabilities for all transitions that are possible within the upconverter material according to Fermi's golden rule as described in Subsection 3.3.3. In principle, the variations of the LDOS can be measured using scanning near field optical microscopy (SNOM) [62, 63] or by electron energy loss spectroscopy (EELS) [64].

The desired effect on the local irradiance is clear, the aim here is to increase the irradiance at the upconverter positions as much as possible, as this also increases the UCQY as described above. The influence of the LDOS is slightly more complex. In principle, it is beneficial to increase the density of states at the emission wavelength of 980 nm, however, this effect is shown to be rather small in the following. A much larger effect could be found if the LDOS is decreased at the absorption wavelength of 1523 nm. The reason for this behavior is that the first excited state is depopulated by radiative emission of such photons. Thus, decreasing this emission probability has the highest potential to increase the upconversion quantum yield. Typically, over 90 % of the absorbed photons are directly re-emitted via this path. Thus, even a slight reduction of the emission probability increases the iUCQY drastically.

Theoretical work on this process includes work on grating structures and on a cavity system [17, 65–68]. Furthermore, a lot of theoretical work has been carried out on upconversion based on second harmonic generation in cavity structures [69–71]. These systems were also investigated experimentally [72, 73]. The experimental work for upconversion using erbium ions includes the work of Johnson *et al.* and Yang *et al.* who investigated the upconversion of erbium ions embedded in a porous silicon Bragg structure [74, 75] and in an inverted opal system [76]. In the first system, the erbium is directly electroplated onto the silicon, which is subsequently oxidized, thus, the erbium ions are basically embedded in SiO_2 whereas in the second system they are embedded in an $YbPO_4$ host crystal and the inverse opal is built by a sol-gel approach. Additionally, Niu *et al.* investigated the influence of an opal-rear side on erbium-ytterbium co-doped nanoparticles [77].

In this work, the effect of photonic structures on upconversion processes is investigated theoretically and experimentally. For the theoretical inves-

tigation, simulations of the optical properties of the different photonic structures, the irradiance distribution and the LDOS, were coupled to a rate-equation model. This rate-equation model does not only consider the absorption and emission processes, but also energy transfer between neighboring ions, as this presents the main upconversion mechanism within erbium ions in a β-$NaYF_4$-lattice, and multi-phonon relaxation. Therefore, it would be very important to know if and how energy transfer processes are influenced by the variations of the LDOS. This, however, is still heavily discussed in literature:

De Dood *et al.* proposed that a variation of the LDOS in the optical range will not influence the energy transfer rates significantly. The reason for this being that the virtual photon, which is responsible for the energy exchange between the ions has a very short lifetime, thus, covers a very broad energy range, due to the uncertainty principle [78]. The base for this theory is an experiment where erbium ions are ion-implanted into soda lime glass. The LDOS is changed by immersing the samples in different liquids with different refractive indices. As the refractive index of the liquid is either larger or smaller than the refractive index of the glass an enhancement or a reduction of the LDOS is expected when approaching the surface. As the erbium ions are embedded at a certain depth within the material, the expected changes in the LDOS are in the range of 20 % but, no effect on the energy transfer rate could be found.

Blum *et al.* also found no influence of the LDOS on energy transfer [79]. In this case, they had Förster resonant energy transfer (FRET)-pairs of two fluorescent dyes separated by a strain of deoxyribonucleic acid (DNA) to ensure a constant separation. These pairs are separated by polymer layers from a metallic mirror having different thicknesses. The LDOS varies in an oscillating manner when approaching the mirror. The excitation lifetime of the donors is measured in a system without acceptors

and in pairs. It was found that for both cases, the lifetime, and thus, also the transfer rate shows the same oscillating behavior. This is due to the spontaneous emission which is modified according to Fermi's golden rule. A relation of both transition rates showed no influence of the LDOS on the energy transfer.

On the other hand there are also publications promoting an influence of the LDOS on energy transfer. The most prominent example is probably the paper from Andrew and Barnes. They investigated the influence of a metallic mirror on energy transfer pairs that have been separated by 0 nm to 25 nm. The acceptor distance to the mirror is varied whereas the donor distance stays constant. This is carried out for a metallic mirror on one side of the sample, a metallic cavity with metal layers on both sides and a reference sample without the mirrors. They found a linear dependence of the energy transfer rate on the donor emission rate indicating the influence of the LDOS [80].

In this work, I follow the argument of de Dood *et al.* and assume that energy transfer processes are not influenced by the LDOS. However, the potential impact of LDOS-modified ET is also investigated in simulations and the results are compared to the experiments.

3 Theoretical Background

In this chapter, the theoretical background is described for the following investigations. Starting with Maxwell's equations, the concept of photonic crystals is explained, from which the photonic band structure and the photonic density of states are derived. Furthermore, the meaning of the Einstein coefficients is explained and Fermi's golden rule is described, which states the influence of the photonic density of states on spontaneous emission. The descriptions in this chapter mainly follow [81–86].

3.1 Electromagnetic Fields and Waves

The Maxwell equations (see Equations 3.1 to 3.4) present the base for all following considerations about photonic crystals.

$$\nabla \times \vec{H} = \vec{j} + \frac{\partial \vec{D}}{\partial t} \tag{3.1}$$

$$\nabla \times \vec{E} = -\frac{\partial \vec{B}}{\partial t} \tag{3.2}$$

$$\nabla \cdot \vec{D} = \rho_Q \tag{3.3}$$

$$\nabla \cdot \vec{B} = 0 \tag{3.4}$$

$\vec{H}$, $\vec{E}$, $\vec{B}$ and $\vec{D}$ describe the magnetic and electric fields, the magnetic induction and the electric displacement field, respectively, $\vec{j}$ describes the free current density and ρ_Q accounts for free charges. All simulation methods described in Chapter 4 describe solutions to these equations for certain boundary conditions.

If we assume to work in the linear regime, thus with low field strength and a macroscopic and isotropic material, we can relate $\vec{E}$ and $\vec{D}$ by:

$$\vec{E} = \epsilon_0 \cdot \epsilon_r(\vec{r}, \omega) \cdot \vec{D}, \tag{3.5}$$

$$\vec{B} = \mu_0 \cdot \mu_r(\vec{r}, \omega) \cdot \vec{H}, \tag{3.6}$$

where ω is the angular frequency, ϵ_0 and μ_0 describe the vacuum permittivity and permeability and ϵ_r and μ_r correspond to the relative values within a material, which are scalar in this simplification. Furthermore, for the materials investigated here, the relative permeability is close to unity.

If one additionally assumes dispersion-less material where the relative permeability does not depend on the frequency ω, the differential equation for the electric field can be expressed as

$$\nabla^2 \vec{E} - \mu_0 \epsilon_0 \epsilon_r(\vec{r}) \frac{\partial^2 \vec{E}}{\partial t^2} = 0, \tag{3.7}$$

where t denotes the time. Typically, there are two different approaches to solve this equation, either in the time domain or in the frequency domain. The simulation methods used in the following can be divided according to this criterion. The time-domain approach is followed for example by finite-difference time-domain (FDTD), whereas for the rigorous coupled wave analysis (RCWA) or MIT photonic bands (MPB) are frequency-domain methods. One solution for this condition is a plane-polarized harmonic wave, which is expressed in a complex exponential form to simplify calculations

$$\vec{E} = E_0 \cdot exp\left[i\omega\left(t - \frac{x}{v}\right)\right], \tag{3.8}$$

where x describes the space coordinate, v the group velocity, t the time, ω the angular frequency and E_0 the amplitude of the field.

According to Fourier analysis, any solution can be expressed as a combination of these harmonic waves.

By solving the wave equation (see Equation 3.7) for harmonic waves, the dispersion relation:

$$\left|\vec{k}\right| = \frac{c}{n} \cdot \omega, \tag{3.9}$$

is obtained. Here $|\vec{k}|$ presents the magnitude of the wave vector, c corresponds to the speed of light in vacuum, ω to the angular frequency and n to the refractive index. This dispersion relation holds for homogeneous media, however, if we go to periodically varying structures, so-called photonic crystals, this dispersion relation is altered.

3.2 Photonic Crystals

In principle, the concept of photonic crystals goes back to 1888, where Lord Rayleigh [87] described the properties of a multilayer dielectric mirror, which consists of a periodic arrangement of thin films with different refractive indices. If these layers have adapted thicknesses, a high reflectance can be achieved within a certain wavelength range. In 1946, Purcell investigated a variation of the spontaneous emission rate for an atom within a cavity [88]. From 1972 on, Bykov theoretically investigated the effect of a photonic structure on spontaneous emission processes [89, 90], more precisely, the suppression of emission in a one-dimensional

cavity. Already in 1979 Ohtaka investigated the photonic band structure of a three-dimensional arrangement of spheres [91]. However, the topic really started drawing attention with the publication of two papers from Yablonovitch and John in 1987 [92, 93], where Yablonovitch investigated the influence of a photonic band gap on spontaneous emission processes and John described that a strong localization of photons is possible for certain disordered microstructures.

Around this time, the term photonic crystal [94, 95] has been defined in analogy to a crystal lattice. In the latter case, semiconductor materials exist, where electrons are subject to band gaps [96], thus, energy ranges in which electrons cannot propagate. Likewise, photonic band gaps can exist within a photonic crystal which, in this case, translates into a periodically varying refractive index [81]. As for a crystal lattice, the term "crystal" implies an infinite periodicity, for photonic crystals a distinction between one-, two- and three dimensional photonic crystals is made according to the number of dimensions with infinite periodicity. Thus, it is possible to build a material in which certain photons are not allowed to propagate either in specific directions or not at all for an omnidirectional band gap. Photons within a certain wavelength regime incident on such a material are, therefore, reflected. This offers the opportunity to realize filter structures using photonic crystals or more complex structures, where light propagation is only possible in a certain direction within the material. Detailed reviews about the properties of photonic crystals are given in [97, 98].

3.2.1 Photonic Band Structure

The analogy to crystal lattices and their influence on electrons leads to the concept of a photonic band structure that describes the relationship

between the frequency ω and the wave vector $\vec{k}$. To reach this, the eigenvalue problem represented by the so-called Master equation (see Equation 3.10) can be deduced from Maxwell's equations without free charges or currents:

$$\nabla \times \left(\frac{1}{\epsilon(\vec{r})} \nabla \times \vec{H}(\vec{r}) \right) = \left(\frac{\omega}{c} \right)^2 \vec{H}(\vec{r}), \tag{3.10}$$

with the position vector $\vec{r}$ and c being the velocity of light. Typically, this equation is expressed in terms of the magnetic field $\vec{H}$ for mathematical convenience. It is subsequently solved for the different values of the wave vector $\vec{k}$ [81] using a Bloch approach. As there is no fundamental length scale in this equation, it is scale-invariant. This implies that the properties of the photonic crystal are scalable with the structure sizes the refractive index of the medium, hence, if a resonance occurs within a structure with refractive index n at a frequency ω, the resonance shifts to a frequency of $\omega \cdot s$ if the refractive index is divided by the same factor s. Thus, beneficial properties of a structure like the resonance frequency can be shifted to another frequency by simply scaling the structure dimensions or the refractive indices of the structure.

Using this concept of photonic bands, materials with a stop band for a certain wavelength range can be built. This implies that photons in this wavelength range cannot propagate within the material. This behavior offers very interesting applications for photonic crystals ranging from reflectors to waveguides and to influencing the spontaneous emission rate of atoms within the material.

To show this influence on the band structure, the structure sizes have to be on a length scale in the order of the wavelength of the light, for larger structure sizes, the behavior can be determined by geometric optics and if the refractive index changes on a length scale much smaller than

the wavelength of light, effective medium approximation (EMA) can be applied, as the changes in refractive index are not "felt" anymore by the electromagnetic wave, thus the material can be treated as if it had a homogeneous refractive index [99, 100].

3.2.2 Photonic Density of States

From the photonic band structure, with potential photonic band gaps, the photonic density of states $\rho(\omega)$ can be derived. This density of states (DOS) is proportional to the inverse of the slope of the band structure and can, therefore, be calculated numerically and directly from the band structure for a photonic crystal [101]:

$$\rho(\omega) = \sum_{m} \int_{1.BZ} d^3\vec{k}\delta(\omega - \omega_m(\vec{k})), \tag{3.11}$$

with the DOS $\rho(\omega)$, the band index m, ω_m describing the angular frequency of band m, which depends on the wave vector $\vec{k}$ and δ representing the Dirac delta function. The integral is carried out over the first Brioullin zone 1.BZ.

The photonic DOS in vacuum can be obtained by using a particle in a box approach and basically counting the equidistant states within this resonator [102]. Using the linear dispersion relation, the density of states per frequency ω and per volume can be obtained:

$$\rho(\omega) = \frac{\omega^2}{\pi^2 c^3} \tag{3.12}$$

In a homogeneous medium, the speed of light c scales with $1/n$ with the refractive index in Equation 3.12. Thus, the slope of the dispersion relation is reduced with the refractive index n. This leads to a larger DOS for a material with a higher refractive index.

The most simple and well-known example for a 1D-photonic crystal is a Bragg stack consisting of infinitely extended layers with two different refractive indices n_1 and n_2, where the layer thicknesses $d_{1,2}$ of the respective layers is given by a quarter of the design wavelength λ_{des} in the respective medium

$$d_{1,2} = \frac{\lambda_{des}}{4 \cdot n_{1,2}}. \tag{3.13}$$

This leads to a high reflection at this design wavelength λ_{des}. If we look at the band structure of such a photonic crystal, we see a band splitting close to the edge of the first Brillouin-zone. This can be understood if we look at the field distribution of the waves at the edge of the Brioullin-zone. Both waves have the same wave vector $\vec{k}$. However, the field distributions are different, they can have their maxima either in the high-index material or in the low-index material. This leads to different energies and subsequently different frequencies ω for the two waves and, hence, band splitting [81].

As the total number of states only depends on the effective refractive index, not on the band structure, a band gap in a certain frequency range leads to an increased number of states close to the band edge [103, 104].

This effect of an increased DOS in a certain wavelength range can be exploited to enhance spontaneous emission rates according to Fermi's Golden Rule [84, 85, 105, 106] described in Subsection 3.3.3. For this interaction between an emitter and the photonic structure environment, the DOS at the emitter position, the local density of states (LDOS), has to be considered. This local information can be obtained from the band structure if additionally to the overall DOS the field distribution for the different modes are taken into account [101]:

$$\rho(\omega, \vec{r}) = \sum_m \int_{1.BZ} d^3\vec{k} \left| E_{m,\vec{k}}(\vec{r}) \right|^2 \delta(\omega - \omega_m(\vec{k})), \tag{3.14}$$

where $\rho(\omega, \vec{r})$ describes the LDOS and $E_{m,\vec{k}}(\vec{r})$ describes the field distribution of the Bloch modes with band index m and wave vector $\vec{k}$.

3.2.3 Examples for Realized Photonic Crystals

We are looking again at the Bragg stack as the most simple example, which shows a very high reflectance an the design wavelength λ_{des} for normal incidence. For larger angles, the reflectance peak shifts to smaller wavelengths. The origin of the band gap is described above. The contrast between the refractive indices determines the size of the gap [81]. This one-dimensional band gap not only occurs for Bragg structures, but for all one-dimensional photonic crystals [81] independent of the contrast between the two refractive indices. Representing the most simple system with photonic band gaps multilayer structures have been investigated since 1888 [87]. Apart from multilayer structured consisting of alternating layers of different refractive indices [107], so-called Rugate-filters with a gradually varying index [108, 109] were thoroughly investigated.

The first photonic crystal with higher dimensionality was produced by Yablonovitch *et al.* in 1991 for microwave frequencies and basically consisted of air holes drilled into a high-refractive index material forming a diamond lattice. This structure was later called "Yablonovite" [110]. However, as the production process for this structure was based on mechanical drilling it was very difficult to scale this structure down to work at optical wavelengths.

As an example for a two-dimensional photonic crystal, one could imagine a system of holes drilled into a substrate forming a square or hexagonal lattice with a defined period resulting in a change in refractive index in two dimensions while in the third dimension, the refractive index stays constant. A band gap for both polarizations was found theoretically and

also shown experimentally in a triangular lattice of air holes in gallium arsenide (GaAs) [111]. Furthermore, it has been shown that the band gap can be increased if holes with two different diameters are used [112].

The production of three-dimensional photonic crystals for optical frequencies was achieved first in the infrared (IR) [113] and then in the visible range [114] in 1998 and 1999 based on a so-called "woodpile"-structure. This structure consists of layers of regularly arranged rectangular "logs" of high-index material in air, where the consecutive layers are turned by 90 degrees. Later, the investigation focused on so-called opal structures, consisting of a regular arrangement of spheres, typically in a face centered cubic (fcc)-lattice. The advantage of these structures is that they typically self-assemble [115]. These structures cannot obtain a complete band gap due to their cubic symmetry, however, the inverted structure does have a complete band gap for the higher bands [101].

As the definition of a crystal implies an infinite extension, all realized materials are called photonic structures in this work whereas the simulations typically consider photonic crystals in the sense described above. It is assumed that the effect of boundaries and surfaces can be neglected for material in macroscopic dimensions.

3.3 Interactions between Electromagnetic Fields and Atoms

A radiative transfer of energy between electromagnetic waves and atoms is possible if the energy difference between an initial electronic state i and a final state f within the atom corresponds to the energy of a photon [83]:

$$E_i - E_f = \hbar\omega. \tag{3.15}$$

Here, $\mathcal{E}_i$ and $\mathcal{E}_f$ describe the energies of the initial and final states, respectively, ω is the angular frequency and $\hbar$ describes the reduced Planck constant.

3.3.1 Einstein Coefficients

If the condition given in Equation 3.15 is met, three different kinds of interactions are possible [82, 83]:

- absorption of photons from the field by the atom,
- stimulated emission of photons and
- spontaneous emission of photons.

The following description mainly follows [83]. To investigate these interactions, the so-called Einstein coefficients B_{if} (B_{fi}, A_{fi}) were defined for the absorption (stimulated and spontaneous emission) as proportionality constants between the transition probabilities W and the spectral energy density u:

$$W_{i\to f} = B_{if} u(\omega_{fi}), \tag{3.16}$$

$$W_{stim,f\to i} = B_{fi} u(\omega_{fi}), \tag{3.17}$$

$$W_{spont,f\to i} = A_{fi}, \tag{3.18}$$

where i denotes the lower energy level and f the higher one, and ω_{fi} describes the angular frequency corresponding to the energy difference between state f and state i according to Equation 3.15. $W_{i\to f}$ describes the absorption probability, $W_{stim,f\to i}$ describes the stimulated emission probablity and $W_{spont,f\to i}$ the spontaneous emission probability. These coefficients are subsequently used to describe the interactions between an electromagnetic wave and an atom.

3.3.2 Planck's Law

As described above, a DOS can be defined for photons. Additionally, the occupation probability for the different states is important. For photons as bosons, this occupation is given by the Bose-Einstein distribution f_{BE}:

$$f_{BE} = \frac{1}{exp\left(\frac{\hbar\omega}{k_B T}\right) - 1}, \tag{3.19}$$

with the Boltzmann constant k_B and the absolute temperature T.

The spectral energy density u of the emitted radiation, which is described by Planck's law can be determined by multiplying the DOS in vacuum given by Equation 3.12 and the Bose-Einstein distribution f_{BE} with the energy of a single photon $\hbar\omega$:

$$u(\omega) = \hbar\omega\rho(\omega)f_{BE}(\omega, T) = \frac{\hbar\omega^3}{\pi^2 c^3} \cdot \frac{1}{\exp\left(\frac{\hbar\omega}{k_B T}\right) - 1}. \tag{3.20}$$

At thermal equilibrium, the probability for emission and absorption are equal so the occupation N_i and N_f of the initial and the final state is constant. Furthermore, the occupation of the levels is given by Boltzmann statistics taking the degeneracy g_i and g_f of the levels into account leads to the following expression for the spectral energy density u:

$$u(\omega) = \frac{A_{fi}}{B_{if}\frac{N_i}{N_f} - B_{fi}} = \frac{A_{fi}/B_{fi}}{\frac{g_i \cdot B_{if}}{g_f \cdot B_{fi}} \cdot \exp\left(\frac{\hbar\omega}{k_B T}\right) - 1}. \tag{3.21}$$

A comparison to Planck's law shown in Equation 3.20 leads to the following relations for the Einstein coefficients:

$$\frac{A_{fi}}{B_{fi}} = \frac{\hbar\omega^3}{\pi^2 c^3}, \tag{3.22}$$

$$g_f \cdot B_{fi} = g_i \cdot B_{if}. \tag{3.23}$$

Thus, if the levels i and f have equal degeneracies, the Einstein coefficients for absorption and stimulated emission are equal. Whereas the Einstein B-coefficients are material properties, the A-coefficient is influenced by the number of states, where the density of states comes into play. Therefore, if we increase the density of states, we increase the spontaneous emission while this does not directly influence the stimulated emission and absorption processes.

3.3.3 Fermi's Golden Rule

Fermi's golden rule states that the transition probability for an electronic transition scales with the local density of final states. Thus, a photon can only be emitted from an excited atom if the photonic local density of states is finite and the probability for the emission process increases with increasing LDOS.

The derivation of Fermi's golden rule is explained in [84–86]. It is based on a solution of the Schrödinger equation for a perturbed system. Under the assumption that the final state is a photonic one, hence, a photon is emitted from the excited atom, the dependence of the transition rate on the photonic density of states $\rho(\mathcal{E})$ at the photon energy $\mathcal{E}$ can be derived.

$$W_{fi} = \frac{2\pi}{\hbar}\rho(\mathcal{E})\left|H_{fi}^{S}(0)\right|^{2}. \tag{3.24}$$

This effect of an influence of the photonic band structure on the spontaneous emission rate has been theoretically investigated for an atom in a cavity [88, 116] and within photonic crystal environments close to a photonic band gap [106, 117–119] where the emission was found to be enhanced. The suppression of the emission within a photonic band gap of different photonic crystals has also been investigated by several groups

[92, 118, 120, 121]. A more detailed review on the influence of photonic structures on spontaneous emission is given in [122].

Experimentally, the emission enhancement near a photonic band gap has been shown for InAs quantum dots in a resonant cavity, while the emission from off-resonance quantum dots was suppressed [123]. This has also been investigated using silicon-based cavity structures doped with erbium [124, 125]. For the emission within an opal matrix also an enhancement of the spontaneous emission close to the band gap and a suppression within the band gap was found for the emission from different materials [126–129].

4 Simulation Methods

For this work, several different optical simulation methods were used to determine the irradiance distribution and the local density of photonic states within photonic structures. Using different approaches was necessary as each of the methods has different advantages and limitations. The transfer matrix method and the scattering matrix method were employed for the description of one-dimensional problems. Photonic band structure calculations were used to improve the understanding of the other simulation results. The rigorous coupled wave analysis was utilized for the simulation of periodic structures and the finite-difference time-domain method presents the most general method used here that can in principle be applied to all simulations. The results were validated by a comparison of different methods wherever possible. The findings for the local density of states and the irradiance distribution were subsequently used in a rate-equation model to describe the influence of a photonic structure environment on an upconverting material. Most of the methods used here were also applied and are therefore described in the diploma thesis of Sebastian Wolf [130].

4.1 Transfer Matrix Method

The transfer matrix method (TMM), as an analytical approach, presents one of the most simple and intuitive possibilities to solve Maxwell's equations for a structure where the refractive index n only varies along one spatial direction. This one-dimensional system, which only varies along the z-axis and is homogeneous and infinitely extended in all other directions is illuminated by a plane wave with a wavelength λ under an angle θ_0 in this approach. The following derivation follows [131].

Looking at a thin film on a substrate, the electric field at boundary b between the substrate and the film can be separated into wave components traveling into the positive or negative direction. Thus, the electric field at this boundary can be expressed as the sum over these two components. The corresponding magnetic field at the same boundary can be related to the electric field by the optical admittance $\eta_{i,(s,p)}$ in layer i for s- and p-polarization, respectively

$$E_b = E_{ib}^{+} + E_{ib}^{-}, \tag{4.1}$$

$$H_b = \eta_{i,(s,p)} E_{ib}^{+} - \eta_{i,(s,p)} E_{ib}^{-}, \tag{4.2}$$

where E_{ib}^{+} (E_{ib}^{-}) corresponds to the electric field component of the wave traveling in positive (negative) direction in the medium with index i at position b.

To obtain the film characteristics we start at the rear surface b. From the fields at this boundary, the fields at boundary a, the film surface, can be determined by taking into account only the phase shift δ, which results from the wave traveling through the film. This phase shift is determined by

$$\delta = \frac{2\pi N_i \cos(\theta_i)}{\lambda}, \tag{4.3}$$

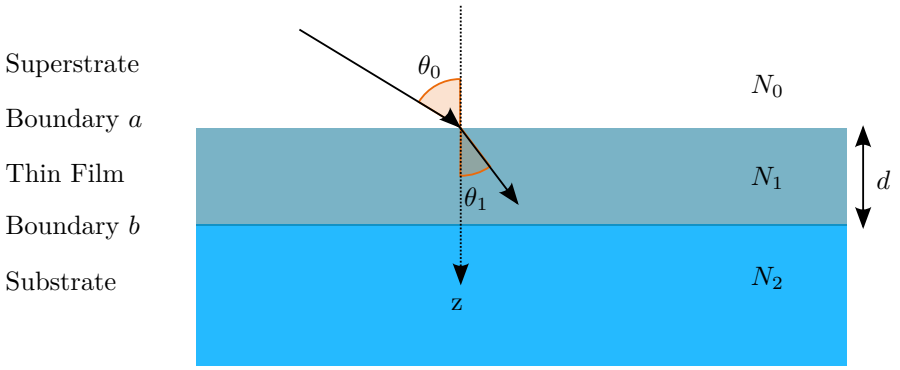

Figure 4.1: Sketch of the simulation setup for the transfer matrix method (adapted from [131]). The arrows denote the propagation vector of a plane wave. This wave with wavelength λ is incident under an angle θ_0 through a superstrate onto a thin film on a substrate. The wave is diffracted and propagates in medium 1 under an angle θ_1.

with the wavelength λ, the complex refractive index N_i of the film and the angle between the propagation direction of the plane waves within the medium and the surface normal θ_i.

The respective components of the fields at the boundary a can then be obtained by multiplying the wave traveling in positive direction by $exp(i\delta)$ and the one traveling in negative direction by $exp(-i\delta)$. Hence, the electric and magnetic fields at the boundary a can be found by

$$E_a = E_{ia}^{+} + E_{ia}^{-} = E_b \cos(\delta) + H_b \frac{1}{\eta_{i,(s,p)}} \sin(\delta) \tag{4.4}$$

$$H_a = H_{ia}^{+} + E_{ia}^{-} = E_b i \eta_{i,(s,p)} \sin(i\delta) + H_b \cos(\delta). \tag{4.5}$$

These expressions can subsequently be converted into a matrix representation

$$\begin{pmatrix} E_a \\ H_a \end{pmatrix} = \begin{pmatrix} \cos(\delta) & i\sin(\delta)/\eta_{s,p} \\ i\eta_{s,p}\sin(\delta) & \cos(\delta) \end{pmatrix} \begin{pmatrix} E_b \\ H_b \end{pmatrix} := \hat{M}_1 \cdot \begin{pmatrix} E_b \\ H_b \end{pmatrix}, \tag{4.6}$$

where $\hat{M}_1$ describes the transfer matrix for the film and with the tilted optical admittances η_s and η_p for s- and p-polarization, respectively

$$\eta_s = \sqrt{\frac{\epsilon_0}{\mu_0}} \cdot n \cdot \cos(\theta) \tag{4.7}$$

$$\eta_p = \sqrt{\frac{\epsilon_0}{\mu_0}} \cdot \frac{n}{\cos(\theta)}. \tag{4.8}$$

This relationship connects the tangential components at the interface between a film and a superstrate (denoted as boundary a in Figure 4.1) with the tangential components of $\vec{E}$ and $\vec{H}$ which are transmitted through the interface to the substrate (denoted as boundary b in Figure 4.1) for a thin film on a substrate. Furthermore, if the parameters B and C are defined as

$$\begin{pmatrix} B \\ C \end{pmatrix} := \begin{pmatrix} \frac{E_a}{E_b} \\ \frac{H_a}{E_b} \end{pmatrix} = \hat{M}_i \cdot \begin{pmatrix} 1 \\ \eta_{sub,(s,p)} \end{pmatrix}, \tag{4.9}$$

using the optical admittance $\eta_{sub,(s,p)}$, and the transfer matrix $\hat{M}_i$. The characteristic matrix of a thin film arrangement consisting of m layers can be obtained by a matrix product of the matrices of the single layers

$$\begin{pmatrix} B \\ C \end{pmatrix} = \left[\prod_{i=1}^{m} \begin{pmatrix} \cos(\delta_i) & \frac{1}{\eta_{i,(s,p)}}\sin(\delta_i) \\ i\eta_{i,(s,p)}\sin(\delta_i) & \cos(\delta_i) \end{pmatrix} \right] \begin{pmatrix} 1 \\ \eta_{sub} \end{pmatrix} \tag{4.10}$$

with the phase thickness $\delta = \frac{2\pi \cdot N_i \cdot \cos(\theta_i)}{\lambda}$ where the angles θ_i in medium i can be obtained by Snell's law and $\eta_{i,s}$ and $\eta_{i,p}$ correspond to the tilted

optical admittances for s- and p-polarization, respectively. The reflectance and the transmittance of the film can subsequently be obtained by

$$\mathcal{R}_{s,p} = \left(\frac{\eta_{0(s,p)} B_{s,p} - C_{s,p}}{\eta_{0(s,p)} B_{s,p} + C_{s,p}} \right) \cdot \left(\frac{\eta_{0(s,p)} B_{s,p} - C_{s,p}}{\eta_{0(s,p)} B_{s,p} + C_{s,p}} \right)^* \tag{4.11}$$

$$\mathcal{T}_{s,p} = \frac{4\eta_{0(s,p)}\eta_{m(s,p)}}{(\eta_{0(s,p)} B_{s,p} + C_{s,p}) \cdot (\eta_{0(s,p)} B_{s,p} + C_{s,p})^*} \tag{4.12}$$

$$\mathcal{A}_{s,p} = 1 - \mathcal{R}_{s,p} - \mathcal{T}_{s,p} \tag{4.13}$$

In this work, the TMM was used to determine the reflectance $\mathcal{R}$, transmittance $\mathcal{T}$ and absorptance $\mathcal{A}$ spectra for thin film arrangements. To be able to adapt these characteristics onto a specific problem, two different evolutionary algorithms have been used. For both algorithms, a fitness criterion of a filter structure for a given application has to be chosen that can be calculated from the reflectance and/or transmittance values. If the aim is a filter structure that shows a high reflectance between 900 nm and 1200 nm and additionally a high transmittance between 1200 nm and 1500 nm, the fitness indicator F could be determined according to

$$F = \sum_{900\,\mathrm{nm}}^{1200\,\mathrm{nm}} \mathcal{R} + \sum_{1200\,\mathrm{nm}}^{1500\,\mathrm{nm}} \mathcal{T}. \tag{4.14}$$

The genetic algorithm is aiming to increase this fitness value F. As the choice of materials sets the refractive indices of the layers, the thicknesses of the various layers are taken to be variable for a defined number of layers. The fitness is calculated for a random starting configuration of thicknesses. In the next step, the thicknesses are "mutated", meaning they are modified by the addition of random values. The fitness of the new configuration is calculated. If this generation shows a higher fitness indicator than the previous one these thicknesses are taken to be the new

starting configuration and they are again mutated. If the fitness is lower, the starting thickness values are mutated again. This process is repeated for a large number of steps until a steady-state is reached, which means that a local or global minimum has been found.

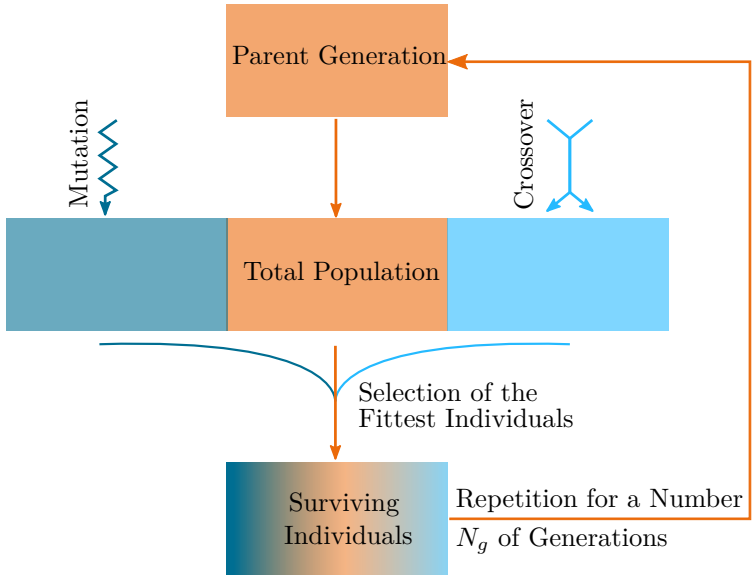

Figure 4.2: Sketch of the optimization using a genetic algorithm (adapted from [130]).

The second algorithm has been implemented by Oliver Höhn and basically does the same thing in a more advanced way, here a large number of random starting configurations, the ”parents” are taken and modified not only by ”mutation” but also by ”crossover” of the best configurations resulting in a new generation of ”children”. From this total number of configurations, those with the best fitness are taken to survive and act as a new ”parent-generation”. This optimization procedure is sketched in Figure 4.2. The end of the simulation is reached after a certain number of generations N_g has been simulated. An overview over evolutionary

algorithms is given in [132].

Using these algorithms, a stack of layers could be optimized for its reflectance and transmittance characteristics in a certain wavelength range.

4.2 Scattering Matrix

The scattering matrix (S-Matrix) approach presents a second possibility to determine the electromagnetic field distribution and the reflectance, transmittance and absorptance characteristics for a structure in which the refractive index varies only along one dimension. This approach is physically equivalent to the TMM but uses a different mathematic approach as the electric and magnetic fields are looked at in $\vec{k}$-space, thus, the Fourier-transform of the fields is calculated [133, 134].

The fields are separated into waves traveling forwards and backwards through the film assembly with amplitudes $\vec{a}^i$ and $\vec{b}^i$, where each amplitude is described by two perpendicular field components. All possible polarizations can be obtained by a linear combination of these field components. These amplitudes are propagated for $\vec{a}^i$ from the top to the bottom and for $\vec{b}^i$ from the bottom to the top of the structure using the matrix $\hat{\mathcal{M}}^i$ and the phase propagation contained in the $\hat{f}^i$-matrices in a layer-by-layer approach. The tangential fields within layer i can be obtained by

$$\begin{pmatrix} \vec{e}^i(z) \\ \vec{h}^i(z) \end{pmatrix} := \begin{pmatrix} E_x^i \\ E_y^i \\ \omega\mu_0 H_x^i \\ \omega\mu_0 H_y^i \end{pmatrix} = \hat{\mathcal{M}}^i \cdot \begin{pmatrix} \hat{f}_+^i(z) & 0 \\ 0 & \hat{f}_-^i(z) \end{pmatrix} \begin{pmatrix} \vec{a}^i \\ \vec{b}^i \end{pmatrix}, \tag{4.15}$$

where the matrix $\hat{\mathcal{M}}^i$ includes the dielectric properties of layer i and the matrices $\hat{f}^i{}_+$ and $\hat{f}^i{}_-$ describe the phase propagation of the amplitudes

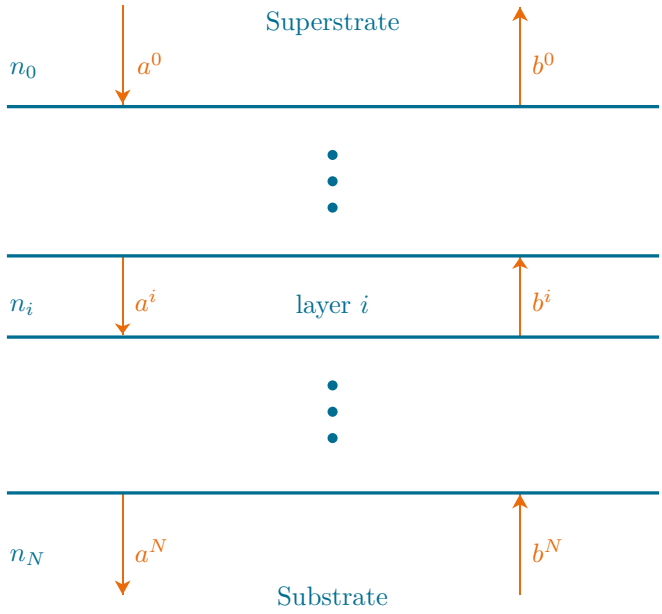

Figure 4.3: Sketch of the simulation setup for the S-Matrix method (adapted from [130, 133, 134]).

$\vec{a}^i$ and $\vec{b}^i$ from the upper and lower boundary of the layer. This relation can be deduced from Maxwell's equations under the assumption of plane waves and the representation of the field in $\vec{k}$-space where the dielectric constant only depends on the z-coordinate.

Thus, a so-called scattering matrix $\hat{S}^i$ can be obtained that connects the field amplitudes in layer i to those in the adjacent layer j [133, 134].

$$\begin{pmatrix} \vec{a}^i \\ \vec{b}^j \end{pmatrix} = \hat{S}^i \cdot \begin{pmatrix} \vec{a}^j \\ \vec{b}^i \end{pmatrix} \tag{4.16}$$

Looking at this relation, the differences between the S-Matrix approach and the TMM can be explained. The scattering matrix connects the forward and backward traveling modes in layer i with the corresponding

modes in the adjacent layer j, whereas the TMM connects the field components at the boundaries of a specific layer. Thus, for this approach, the evanescent fields at the boundaries lead to rather high non-propagating fields, which might lead to very large field components and thus numerical instabilities [134].

As the fields are calculated within the layers and not at the boundaries, dipole emitters can be implemented at an artificial boundary [134] using the S-Matrix-approach. This leads to a discontinuity at this artificial boundary, which does not cause any problems in the S-Matrix approach as the forward and backward traveling modes are calculated in their propagation directions, the forward traveling wave propagates the dipole emission to the bottom whereas the backward traveling wave propagates the emission to the top of the structure. For the TMM, this is not as easily accessible.

The implementation used in this work was developed in a work of Florian Boedicker [135] using the free software package GNU Octave [136, 137].

The S-Matrix method has been applied as a second method to determine the reflectance, transmittance and absorptance spectra of layered structures. Furthermore, the near-field distribution within the layers and the emission of a dipole within the layers could be simulated using this method.

4.3 Band Structure Calculations

One possibility to determine the photonic density of states (DOS) of a structure are band structure calculations, where the Master equation (Equation 3.10) is solved numerically for different $\vec{k}$-vectors [81]. Thus, the dispersion relation $\omega(\vec{k})$ can be obtained for a specific direction of $\vec{k}$.

An integration over the $\vec{k}$-states of the first Brillouin zone for a given frequency $\omega(\vec{k})$ gives the density of states at this frequency $\rho(\omega)$ [101] as shown in Equation 3.11.

The local information required for the local density of states (LDOS) $\rho(\omega, \vec{r})$ can be obtained by taking the field distributions of each state into account and can be described as [101, 138] according to Equation 3.14.

In this work, I used MIT photonic bands (MPB), a frequency-domain solver [139]. It inherently only works for periodic structures, as it is based on a Bloch ansatz for the fields.

The eigenvalue problem for the given structure is solved for a specific $\vec{k}$-vector with the frequency ω using a plane-wave basis. From this, the dispersion relation can be obtained. Furthermore, the fields can be determined for this specific solution of the eigenvalue problem.

The calculation of photonic band structures has been used to gain a deeper understanding of the origin of peaks in the reflectance characteristics for periodic structures. Additionally, this method presents another possibility to determine the LDOS of periodic structures.

4.4 Rigorous Coupled Wave Analysis

The rigorous coupled wave analysis (RCWA) presents a numerical method that has first been implemented to determine the diffraction properties of grating structures. In principle, it can be applied to all types of structures that are periodic in one, two or three dimensions. The method has first been described in the 1960s for sinusoidal surface gratings [140, 141]. In the 1980s and 1990s, the method has been applied to one or two-dimensional binary gratings [142–144] and extended to obtain the near-field information [145]. It is based on a solution of Maxwell's equation for

a loss-less, homogeneous incident medium, a periodic structure and a substrate medium. An incident field impinges on the periodic structure, for example a grating, under the angle θ_0 with respect to the surface normals shown in Figure 4.4. An additional angle ϕ can be specified against the periodicity of the structure.

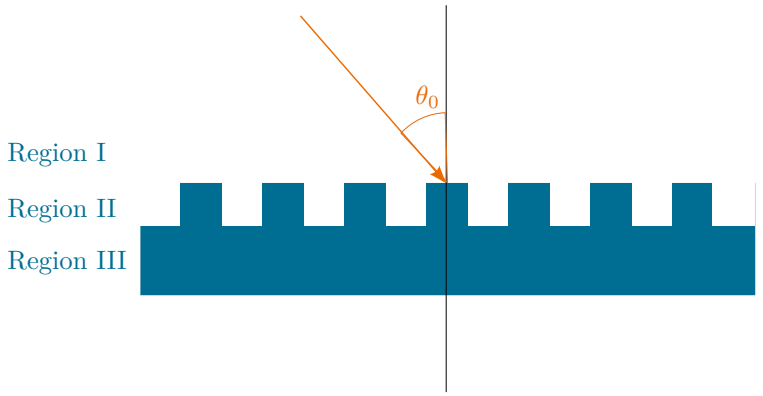

Figure 4.4: Example for an RCWA simulation (adapted from [143]).

The derivation of this simulation method follows [146, 147]. As the super- and substrate consist of homogeneous media, the diffracted fields can be determined by Rayleigh expansion. In the grating region, this is not possible due to the inhomogeneity in the electric permittivity ϵ. However, as ϵ is periodic in at least one dimension, it can be described as a Fourier-series. Thus, the electromagnetic fields can as well be described as a Fourier-series over the tangential components of the $\vec{k}$-vectors of the modes in super- and substrate [143, 144].

$$E_p(y)(\vec{r}) = \sum_{p=-\infty}^{\infty} F_p(z) exp(i(k_{p,x}x)) \tag{4.17}$$

where $F_p(z)$ corresponds to the normalized amplitude of mode p.

Subsequently, Maxwell's equations are solved for the Fourier-expansions of the fields using the respective boundary conditions for the boundary to the superstrate and the substrate. This leads to a set of ordinary differential equations where the amplitudes for the Rayleigh-modes can be obtained from the solution of the eigenvalue problem.

In principle, this simulation method relies on a correct solution of the Maxwell equations, thus, its accuracy is only determined by the number of Fourier modes which are considered within the calculation.

To obtain not only the far-field information about the transmitted and reflected waves but also the near-field information, Lalanne *et al.* proposed a simulation method where only those field components that are continuous at the grating boundaries are expanded into Fourier-series. All other field components are determined from the constitutive relations [145]. This leads to more accurate results than taking the Fourier-expansion of all fields, as many Fourier-components are required to represent the discontinuities in the fields.

The implementation used within the scope of this work is the Matlab-based Reticolo2D code programmed by Philippe Lalanne and coworkers [148].

The RCWA has been used to determine the irradiance distribution within the grating structures. Due to the higher dimensionality these results could not be obtained by the simple TMM or S-Matrix methods and the RCWA-calculations were much faster than the corresponding finite-difference time-domain (FDTD)-calculations.

4.5 Finite-Difference Time-Domain

4.5.1 Theory of the Finite-Difference Time-Domain Method

The FDTD method presents a very general tool to solve Maxwell's equations. It offers the possibility to simulate arbitrary structures and geometries in one, two or three dimensions. Thus, it presents the most general simulation mechanism used in this work. The $\vec{E}$- and $\vec{H}$-field components are simulated on a grid of lattice points at defined time-steps. Hence, time as well as space is discretized with a defined grid, where the temporal discretization is determined from the spatial discretization according to Equation 4.18 [149] and the spatial discretization has to be small enough to ensure that the field components do not change significantly between two lattice points, thus the spacing between two lattice points has to be only a fraction of the smallest medium wavelength used in the setup.

$$\sqrt{(\Delta x)^2 + (\Delta y)^2 + (\Delta z)^2} > c \cdot \Delta t \tag{4.18}$$

where Δx, Δy and Δz correspond to the distance between two lattice points in x-, y and z-direction, c is the speed of light and Δt is the length of a time-step.

The major drawback of the FDTD-method is its relatively high memory requirement as the $\vec{E}$ and $\vec{H}$-field components have to be stored for each lattice point for three time-steps to be able to determine the temporal evolution of the field. Thus, for a cubic lattice, 18 components have to be stored for each space cell as shown in Figure 4.5 [150], leading to a very high memory requirement for large computational areas.

The discretization of the grid is based on the so-called Yee-grid published in 1966 [149]. The lattice points on which the electric and the

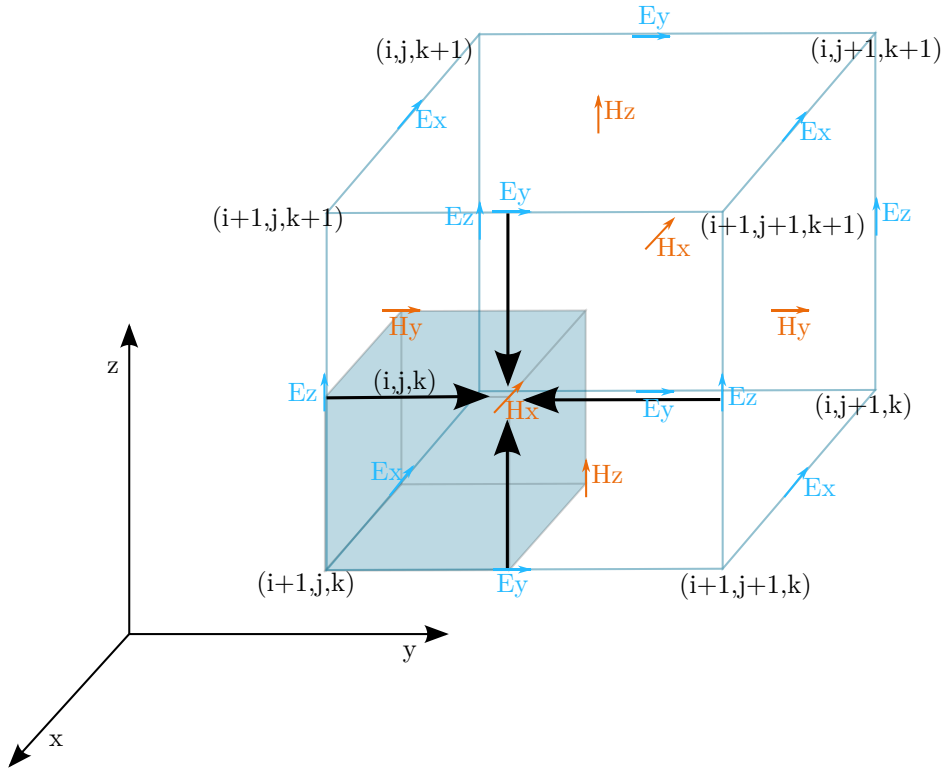

Figure 4.5: Yee-grid for the FDTD-algorithm (adapted from [149])

magnetic fields are calculated are separated by half a discretization step, thus, the space derivatives are determined by a central-difference approximation and are, therefore, second-order accurate [150]. Furthermore, the field components are calculated in a "leapfrog"-manner, first the $\vec{E}$-field components on the grid are calculated using the data for the $\vec{H}$-field obtained from the previous half time-step. The new $\vec{H}$-field components are subsequently calculated from the stored $\vec{E}$-field components [149, 150].

As the field components are stored at lattice points, the computational area has to be limited by boundaries that can have different properties:

- perfectly metallic boundaries: Here, the tangential $\vec{E}$-field components are set to zero at the boundaries
- periodic boundary conditions (PBCs): This type of boundary conditions is used to simulate structures, which are periodic in at least one spatial direction. To simulate this, the field components at one side of the computational area are connected to those at the opposite edge.
- perfectly matched layers (PMLs): If a structure is not periodic or limited by metal in all directions, an additional layer is required, which absorbs the outgoing fields before they reach the actual boundary. The most commonly used type of absorbing boundary conditions are PMLs. Independently of the actual boundaries, the fields at the edges of the simulation domain are absorbed without parasitic reflections in these additional layers. This type of absorbing boundary conditions has been proposed by [151] and is based on a splitting of the electric and magnetic field components in the absorbing boundary region. Thus, the split fields can be attenuated individually [150–152].

4.5.2 MIT Electromagnetic Equation Propagation

For this work, MIT electromagnetic equation propagation (Meep) was used, a freely-available software package for FDTD simulations [153]. Within this code, several features are already implemented, for example the possibility to limit the computational area with PMLs or an interpolation method that enables the reading of field components as well in between time-steps or between lattice points. The structure geometry is introduced using geometric objects which limit regions with certain refractive indices. Here, absorbing media can be introduced as well as perfectly

dielectric structures.

The sources are implemented as current sources and various profiles can be introduced including continuous waves or Gaussian pulses. The first one is determined by the field component, the corresponding emission frequency, and the source position, which can be either a single lattice point, a line or a plane to obtain either a point-source or a homogeneous illumination with a plane wave in two or three dimensions. For the second type of sources, additionally, the frequency width and the center frequency has to be set. Due to Fourier transformation, the Gaussian pulse in the frequency-domain also has a Gaussian shape in the time-domain.

All simulations are started by turning the emission of the source on and end-criteria include a stop after a given time t or a decay in the amplitude of a defined field component by a certain factor at a specific lattice point. The vacuum speed of light c is set to 1 for all calculations.

4.5.3 Simulation of the Irradiance Distribution

To determine the irradiance distribution within a periodic structure, like for example the grating structure sketched in Figure 4.6, the structure is placed at the bottom of the calculation domain. To simulate a periodic structure in x-direction, PBCs are implemented in this direction, whereas the simulation domain is limited by PMLs in y-direction. As the structure does not vary in z-direction, the simulations are carried out in a two-dimensional setup. Thus, a linear source can be used to simulate a plane-wave illumination. This source is placed at a distance of ten wavelengths away from the structure to prevent near-field coupling of the source and the structure. The source emits monochromatically at a wavelength of 1523 nm. The illumination with s- and p-polarized waves is simulated simultaneously. As the simulation is carried out in the time-domain, one

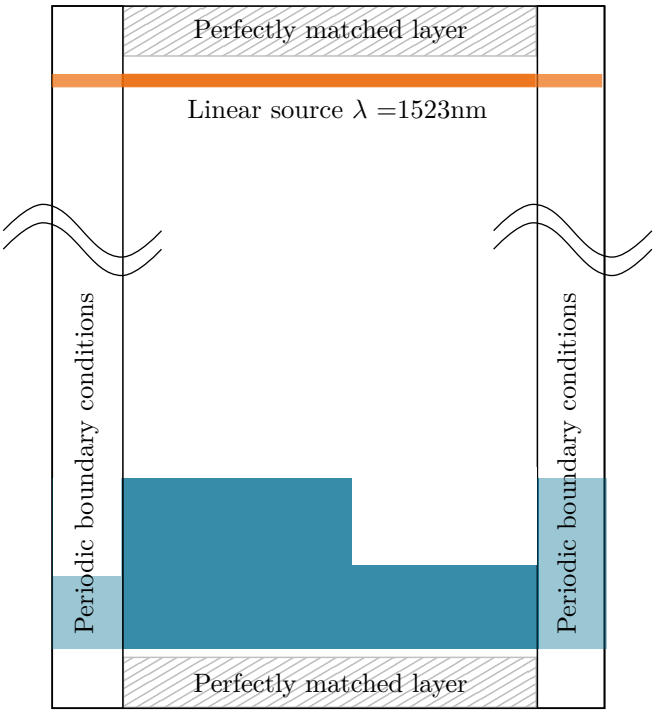

Figure 4.6: Simulation setup to determine the irradiance enhancement for the example of a grating structure periodic in x-direction

has to wait until a steady-state is reached to obtain the field distribution within the structure.

After this steady-state is reached, the time-averaged irradiance I can be extracted from the simulation data. This irradiance is proportional to the photon flux for a monochromatic source.

The irradiance at the position $\vec{r}$ is determined according to

$$I(\vec{r}) = n \cdot E(\vec{r})^2, \tag{4.19}$$

with E being the electric field component.

For the coupling of photonic structures with upconverters, the local variation factor of the irradiance γ_{E} is an important parameter. This factor is determined as the ratio of the local irradiance within a certain structure I_{struct} at the position $\vec{r}$ to the irradiance I_0 that is determined for the same source placed in a homogeneous medium with the refractive index of the upconverter material.

$$\gamma_{\mathrm{E}}(\vec{r}) = \frac{I_{\mathrm{struct}}(\vec{r})}{I_0} \tag{4.20}$$

4.5.4 Simulation of the Local Density of States

To determine the variation factor $\gamma_{\mathrm{if}}(\vec{r})$ of the LDOS due to the photonic structure, further FDTD-simulations were used. In contrast to the previous case, where a line source was placed outside the grating structure, for this application a point dipole emitter inside the structure is simulated [116, 121, 154]. Additionally, the emission is no longer monochromatic but has a Gaussian shape in the frequency domain. This Gaussian shape offers the opportunity to cover a certain frequency range in a single simulation run. The emission of a Gaussian pulse in the frequency domain implies a Gaussian-modulated sine wave at the center frequency in the time-domain.

The variations of the LDOS were carried out in a two-dimensional setup instead of real three-dimensional space. This restriction was necessary to keep the computational efforts within reasonable limits. However, this limitation neglects one dimension in which the refractive index stays constant, thus, the effect on the LDOS is overestimated in the simulations. One approach to get closer to these simulated results could be structuring in two dimensions.

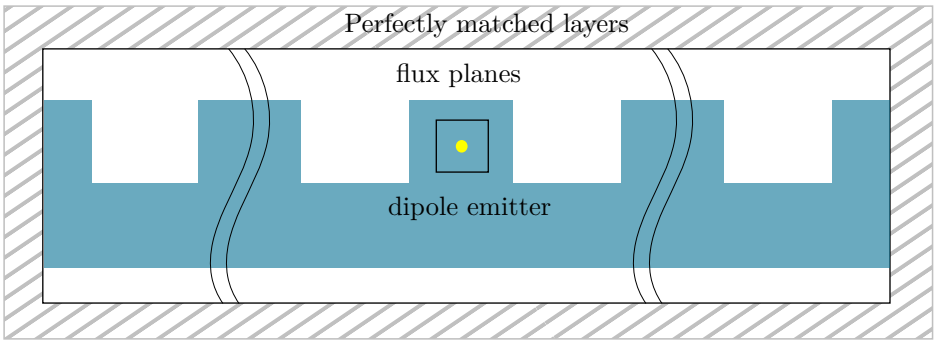

Figure 4.7: Simulation setup for the evaluation of the transition enhancement factor.

The point dipole source is placed within the structure and surrounded by four detector planes as sketched in Figure 4.7. Meep, the simulation software used here, allows for direct recording of the Poynting vector $\vec{S}$ in the frequency domain over the area $\vec{A}$ of these flux detection planes. The emitted energy is measured in these detector planes as the waves pass through, and the data is directly Fourier-transformed. Thus, after the simulation run, the emitted energy $\mathcal{E}(\omega_{if}, \vec{r})$ is obtained spectrally resolved according to [17]:

$$\mathcal{E}(\omega_{if}, \vec{r}) = \frac{\partial \int_{\vec{A}} \vec{S}(\omega, \vec{r}) d^2\vec{r}}{\partial \omega}|_{\omega_{if}} \Delta\omega. \tag{4.21}$$

In principle, this method has been demonstrated in [154]. Inside the photonic structure environment, the initially Gaussian shape of the emission is distorted. The emitted energy $\mathcal{E}$ at the transition frequency ω_{if} is proportional to the LDOS $\rho(\omega, \vec{r})$ at this frequency. Thus, the relative enhancement factor for this frequency γ_{if} (ω_{if}) can be obtained by dividing the emitted energy $\mathcal{E}_{\text{struct}}(\omega_{if})$ at the transition frequency ω_{if} by the corresponding unperturbed values taken from a reference simulation in a

homogeneous medium with a refractive index equal to the upconverter material ($n_0 = 1.5$) [17]. This is important as the DOS and with this also the LDOS depends on the refractive index.

$$\gamma_{if}(\vec{r}) = \frac{\mathcal{E}_{\text{struct}}(\omega_{if}, \vec{r})}{\mathcal{E}_0(\omega_{if})}. \tag{4.22}$$

As the LDOS is a local quantity, this procedure has to be repeated for a sufficiently dense grid of sampling positions.

For these simulations, the computational cell had to be extended for several periods in x-direction, compared to the previously used where only one period of the structure was simulated with periodic boundaries. In principle, we would like to simulate an infinitely extended structure, however, here, periodic boundaries would imply that field components leaving in negative x-direction re-entered the simulation cell from the positive x-direction and would be counted in the detector planes, leading to wrong results. The simulation results shown here were typically obtained in simulation runs covering 25 periods of the grating structure to minimize the effects of the boundaries, followed by PMLs.

Furthermore, at each lattice point the emission has to be simulated for all possible dipole orientations. The dipole can be oriented along the x-axis, the y-axis or perpendicular to the simulation cell. All possible dipole orientations can be covered in one simulation run.

In order to quantify the effects of a photonic structure environment on upconversion processes, a description of these processes is required.

4.6 Rate-Equation Model

One of the most suitable materials for upconversion of near-infrared photons above the band gap of silicon is hexagonal sodium yttrium tetraflu-

oride doped with trivalent erbium (β-$NaYF_4$:Er^{3+})[30]. The erbium ions can be excited at a wavelength of around 1523 nm and the most important upconversion emission occurs at 980 nm. Subsequent absorption of photons or energy transfer between neighboring ions can lead to the emission of these higher-energy photons.

This material has been investigated theoretically and a rate-equation model has been developed describing the upconversion dynamics [28, 45]. The model describes absorption, emission, energy transfer, and multi-phonon relaxation processes in β-$NaYF_4$:Er^{3+}. All relevant transitions for the upconversion of infrared photons at a wavelength of 1523 nm within a trivalent erbium ion are considered. An occupation vector $\vec{n}$ describes the relative occupation of the six lowest energy level, thus, the fraction of ions of a large ion ensemble that is excited to this state.

The occupation vector $\vec{n}$ and its rate of change $\dot{\vec{n}}$ are described by the differential equation

$$\dot{\vec{n}} = [GSA + ESA + STE + SPE + MPR] \cdot \vec{n} + \vec{v}_{ET}(\vec{n}). \tag{4.23}$$

The matrix GSA describes the ground state absorption, ESA the excited state absorption, STE the stimulated emission, SPE the spontaneous emission and MPR the multi-phonon relaxation processes. These processes are proportional to the occupation vector. The more complex energy transfer processes $\vec{v}_{ET}(\vec{n})$ which are not linear in $\vec{n}$ are described by a set of vectors [28].

The model is based on experimentally determined Einstein coefficients [28, 45]. Starting from these values, the matrix entries for GSA, ESA, STE and SPE were determined. For the stimulated processes, additionally, the local irradiance has to be considered. If the irradiance is increased

locally, the stimulated processes are scaled by the factor $\gamma_{\mathrm{E}}(\vec{r})$ as determined from Equation 4.20:

$$GSA_{\mathrm{struct}}(\vec{r}) = \gamma_E(\vec{r}) \cdot GSA_0 \tag{4.24}$$

$$ESA_{\mathrm{struct}}(\vec{r}) = \gamma_E(\vec{r}) \cdot ESA_0 \tag{4.25}$$

$$STE_{\mathrm{struct}}(\vec{r}) = \gamma_E(\vec{r}) \cdot STE_0. \tag{4.26}$$

The second effect of the photonic structure onto the upconversion process is the modified LDOS. This affects the Einstein coefficients for the spontaneous emission A_{fi} from all excited states according to Fermi's golden rule [85]. Thus, these coefficients are multiplied by the factor γ_{if}, which is determined from the emission simulations (see Equation 4.22) [17].

$$A_{if,\mathrm{struct}}(\vec{r}) = \gamma_{if}(\vec{r}) \cdot A_{if,0}. \tag{4.27}$$

For the absorption the final state is an electronic state which is independent from the photonic LDOS, therefore, the absorption rate is considered to be independent from the transition enhancement factor $\gamma_{\mathrm{if}}(\vec{r})$. If the absorption is independent of the LDOS, the stimulated emission processes have to be also independent of the LDOS as these quantities are related only by the degeneracies of the energy levels (see Equation 3.23).

During the last few years, there has been an extensive debate in literature whether energy transfer processes between the erbium ions are significantly influenced by the change of the LDOS [78–80]. Here, we consider the energy transfer processes to be independent of the LDOS. This assumption follows the argument of de Dood *et al.* [78]. They reasoned

that the energy of the virtual photons involved in the energy transfer covers a very broad range due to their short lifetime, therefore, the effect of the LDOS at a specific theoretically determined transition energy plays a negligible role.

Including the effect of the irradiance enhancement and the variation of the LDOS, the rate-equation model can be used to quantify the effects of the photonic structure on the upconversion processes. The absorption rate Abs is determined as the sum over GSA- and ESA- processes from the initial state minus the STE from excited states leading to the emission of a photon at the excitation wavelength of 1523 nm [28]. The matrices describing these processes are multiplied by the occupation of the corresponding energy levels, where $\vec{n}_1$ describes the occupation of the ${}^4I_{15/2}$ ground state, $\vec{n}_2$ describes the occupation of the ${}^4I_{13/2}$ first excited state and so on.

$$\begin{aligned} Abs = \vec{n}_1 \cdot GSA + \vec{n}_2 \cdot ESA + \vec{n}_4 \cdot ESA \\ - \vec{n}_2 \cdot STE - \vec{n}_4 \cdot STE - \vec{n}_6 \cdot STE. \end{aligned} \tag{4.28}$$

The absorption enhancement γ_{Abs} and its mean value $\overline{\gamma_{\mathrm{Abs}}}$ are defined as

$$\gamma_{\mathrm{Abs}}(\vec{r}) = \frac{Abs_{\mathrm{struct}}(\vec{r})}{Abs_0}, \tag{4.29}$$

$$\overline{\gamma_{\mathrm{Abs}}} = \frac{\sum_{i=1}^{M} \gamma_{\mathrm{Abs}}(\vec{r_i})}{M}. \tag{4.30}$$

Abs_0 describes the absorption of a homogeneous upconverter. The mean value $\overline{\gamma_{\mathrm{Abs}}}$ is determined as sum over all absorption enhancement values divided by the number of points M.

The luminescence rate of a specific transition is obtained by a multiplication of the the population of the starting energy level and the spontaneous

emission Einstein coefficient for the specific transition from level f to level i [28]. The most important emission for the upconverter material hexagonal sodium yttrium tetrafluoride (β-$NaYF_4$):20% Er^{3+} occurs at 980 nm and corresponds to the luminescence from the $^4I_{11/2}$-level to the ground state. Thus, we are mainly interested in improving the luminescence from this level.

$$Lum = \vec{n}(3) \cdot A_{31}. \tag{4.31}$$

The luminescence enhancement γ_{Lum} and its mean value $\overline{\gamma_{\mathrm{Lum}}}$ are defined as

$$\gamma_{\mathrm{Lum}}(\vec{r}) = \frac{Lum_{\mathrm{struct}}(\vec{r})}{Lum_0}, \tag{4.32}$$

$$\overline{\gamma_{\mathrm{Lum}}} = \frac{\sum_{i=1}^{M} \gamma_{\mathrm{Lum}}(\vec{r_i})}{M}. \tag{4.33}$$

Here Lum_0 describes the luminescence from a homogeneous upconverter. The mean value $\overline{\gamma_{\mathrm{Lum}}}$ is determined as sum over all luminescence enhancement values divided by the number of points M. From this absorption and luminescence rates, the internal upconversion quantum yield (iUCQY) for all transitions can be obtained. Again, we are mainly interested in the transition from the second excited state to the ground state.

The quantum yield can subsequently be related to the quantum yield of the unchanged upconverter system iUCQY_0 to obtain an enhancement factor γ_{iUCQY} for the iUCQY. The mean $\overline{\gamma_{\mathrm{iUCQY}}}$ over the whole structure with M points is determined according to

$$\gamma_{\mathrm{iUCQY}}(\vec{r}) = \frac{iUCQY_{\mathrm{struct}}(\vec{r})}{iUCQY_0}, \tag{4.34}$$

$$\overline{\gamma_{\mathrm{iUCQY}}} = \frac{\sum_{i=1}^{M} \gamma_{\mathrm{Lum}}(\vec{r_i})}{\sum_{i=1}^{M} \gamma_{\mathrm{Abs}}(\vec{r_i})}. \tag{4.35}$$

5 Experimental Methods

This chapter describes the materials and the experimental methods that have been used in this work. First the material system of hydrogenated amorphous silicon carbide (a-Si_xC_{1-x}:H) is described, which has the advantage that the refractive index of this material can be varied with the composition. This offers the possibility to prepare one-dimensional filter structures using only one material system. The layers can be deposited with plasma-enhanced chemical vapor deposition (PECVD). These filters can be used in a system which combines a silicon solar cell with upconverter material or to build a cavity into which upconverter material can be embedded to determine the influence of a photonic structure environment on upconversion processes. For this second application, upconverter nanoparticles have to be embedded into a suitable host material, in this case polymethylmethacrylate (PMMA) was used. Thin layers of this material can be prepared by spin-coating. Furthermore, linear gratings within upconverter materials are investigated. These grating structures can also be produced from the spin-coated layers if a master structure is hot-embossed into the layer. The last section describes the two main characterization methods used in this work: ellipsometry and photoluminescence measurements in an integrating sphere setup. Most processes described here have also been used and are, therefore, described in the diploma thesis of Sebas-

tian Wolf [130], which I supervised.

5.1 Fabrication of Amorphous Silicon Carbide Layers

5.1.1 Properties of Amorphous Silicon Carbide

Within this work, the material system of a-Si_xC_{1-x}:H was chosen to realize multilayer structures acting as spectrally selective filters. These filters can be used in a system, which combines silicon solar cells with upconverter material and a second luminescent material (see Figure 2.3). Another application for these filters is a cavity system where a thin layer of upconverter material is embedded between two filter structures and the upconversion properties are influenced by the photonic structure environment. A very extensive review about the properties of this material is given in [155]. With this material a rather broad range of refractive indices can be covered, which offers high flexibility for filter design. The refractive index in this material system can be tuned with the silicon to carbon ratio of the film [155]. It ranges from about a value of 1.7 for amorphous carbon up to around 3.3 for amorphous silicon. The drawback of the high-index silicon-rich films is that they tend to have an island-like growth [156], thus, it is difficult to obtain thin closed layers. As the films are hydrogenated the film density and refractive index depends as well on the hydrogen incorporated in the film.

As a-Si_xC_{1-x}:H is an amorphous semiconductor with a band gap of around 1.7 eV to 2.6 eV [157] it shows some absorption in the visible range of the spectrum. As the filters are to be used only at the rear side of a silicon solar cell, this does not cause parasitic absorption. Photons in this wavelength range are absorbed in the silicon and are not able to reach the filter structures.

5.1.2 Plasma-Enhanced Chemical Vapor Deposition

There are various deposition methods for thin films which are categorized according to the aggregation state of the precursors. Those that are based on gaseous precursors and hence are vacuum-based technologies are subsequently divided into physically or chemically based deposition. Opposed to the physical vapor deposition (PVD)-methods where a precursor material is typically evaporated from a source and deposited on the substrate, the chemical vapor deposition (CVD)-methods include a chemical reaction. The gaseous precursors are transported to the substrate and react near or at the surface (see Figure 5.1) to form the product thin film. This chemical reaction leads to a solid phase on the substrate surface and an additional volatile compound. The energy required for the reaction (to produce the reactive species from the gaseous precursors and for nucleation and growth of the film) can be provided either by heating the substrate to temperatures of several hundred degrees Celsius or for example by a plasma, which reduces the required substrate temperature. The latter process is called PECVD. Additional to the deposition process, there are various other processes including the reverse reaction and desorption of the precursors (etching), surface diffusion of the intermediates and in the case of PECVD ionic bombardment of the thin film. Here, the film structure and compositions can be influenced by the plasma parameters [158].

PECVD is widely used for the deposition of a-Si_xC_{1-x}:H using silane (SiH_4) and methane (CH_4) as precursor gases in an argon plasma [159–161]. It has been shown that the reproducibility of layers under the same plasma conditions is good [159]. Petrich *et. al* have shown that sp^3-hybridized carbon is present in all configurations using C^{13}-nuclear magnetic resonance (NMR) [160]. The sp^3-hybridized carbon is typically hy-

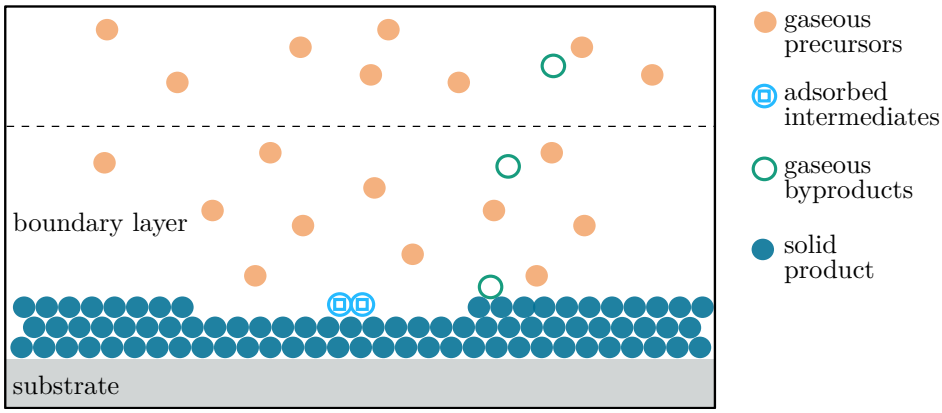

Figure 5.1: Sketch of a chemical vapor deposition process (adapted from [158])

drogenated whereas the sp^2-carbon usually has no bound hydrogen [160]. The hydrogen originates either directly from the precursor molecules or from additional hydrogen that is added to the reactor chamber to stabilize the plasma [162].

To produce good quality filter structures, closed, homogeneous layers of thicknesses in the range of 50nm to 300nm are required. A high reflectance can be reached by increasing the number of layers or by increasing the refractive index contrast (n_{high}/n_{low}) between the layers. Using a third layer with intermediate refractive index did not improve the filter characteristics in simulations (see Section 6.3) and thus, the most simple configuration of two alternating layers was investigated. Thus, two different processes were required to obtain a high-index and a low-index layer, which resulted in homogeneous, closed layers. Additionally, the deposition rates should be at around 2 nm/s or less to ensure that the layers can be deposited with the required accuracy. As described above, silicon-rich layers show an island-like growth mechanism [156] and are, therefore, not suited for

this application. This restriction gave the upper limit for the refractive index.

All a-Si_xC_{1-x}:H layers were produced in an AK-400M reactor built by Roth and Rau. CH_4 and SiH_4 were used as precursor gases which react in an argon plasma. The plasma is additionally diluted with hydrogen to obtain a more homogeneous deposition. It was also found that the addition of H_2 leads to higher Si/C ratios [163]. This increase in silicon content is expected to originate from predominant reactions of H-atoms with SiH_4 to form SiH_3 radicals and with CH_3 radicals to form CH_4 close to the film surface [163]. The gas flow rates for CH_4 and SiH_4 are controlled by mass flow controllers (MFCs) and can be regulated from a minimum gas flow of 7 standard cubic centimeter per minute (sccm) to a maximum of 150 sccm. The argon gas flow for all processes was set to 30 sccm to obtain stable plasma conditions. The pressure within the reaction chamber was set to 0.05 mbar. Changing the chamber pressure influences the film composition and growth of the layers: a higher pressure leads to more ionic bombardment of the film surface. The maximum process pressure is 1 mbar. The chamber can be evacuated to a pressure of 10^{-6} mbar and the samples are introduced via a load lock to minimize the amount of oxygen within the deposition chamber. For this work, two different approaches to power the plasma were used:

Coupled Microwave and Radio-Frequency Deposition The plasma used in these processes is powered by a combination of a radio frequency (rf)-source at a frequency of 13.56 MHz and a power of 150 W and two additional microwave (MW)-sources at a frequency of 2.54 GHz with a power of 1 kW each [164]. The combination of sources improves the decomposition of CH_4, which is much more stable than SiH_4. To change the refractive index of the layers the gas flow rates of the precursor gases were adapted. For the low-index (high-index) layer,

the CH_4 flow rate was set to 110 sccm (50 sccm) and the one for SiH_4 to 7 sccm (50 sccm). These processes are based on those used in [162] and had the advantage that they were well known and the deposition parameters were well established.

Pulsed Microwave Deposition After a modification of the reactor chamber, pulsed MW-sources were available for the processes. Thus, new processes were developed using these sources to power the plasma. For these processes, the gas fluxes for the high index layers were slightly adapted to a SiH_4 flow of 60 sccm and a CH_4 flow of 40 sccm. For the low-index layers, the gas flow rates were left unchanged. The MW-power for each source was set to 1500 W, which was on for 10 ms and off for 17/18 ms respectively. Using these processes, a better homogeneity could be obtained over a larger area.

5.2 Fabrication of Upconverter-Doped PMMA-layers

To embed the upconverter materials into the photonic structures, thin layers in the range of a few hundred nanometer containing the upconverter material are required. This presents a challenge as the most efficient upconverter materials are typically in a micro-crystalline state. However, there have been enormous advances in producing upconverter nanoparticles [35], so these were chosen to demonstrate the positive impact on upconversion. For this purpose, however, the upconverter nanoparticles have to be embedded in a transparent matrix.

5.2.1 Upconverter Nanoparticles

The synthesis and characterization of lanthanide-based upconverter nanoparticles has drawn a lot of attention during the recent years [35, 36, 42].

These lanthanide-based materials have the potential to show upconversion from the near infrared (NIR) above the band gap of silicon.

The synthesis methods that are applied to obtain nanoparticles include mechano-chemical and combustion synthesis methods [42] as well as wet-chemical processes based on a nucleation and growth mechanism [38]. The latter process offers a great flexibility and a good control of the particle sizes as the fabrication can be separated into a nucleation and a growth phase. If low temperatures can be applied, these processes can result in upconversion nanoparticles, which are capped with organic ligands, and can therefore be dispersed in an organic solvent [36]. These suspensions can subsequently be used to embed the nanoparticles into a polymer. One approach to do this is to disperse the Nanoparticles (NPs) which were capped with polyethylene glycol (PEG) monooleate in methylmethacrylate (MMA) and carry out a direct radical polymerization [43]. Using this process, a doped bulk PMMA block can be obtained. For the combination with photonic structures, however, very thin layers of the doped polymer are required. Therefore, a different approach was used: the nanoparticles were stabilized with PEG monooleate [44] and transferred into toluene, the same solvent that has been used for PMMA and a suspension of PMMA, β-$NaYF_4$:Er^{3+} and PEG monooleate was produced which could be used for spin-coating.

The upconverter nanoparticles used in this work have been produced by my colleague Stefan Fischer at the University of Victoria in an unpublished work. They consist of a β-$NaYF_4$:Er^{3+}-core and an undoped $NaLnF_4$-shell and are dispersed in hexane. Adding ethanol to the solution leads to a precipitation of the nanoparticles. The mixtures are produced at a ratio of (NP+PEG):PMMA=1/3 and (NP+PEG+PMMA):Toluene=1/9.

5.2.2 Properties of PMMA

PMMA is a polymer that is formed by polymerization of methyl methacrylate monomers [165]. Its repeat unit is shown in Figure 5.2.

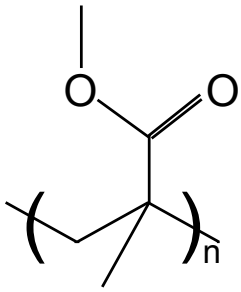

Figure 5.2: Repeat unit of a PMMA-macromolecule.

PMMA is soluble in organic solvents like for example toluene and thin layers of the material can be prepared in a spin-coating process from the solution. The glass transition temperature depends on the tacticity and for the atactic conformation has a glass-transition temperature of around 105 °C [166–168]. PMMA has good optical properties, as it shows a very high transparency from the visible range to the infrared (IR). Furthermore, it features a refractive index of $n = 1.49$ [167], which matches the refractive index of β-$NaYF_4$ quite well. Thus, it is a suitable material to embed the upconverter nanoparticles, which does not lead to significant light scattering and has also been used as a matrix material by other groups [43].

5.2.3 Spin-Coating

Together with PMMA, the upconverter nanoparticles can be dissolved in toluene. For this, the nanoparticles had to be transferred from hexane

to toluene. Adding ethanol to the solution started a precipitation of the nanoparticles, which were subsequently separated from the solvent in a centrifuge at 5000 rpm for 6 min. This process was repeated twice and the additional solvent was decanted. The nanoparticles, which precipitate to the bottom, are subsequently dispersed in 5 ml toluene and additionally, 500 mg of PEG were added to the solution to stabilize the particles in PMMA. Additionally, 15 ml of PMMA dissolved in toluene were prepared. These two solutions were subsequently mixed to obtain a solution of 10 wt% PMMA to toluene with 25 wt% nanoparticles in PMMA. This suspension was stirred for several hours at room temperature until a clear solution was obtained. It was then used in a spin-coating process to obtain thin layers of doped PMMA on a glass substrate in a controllable way. As reference samples, additional undoped PMMA-layers were produced.

For spin-coating, 250 µl of the solution were dropped onto a substrate placed on a chuck and which then started spinning for 60 s. During the rotation, a thin film is formed on the substrate, whose thickness is determined by the adhesion of the film on the substrate and the centrifugal force. Thus, the film thickness can be tuned with the concentration of the solution and the spin velocity. The film thickness increases with the viscosity and hence with the concentration of the solution and decreases with increasing spin velocity. The substrate can be rotated prior to adding the solution or the spin process can be started after the solution has been added and the spin velocity can be ramped. Furthermore, the amount of solution, which is added onto the substrate, and the choice of solvent, more precisely its vapor pressure, plays a role as a part of the solvent is evaporated during the process. Within this work, the choice of solvent was limited to toluene.

All films produced in this work were produced in a G3P-8 spin coater from Speciality Coating Systems. The glass substrates were washed with

ethanol, dried and additionally washed with isopropanol and dried with nitrogen. Subsequently, 250 µl of the solution are pipetted onto the middle of the substrate, which leads to a complete wetting of the substrate. The spinning process is then started and the spin velocity is ramped to reach its final value within 1s to avoid significant evaporation of the solvent prior to reaching the final settings. The substrate was subsequently rotated for 60 s. After the deposition, the samples were heated to 40 °C for 10 min to evaporate the residual solvent.

For the dependence of the film thickness d on the spin velocity ω_r and the solvent concentration $\mathcal{C}$, an empirical model was used that has been developed in [169]:

$$d = D \cdot \mathcal{C}^{\alpha} \cdot \omega_r^{\beta}. \tag{5.1}$$

Here, D, α and β are empirically determined parameters.

As the solvent high-performance liquid chromatography (HPLC)-grade toluene from Roth was used, the PMMA used had a molecular weight of 120.000 g/mol and was ordered from Sigma-Aldrich.

5.2.4 Hot-Embossing

Hot-embossing is used for two different purposes within the scope of this work. First, two substrates coated with layers of PMMA can be combined in a hot-emboss process [170] under elevated temperatures and pressure in a Dr Collin plate press 200P. This is used to form the cavity structure. Second, a similar process is used to imprint a grating structure into the PMMA-layers from a silicone stamp. With this process, a grating with embedded upconverter material could be obtained.

During hot-embossing the layers on glass substrates are placed on top of each other with the PMMA-layers facing each other. To reach a homogeneous pressure distribution over the sample surface and avoid cracking, additional polytetrafluorethylene (PTFE)-foils are placed on top of and below the samples. To obtain a good contact between the layers without any air inclusions the sample chamber is evacuated and the pressure is subsequently increased to a value of 10 MPa. The temperature is increased to 100 °C and kept for 12 min. This temperature is slightly below the glass transition temperature of the used PMMA, which lies at around 105 °C for atactic PMMA under normal pressure [166–168]. Subsequently, the temperature is decreased slowly under constant pressure to reduce thermal stress. This process has been developed by Sebastian Wolf during his diploma thesis [130]. The maximum pressure is given by the mechanical stability of the glass substrates.

A similar process can be used to imprint a structure into a layer of doped PMMA. Using this process, a given master structure can be transferred into an upconverter layer. A silicone stamp is used to mold the master structure and this stamp is subsequently embossed into the doped PMMA-layer.

5.2.5 Stamp Production

For the grating structures, a master structure has been produced by electron-beam lithography at the Friedrich-Schiller-University (FSU) in Jena. For this purpose, a silica wafer was structured and metallized with chromium. From this master, a double-layer silicone stamp has been produced. A hard top-layer of the stamp is required to preserve the structure and the softer bulk material is needed to obtain a good contact between the stamp and the PMMA-layer into which the structure is embossed. The

whole process chain is sketched in Figure 5.3.

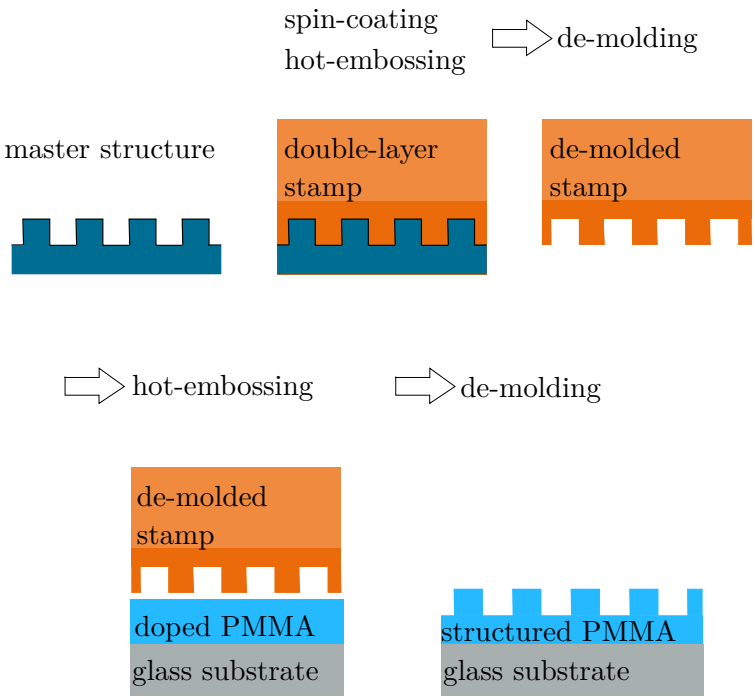

Figure 5.3: Sketch of the process chain used to transfer a grating into PMMA.

This double-layer silicone stamp was realized by first depositing a thin layer of hard polydimethylsiloxane (PDMS) onto the master structure. For this hard layer, 3.4 g of a vinyl PDMS pre-polymer (VDT-731) is mixed with 18 µl of a platinum catalyst (SIP 6831) and 4.5 µl of a modulator. Subsequently, 1.0 g of hydrosilane pre-polymer (HMS 301) is added and stirred. This mixture is then spin-coated onto the master and evacuated for 1 min. Subsequently, the sample is cured for 30 min at 60 °C. This procedure was described in [171]. The soft bulk PDMS is produced as a

mixture of 31.5 g silicone and 3.5 g hardener. This mixture is stirred for 4 min under vacuum and poured into an aluminum frame which has been placed on top of the coated master. A glass plate that has been previously treated with a primer to improve the bonding to the PDMS, was placed on top of the aluminum frame. To improve the adhesion between the two layers of PDMS, the whole stack was hot-embossed with a maximum pressure of 1 bar and a maximum temperature of 60 °C for 60 min. The complete stamp can then be detached from the master structure and used to transfer the grating structure into a spin-coated PMMA-layer in a hot-emboss process.

5.3 Characterization

5.3.1 Ellipsometry

Ellipsometry presents a non-destructive method to measure the thicknesses and optical properties of thin films. The method uses the reflection of light at a sample surface and evaluates the Fresnel reflection coefficients r_s and r_p for s- and p-polarized light, respectively, thus, the ratio of the reflected to the incident electric field components for the two polarization states. The s- and p- polarized fractions are separated in a rotating analyzer (see Figure 5.4).

A Woollam M2000 spectroscopic ellipsometer has been used in this work, which offers the possibility to scan a wavelength range from 250 nm to 1000 nm.

The ratio between the s- and p-polarized Fresnel coefficients is described by:

$$\frac{r_p}{r_s} = \frac{E_p^{out}/E_p^{in}}{E_s^{out}/E_s^{in}} = \tan(\Psi_{ell}) \cdot e^{i\Delta_{ell}} \tag{5.2}$$

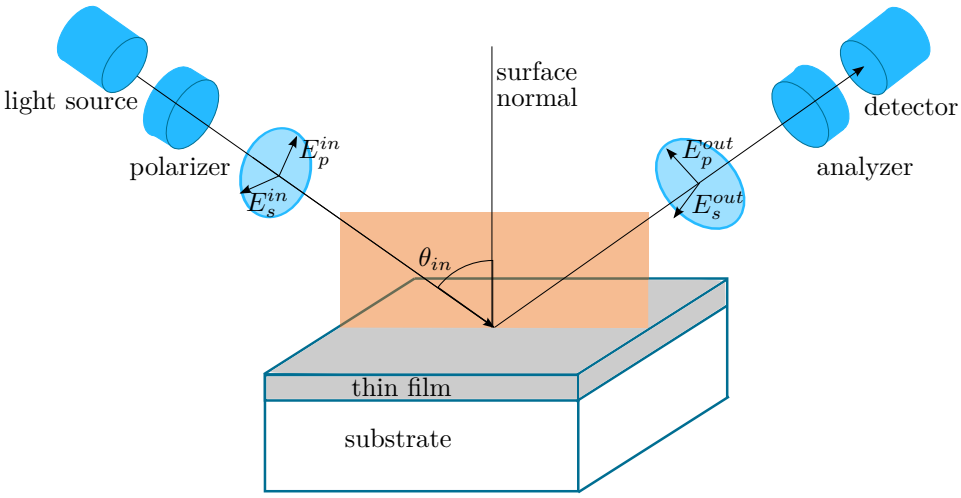

Figure 5.4: Setup for an ellipsometry measurement.

where E_p^{in} and E_p^{out} (E_s^{in} and E_s^{out}) are the incident and reflected part of the electric field in p- (s-) polarization, $\tan(\Psi_{ell})$ describes the amplitude ratio and Δ_{ell} describes the phase change. The measurement signal has its maximum, if the incident angle θ_{in} is chosen to be close to the Brewster angle.

If the sample is homogeneous, if rear-side reflections can be neglected and if it is measured in air, the values for the relative permittivity ϵ_r of the layer can be obtained by direct inversion from Ψ_{ell} and Δ_{ell}:

$$\epsilon_r = \sin^2(\theta_{in}) \cdot \left[1 + \tan^2(\theta_{in}) \cdot \left(\frac{1 - \tan(\Psi_{ell}) \cdot e^{i\Delta_{ell}}}{1 + \tan(\Psi_{ell}) \cdot e^{i\Delta_{ell}}} \right)^2 \right]. \tag{5.3}$$

For all other cases, for example thin films on a substrate, the number of unknowns (complex refractive index for each wavelength and thickness of the film) exceeds the amount of measured data. To reduce the number

of unknowns, a model is used that describes the optical properties of the film. This model together with the layer thickness is subsequently adapted until it reproduces the measured Ψ_{ell}- and Δ_{ell}-values.

Within the context of this work, mainly two different models were used to determine the characteristics of the thin films: for the PMMA-layers, which show no absorption within the measured range, a Cauchy-model has been used. This model does not include any absorption within the film. For the a-Si_xC_{1-x}:H-layers, a Tauc-Lorentz model [172, 173] has been used. This model is very commonly used for the description of amorphous semiconductors and ensures Kramers-Kronig consistency of the real and imaginary part of the permittivity ϵ_r.

5.3.2 Luminescence Measurements in an Integrating Sphere

To quantify the effects of the photonic structure environment on the upconversion process, the main characterization method used here is the measurement of the upconversion luminescence signal. The sample is illuminated with a Santec ECL-210 NIR laser at a wavelength of 1523 nm to excite the $^4I_{13/2}$-state within an erbium ion. As described in Chapter 2, under this illumination, the most important upconversion signal occurs at a wavelength of 980 nm originating from the radiative transition from the $^4I_{11/2}$-state to the ground state, which had been excited by energy transfer upconversion.

The measurement is carried out inside an integrating sphere to capture all emitted light, regardless of the exit plane and direction. The samples are fixed on a centermount sample holder and placed in the middle of the integrating sphere (as shown in Figure 5.5). The laser beam hits the sample surface and a part of the light is absorbed within the upconverter layer. The part of the light that is not absorbed within the layer hits the

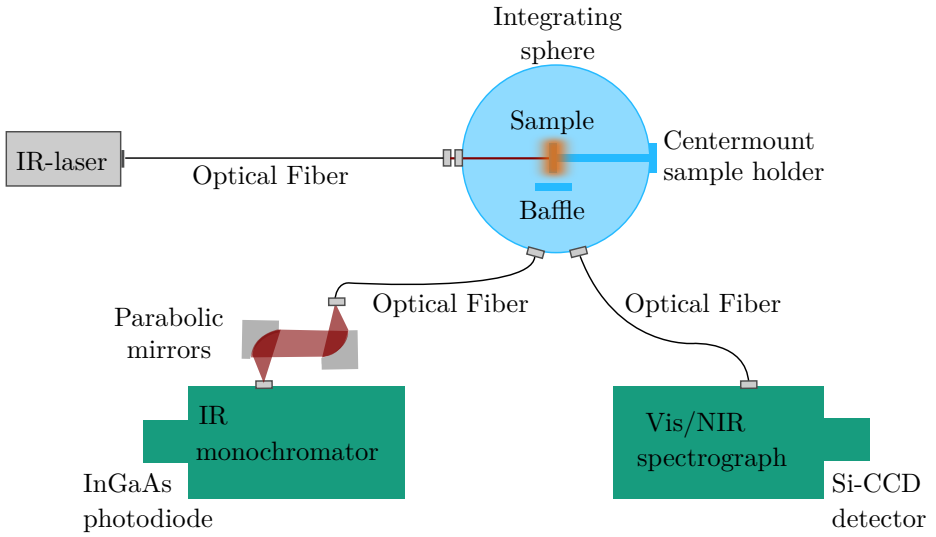

Figure 5.5: Sketch of the measurement setup for luminescence measurements.

surface of the integrating sphere and is scattered. The direct path from the sample to the detectors is blocked by a baffle. This ensures that all the light is scattered before it reaches the detector. The laser signal is monitored using a H25 monochromator from Jobin-Yvon with a moving gold grating and an indium-gallium-arsenide photodiode measuring the photon flux. The luminescence signal of the sample in the visible and near infrared is measured in a Princeton SP2300i spectrograph with aluminum grating and silicon charge coupled device (CCD)-detector. In this spectrograph, the grating is fixed and the whole spectrum can be recorded at once.

As the quantum efficiency of the Princeton detector is highly wavelength dependent, a measurement of the known spectrum of a tungsten lamp is used to determine a spectral correction function $f_{vis,NIR}$. The measured signal is subsequently corrected using this correction function. Based on

the measured luminescence signal $S(\lambda)$, a figure-of-merit Lum representing the luminescence from the ${}^4I_{11/2}$-state around a wavelength of 980 nm was defined that can be compared to the Lum determined in the simulations:

$$Lum = \int_{\lambda_{lum,low}}^{\lambda_{lum,high}} S(\lambda) \cdot f_{vis,NIR}(\lambda) d\lambda, \tag{5.4}$$

where $\lambda_{lum,low}$ and $\lambda_{lum,high}$ are determined as the wavelengths where the signal disappears in the background signal.

Using this setup, one can not only measure the luminescence signal but in principle also the absorption of the samples. For this purpose, additionally to the upconverter samples, reference samples are produced that imitate the optical properties of the samples, lacking only the upconverter absorption. In this work, typically structures with undoped PMMA were used as a reference. The corresponding measurement method to determine the absorption, is described in [174]. First, the width of the exiting laser beam, characterized by the lower limiting wavelength $\lambda_{exc,low}$ and the upper limit $\lambda_{exc,high}$, is determined in a measurement with empty sample holder inside the integrating sphere. In a second measurement, the signal is recorded with the sample inside the holder to obtain $S_{exc,sample}$. Finally, a measurement is performed with the corresponding reference sample to obtain $S_{exc,ref}$. The sample absorption Abs can then be determined as the difference between the integrated excitation signals:

$$Abs = \int_{\lambda_{low}}^{\lambda_{high}} S_{exc,ref} d\lambda - \int_{\lambda_{exc,low}}^{\lambda_{exc,high}} S_{exc,sample} d\lambda. \tag{5.5}$$

The sample is tilted at an angle of 4° against the laser axis to ensure that the zero order reflex does not directly leave the integrating sphere through the laser entrance opening.

In principle, it would be possible to determine the upconversion quantum yield (UCQY) of the samples from the ratio of luminescence to absorption if one additionally takes into account the different sensitivities of the two different detectors. However, for the samples used here, the absorption was very small as very thin layers were used and the absorption coefficient is rather small as well. Furthermore, the absorption is determined as the differences of two rather large values, with only small differences due to the low absorption. So even if the relative uncertainty of the original values is small, it means that large uncertainties occur for the absorption. It was found that the sensitivity of this setup was not good enough to measure the absorption of the very thin layers of upconverter material. Thus, also no statements could be made for the effects of the photonic structure on the UCQY. For this reason, the experimental results focus on the luminescence enhancement.

6 Simulation of Photonic Structures

Photonic structures for two different applications are investigated theoretically in this chapter: first, the use of photonic structures as filters to guide photons to the regions where they can be used most efficiently for a system consisting of a silicon solar cell and upconverter material, described in Section 6.3 and second, the embedding of upconverter material directly into a photonic structure is described in Sections 6.4 to 6.6. In the second approach, the photonic structure influences the local irradiance and the LDOS, so these quantities were simulated and taken into account in a rate-equation model for β-$NaYF_4$ doped with 20 % Er^{3+}. Furthermore, convergence analyses were carried out for all methods used, shown in Section 6.1, and the validity of the methods was checked by comparing the results of different methods wherever possible as shown in Section 6.2.

6.1 Convergence Analyses

6.1.1 Simulation of the Irradiance Distribution

For the two different numerical methods used in this work, namely, the FDTD- and the RCWA-method (see Sections 4.5 and 4.4), different parameters influence the accurateness of the simulation results. For the FDTD-method, these are the resolution of the lattice and the runtime of the simulation, as this is a time-domain simulation. For the RCWA, the results depend on the number of Fourier-components considered in the simulations. The convergence analyses were carried out for the grating-waveguide structure described in Section 6.6, the most complex structure used in this work.

For the FDTD-simulations, the runtime required to reach a steady-state obviously depends on the distance between the source and the structure, the further away the source, the longer the light has to travel until it reaches the structure and a steady state can be reached. Thus, a smaller distance between the source and the structure would reduce the required simulation time. However, if the source is close to the structure, near-field coupling between the source and the structure influences the emission and the source does not emit in the same way as it would in a homogeneous medium. The effect of this distance is also investigated. The squared absolute value of the electric field component is taken as a parameter to determine the convergence of the simulations. This parameter is proportional to the irradiance. Figure 6.1 shows the convergence analysis for the runtime of the simulation in periods of the emission wavelengths $\lambda_{\text{emission}}$ and for the resolution of the grid. It shows that a good convergence is obtained for a runtime of 200 periods but the resolution required is at least 130 pt/µm. This high resolution not only increases the storage require-

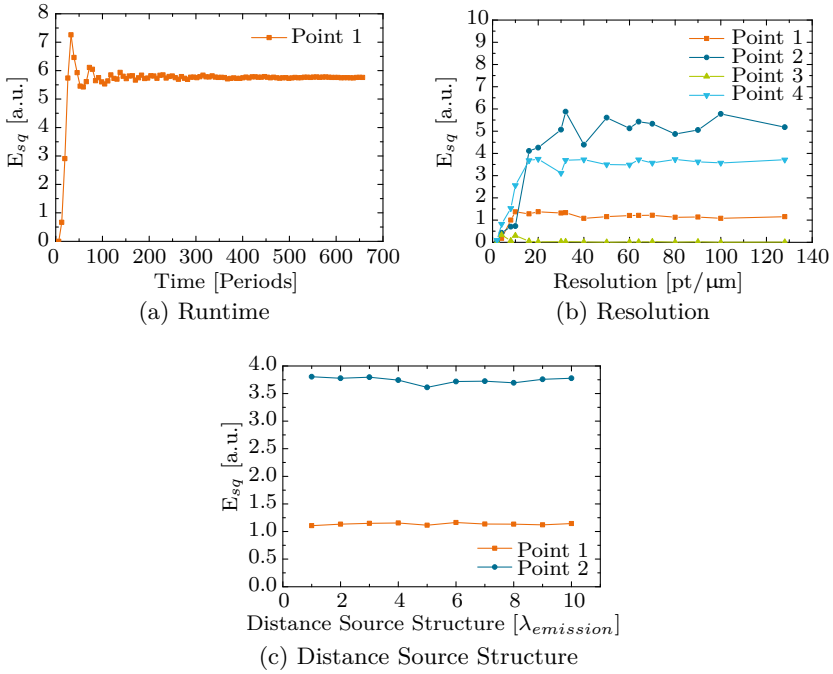

(a) Runtime (b) Resolution

(c) Distance Source Structure

Figure 6.1: Convergence analysis for the dependence of the irradiance distribution on the resolution of the grid and the runtime.

ments, it also increases the time required for a simulation run, as a higher resolution also requires a smaller time step according to Equation 4.18. The distance between the source and the structure was set to 10 $\lambda_{emission}$ to ensure that the structure does not influence the emission.

For the RCWA the parameter that has to be checked for convergence is the number of Fourier components that is used to describe the fields. To check for convergence, again the squared electric field is investigated at two different points in the structure (see Figure 6.2). This parameter varies with the number of Fourier components used in the simulation setup until a steady state is reached at around 15 Fourier components.

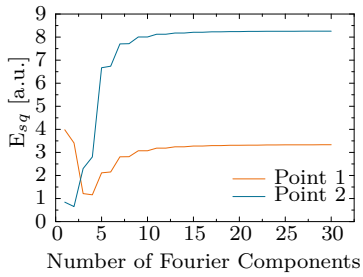

Figure 6.2: Convergence analysis for the number of Fourier components required for the RCWA simulations.

Thus, for the FDTD a resolution of at least 130 pt/µm and a runtime of at least 200 periods would be required to reach a steady state. On the other hand, the results determined from the RCWA-simulations show a very good convergence from 15 Fourier components. Hence, as a better convergence could be obtained with less computational efforts using the RCWA-approach, the simulations for the irradiance distribution were typically carried out using this method.

6.1.2 Simulation of the Local Density of States

As mentioned above, speaking of LDOS, I refer to the photonic density of states. Within this work, the variations in this quantity was determined using the FDTD-method, as with the RCWA- and the TMM-approaches it is not possible to implement sources within the structure. For the S-Matrix, the implementation of a dipole source is possible but this dipole is not able to emit in the x-y-plane. The simulation setup for these simulations is described in Subsection 4.5.4. As in the previous subsection, the resolution has to be checked, but here, there are further parameters that may influence the results. The width of the Gaussian pulse of the excitation and its center frequency play a role as towards the edges of the

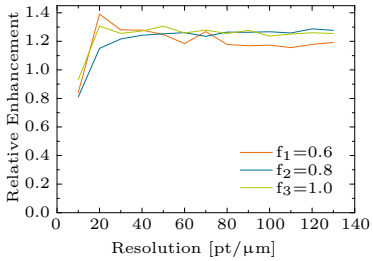

(a) Resolution

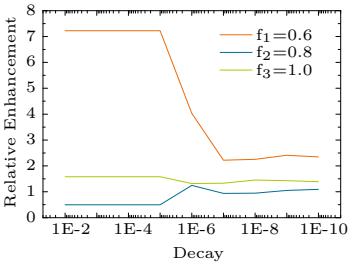

(b) Decay

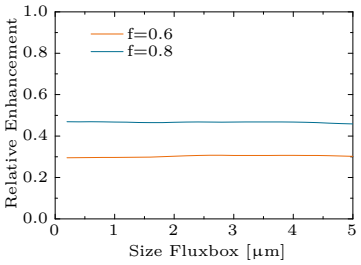

(c) Size of the Fluxbox

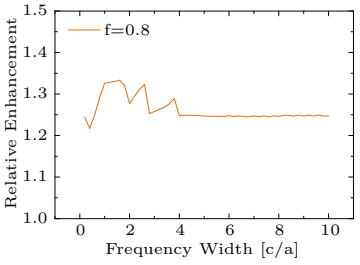

(d) Frequency Width of the Pulse

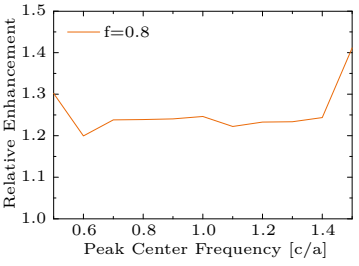

(e) Center Frequency of the Peak

Figure 6.3: Convergence analysis for the dependence of the local density of states on a) the resolution, b) the fraction of the fields to which the field has to decay until the simulation is stopped, c) the size of the box through which the flux is measured, d) the frequency width of the Gaussian emission, and e) the center frequency of the Gaussian emission.

pulse, the components become very small and as the enhancement factor is determined from a ratio between two very small values, its uncertainty becomes quite large. Furthermore, the size of the box was varied to see if it has an influence on the results. The last parameter that can be set in the simulation is the value to which the field has to decay before the simulation is stopped.

Figure 6.3 shows the convergence analysis for the different parameters. For all parameters, the relative enhancement factor is plotted against the respective converging parameter. This enhancement factor was determined by dividing the simulated flux by the flux obtained in a reference simulation where the emission takes place in a homogeneous medium.

As shown in Figure 6.3, the resolution for the simulation setup should exceed 70 pt/µm, the field should decay to a fraction of 10^{-7} of its maximum value, and the size of the fluxbox does not influence the enhancement factors. The frequency width should exceed a value of $4c/a$ to ensure that the investigated frequencies do not lie too close at the edges of the pulse where the uncertainty of the results increases. The center frequency of the Gaussian peak that is emitted by the source does not play a role unless the frequency of interest is very close to the edges of the pulse, in this case, the errors on the emission enhancement factor become large as they result from the division of two very small values.

The values determined in this convergence analysis were used in the following simulations unless stated otherwise.

6.2 Comparison of Simulation Results Using Different Methods

To validate the different methods, the same systems were simulated using different methods.

6.2.1 Reflectance and Transmittance of Thin Film Arrangements

The reflectance and transmittance of a thin-film arrangement can in principle be determined by all methods used here. As for this purpose, only the TMM and the S-Matrix approach were used for the one-dimensional systems and the RCWA for the grating structure, here we only compare these three methods for a one-dimensional system.

The system used for this comparison of methods was a cavity-filter, which was optimized for high reflectance below 1000 nm and high transmittance at 1523nm consisting of 17 layers of alternating refractive indices of $n_{\text{high}} = 2.5$ and $n_{\text{low}} = 1.8$ without absorption in this range. The thicknesses of the various layers lie between 40 nm and 160 nm.

Figure 6.4 shows the reflectance versus the wavelength of the incident light for normal incidence calculated with the three different methods: the TMM, the S-Matrix approach and the RCWA. It shows very nicely that the same reflectance characteristics are reproduced using the three different methods. For the TMM and the S-Matrix approach, this result is expected, as both methods use an analytic approach and should, therefore, lead to the same exact results. For the RCWA, this result means that the calculations converged very well. The transmittance, which is not shown here, also shows exactly the same characteristics.

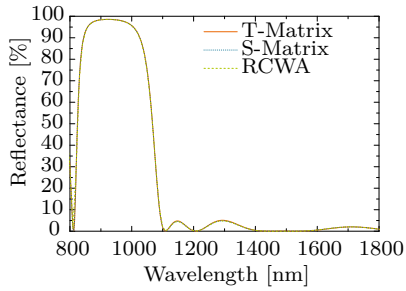

Figure 6.4: Comparison between the reflectance characteristics of a thin film system determined by the transfer matrix approach, the scattering matrix approach, and RCWA.

6.2.2 Irradiance Distribution within a Layered Structure

The irradiance distribution for a one-dimensional system can basically be determined using all simulation methods presented here. However, for the TMM code used in this work, the calculation of the fields was never implemented, this method was only used to determine the reflectance, transmittance and absorptance characteristics of thin film arrangements. Furthermore, the RCWA was only used to determine the irradiance in structures with higher dimensionality. Hence, here, we compare the results for a cavity structure obtained by FDTD and S-Matrix. The cavity consists of a rear-reflector, a buffer layer and two cavity filters with the cavity layer in between. The cavity layer has a thickness of 785 nm and the buffer layer thickness is 400 nm. The filters were especially optimized for the purpose, thus, the cavity filters show a very high reflectance at the emission wavelength of the upconverter of 980 nm and very good transmittance at the incident wavelength of 1523 nm. The structure is illuminated by a plane wave emitting at a wavelength of 1523 nm under normal incidence.

For the FDTD, the source is placed ten medium wavelengths away from

the structure to avoid near-field coupling. The value γ_E shown here represents the relative change in the irradiance within the structure compared to a homogeneous medium with refractive index of $n = 1.5$ and it is plotted versus the position along the $z-$axis within the structure.

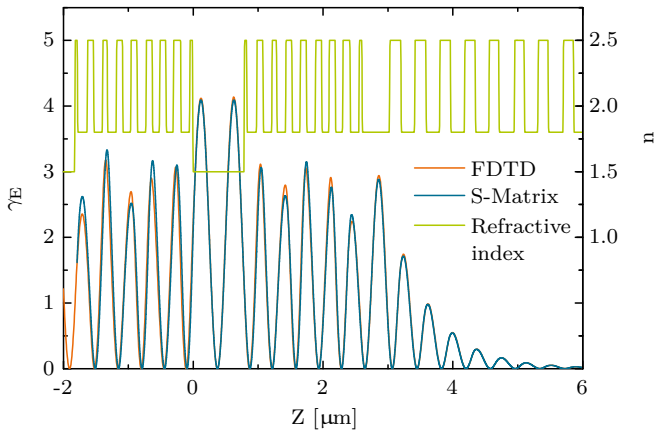

Figure 6.5: Comparison of the local irradiance enhancement factor γ_E within a layered structure obtained by FDTD and S-Matrix simulations. A plane wave with a wavelength of 1523 nm is impinging from the left under normal incidence.

The comparison between the two different methods shows the same trends and the slight differences can be explained due to the fact that FDTD is a numerical approach whereas S-Matrix determines an analytical solution. The numerical approach implies a discrete lattice of points and with that a certain resolution. Furthermore, the steps between layers of different refractive indices are slightly smoothed to account for the finite resolution. Overall, the agreement between the two methods is very good.

6.2.3 Irradiance Distribution within a Grating Structure

To validate the two approaches used to determine the irradiance distribution within the two-dimensional photonic structures, a test structure consisting of a grating with a refractive index $n = 2$ on a metallic mirror in air was implemented and simulated using RCWA and FDTD-simulations. For the RCWA 20 Fourier components were taken into account and for the FDTD, the source was placed ten wavelengths away from the structure and the simulation was run for 500 periods with a resolution of 120 pt/µm.

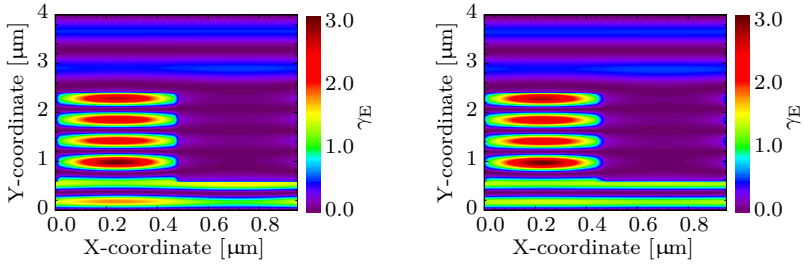

(a) RCWA-calculation (b) FDTD-calculation

Figure 6.6: Comparison of the irradiance enhancement determined by RCWA and FDTD.

Figure 6.6 shows the simulation results for the irradiance enhancement within the structure obtained with the two different methods, which show a very good agreement. There are slight differences at the edges of the grating which can be attributed to the subpixel-averaging that is applied in the FDTD-simulation and leads to a more smooth transition from the high refractive index of the grating to the air region whereas the transition is step-like in the RCWA. These small differences are taken to be negligible and, therefore, the simulations of the irradiance distribution within

the grating structures were carried out using the RCWA-method unless otherwise noted as this dramatically reduced the simulation costs.

6.2.4 Local Density of States in a Layered Structure

In principle, the variations in the LDOS can be determined from the emission of a dipole at each lattice point. The dipole emission at a specific wavelength varies due to the environment, so by relating the emitted flux to the flux emitted in a homogeneous medium, the relative variation in the LDOS is obtained, as described in Subsection 4.5.4. This can be achieved over a certain wavelength range in one simulation run if the simulated emission is not monochromatic but has a Gaussian distribution.

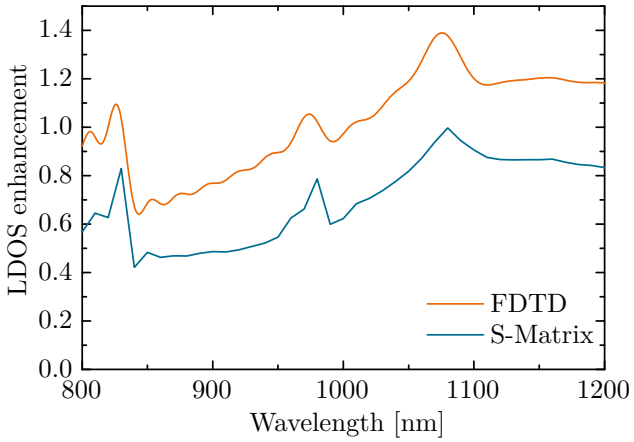

Figure 6.7: Comparison of the relative emission coefficients over the emission wavelength determined by the S-Matrix method and FDTD.

The enhancement factors for the LDOS are shown in Figure 6.7 for a given position within the cavity structure described in Subsection 6.4.1

and were determined by two different methods, the S-Matrix approach and FDTD. The results obtained with the two methods show the same features. However, an offset is visible that can be attributed to the fact that in the S-Matrix calculation, energy propagation within the x-y-plane is not possible, whereas the dipole in the FDTD-calculations can emit in all directions. For the homogeneous reference simulation, the emission is homogeneous over the angle θ, thus the difference is negligible, however, within a structure, it might be the case that a considerable amount of energy is emitted into the x-direction. As this part is not taken account for in the S-Matrix calculations, the result for the relative enhancement are constantly lower than for the FDTD-calculations. However, as the two methods show exactly the same trends, the S-Matrix approach has still been used to determine trends within the structures, due to the advantage in computational effort.

6.3 Transfer Matrix Simulations of Filter Structures

6.3.1 Simulation of Bragg-Structures

The most simple approach to obtain filters with a high reflectance around a certain wavelength is to use so-called Bragg-structures, which consist of layers of two materials with different refractive indices. The thickness of these respective layers depends on their refractive index and the wavelength of maximum reflection λ_{des} according to Equation 3.13. The only variable parameters for these structures are λ_{des} and the number of layers. The refractive indices, which are typically given by the choice of material, together with λ_{des} determines the layer thicknesses, which correspond to a quarter of the design wavelength in the corresponding medium. The design wavelength can be adapted to shift the reflection peak to the desired

position.

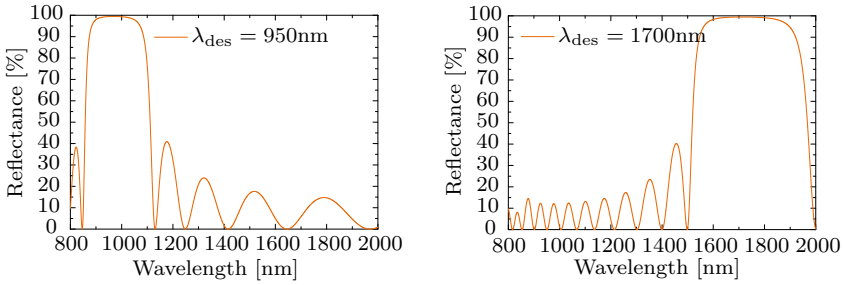

(a) UC-Filter (b) SC-Filter

Figure 6.8: Comparison of the simulated reflectance characteristics of two Bragg-structures consisting of 20 layers each with refractive indices of $n_{high} = 2.5$ and $n_{low} = 1.8$.

Figure 6.8 shows the simulated reflectance characteristics of two different Bragg-structures. The vacuum design wavelength was set to 950 nm and 1170 nm, respectively. The respective filter structures were denoted upconversion (UC)-Filter, and spectral concentration (SC)-Filter, motivated by their role in the system layout presented in Figure 2.3. The UC-filter is responsible for guiding the upconverted photons to the solar cell, whereas the SC-filter is responsible for the spectral concentration. The refractive indices are chosen to have constant values of $n_{low} = 1.8$ and $n_{high} = 2.5$, these values were reached for the first a-Si$_x$C$_{1-x}$:H-layers deposited. These structures not only show a very good and well pronounced reflectance peak, but also the corresponding harmonics and a certain number of side lobes in between. The number of side lobes depends on the number of layers: the more layers, the more side lobes. The harmonics are more easily visible, if the reflectance is plotted against the reciprocal wavelength, corresponding to a plot against the frequency as shown in Figure 6.9.

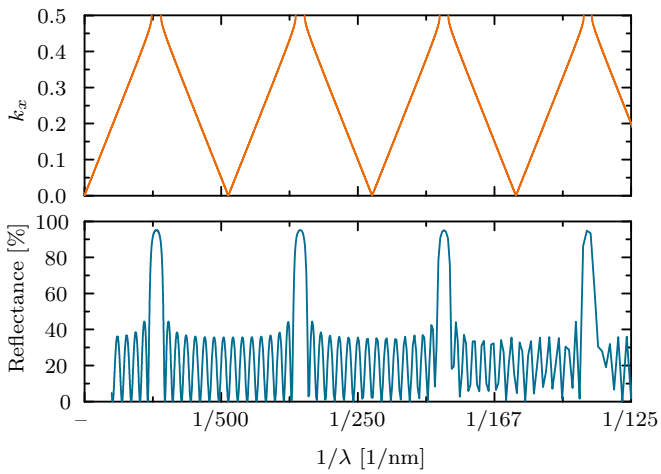

Figure 6.9: Plot of the reflectance of a Bragg consisting of 15 layers with refractive indices of $n_{low} = 1.8$ and $n_{high} = 2.2$ against the reciprocal wavelength in comparison to the bandstructure of the first Brillouin zone. Here the frequency axis of the band structure plot is rescaled to the same reciprocal wavelength axis as in the reflectance plot below. The k_x-component of the wavevector is plotted from 0 to the edge of the first Brillouin zone 0.5 for the 8 first bands.

Figure 6.9 shows the band structure calculated with MPB and the reflectance of a Bragg-structure calculated with TMM plotted against the reciprocal wavelength. This plot shows nicely that the reflectance peaks originate from photonic band gaps at the corresponding wavelengths. The large number of oscillations between two harmonic high reflectance peaks presents the main drawback for the application of this type of filters for systems, where a high transmittance is required in a certain wavelength range as well as a high reflectance peak as in the system shown in 2.3. These oscillations can be reduced if the filters are terminated with layers

of a thickness of $\lambda/8$ instead of $\lambda/4$. Depending on whether the outer layers are layers with a high (or low) refractive index, the side lobes are reduced for wavelengths above (or below) the design wavelength [131].

For the Nanospec System shown in Figure 2.3 two different filter structures are required, they were named UC- and SC-UC-filter. The UC-filter has to reflect photons that can be absorbed in the silicon solar cell (up to a wavelength of around 1150 nm) and must have a high transmittance above this range. The SC-filter reflects photons around the absorption wavelength of the upconverter material (at a wavelength of 1523 nm). A combination with the UC-filter gives the reflectance required at positions, where no upconverter material is present. As the filters were prepared using a-Si_xC_{1-x}:H-layers with different configurations, the dispersion relations of these layers as determined from ellipsometry measurements were used as input parameters for the simulations.

Using simple Bragg-structures with additional layers having a thickness of $\lambda_{des}/8$ at the top and at the bottom of the filter, both types of filters can be produced.

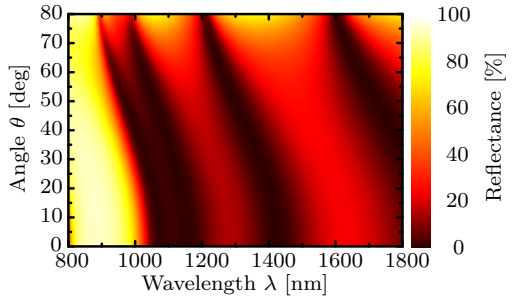

Figure 6.10: Reflectance of an UC-filter based on a Bragg-structure consisting of 15 layers with $\lambda/8$-layers at the top and the bottom of the structure.

The UC-filter can be prepared with a design wavelength of 950nm where

the outer layers are taken to be the high-index layers. A minimum of 15 alternating layers is required to obtain a peak reflectance of 98 % for a refractive index contrast of $n_{\text{high}} = 2.5$ to $n_{\text{low}} = 1.8$. The SC-filter can be produced as a Bragg-structure with a design wavelength of 1700 nm. Here, the outer layers are taken to be the low-index layers. A peak reflectance of 97 % can be achieved with 15 alternating layers for this second Bragg-structure, leading to a complete structure consisting of 30 layers. Figure 6.10 shows the reflectance characteristics of an UC-filter consisting of 15 layers over the wavelength and the angle of incidence

6.3.2 Optimization of Adapted Filter Structures

The reflectance and transmittance characteristics of the Bragg-structures described above can be further improved if the layer thicknesses are varied from the Bragg condition. This was carried out using the two different evolutionary algorithms described in Section 4.1. The number of degrees of freedom of the algorithms is given by the number of layers used. The thickness of each layer can be adapted in order to improve the fitness of the filter, which is determined from an arbitrarily set criterion that weights the reflectance and transmittance within certain important regions. For the UC-filter, the fitness F_{UC} of the filter structure was calculated as the sum over the reflectance values between wavelengths of 800 nm and 1150 nm divided by the sum over the reflectance between 1150 nm and 1700 nm. For the combined SC-UC-filter the fitness $F_{\text{SC-UC}}$ was calculated by dividing the sum over the reflectance values between 800 nm and 1150 nm and between 1500 nm and 1700 nm by the transmittance between these reflectance regions. The division by the transmittance increases its importance for the fitness of the filter structure.

$$F_{\mathrm{UC}} = \frac{\int_\theta \sum_{800\,\mathrm{nm}}^{1150\,\mathrm{nm}} \mathcal{R}}{\int_\theta \sum_{1150\,\mathrm{nm}}^{1700\,\mathrm{nm}} \mathcal{R}} \tag{6.1}$$

$$F_{\text{SC-UC}} = \frac{\int_\theta \sum_{800\,\mathrm{nm}}^{1150\,\mathrm{nm}} \mathcal{R} + \int_\theta \sum_{1500\,\mathrm{nm}}^{1700\,\mathrm{nm}} \mathcal{R}}{\int_\theta \sum_{1150\,\mathrm{nm}}^{1500\,\mathrm{nm}} \mathcal{R}} \tag{6.2}$$

where the incident angle θ runs from 0 to 90 degrees. The number of layers required was set to 21 and reduced later on. According to previous calculations, a very high reflectance of theoretically above 97 % can be obtained for Bragg-stacks consisting of 15 layers. The minimum target peak reflectance was 95 %. The additional layers offer some flexibility for for the evolutionary algorithm, as a variation of the layer thicknesses typically results in a slight reduction of the reflectance in a certain region to be able to improve the transmittance in another region. Additionally, the peak width of the Bragg-stacks is fixed by the center frequency, this parameter can also be tuned to a certain extend by the evolutionary algorithm. One could imagine for example to de-tune the design wavelengths for the two different layers slightly to obtain a broader peak.

As already mentioned, the main goal of the evolutionary algorithm was to increase the transmittance directly besides the peak, for the UC-filter for wavelengths above 1150nm. A high transmittance in this region ensures that all photons that cannot be absorbed by the silicon solar cell reach the upconverter and the Nanocrystalline Quantum Dots (NQDs). For the combined filter structure, the transmittance has to be optimized between 1150 nm and 1500 nm to allow photons between the absorption edge of the silicon solar cell and the absorption of the upconverter to reach the NQDs. The optimization was carried out not only for normal incidence but over the complete angular range from 0 to 90 degrees. Figure 6.11 shows the comparison between the Bragg filters with $\lambda/8$-layers and optimized filter structures for filter structures consisting of 21 layers under normal

incidence.

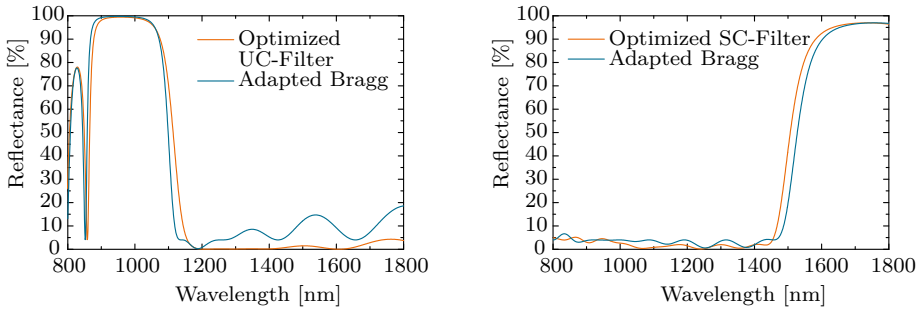

(a) UC-Filter (b) SC-Filter

Figure 6.11: Comparison of the reflectance of optimized filter structures and adapted Bragg-structures for UC and SC-filter consisting of 21 layers, each.

For this stack, the optimization worked very well, as both, the reflectance and the transmittance of the thin-film arrangement in the respecitve regions is improved by the evolutionary algorithm.

In addition to the improvement of the Bragg-stacks, three layer systems were investigated, where the third layer had an intermediate refractive index. Therefore, also stacks with 15 layers were investigated where the refractive index varied in steps. The starting thickness values were taken to be random and the genetic algorithm was run for 200 generations with each generation consisting of 100 individuals.

Figure 6.12 shows that no advantage could be achieved using a three-layer system, the reflectance peak for this particular optimization ended up being broader than for the adapted Bragg-structure and the transmittance above 1150 nm is not considerably improved compared to the simple structure using only two different layers. Thus, these systems were not investigated further as a third layer only increases the complexity of the

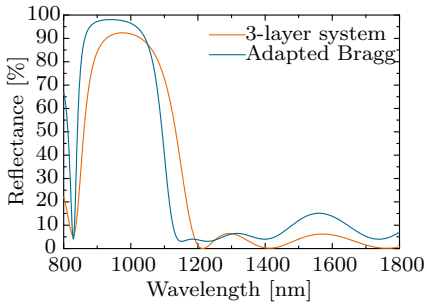

Figure 6.12: Comparison between an adapted Bragg-structure and an optimized system consisting of three different layers consisting of 15 layers each.

deposition as an additional deposition process has to be well controlled.

6.3.3 Comparison of the Robustness of the Bragg and the Optimized Filters against Process Variations

To investigate the robustness of the filter characteristics onto process variations during the deposition-process, the optimized filter configuration as well as the Bragg-structure with the $\lambda/8$-layers were subjected to variations of the layer thicknesses around the optimized values. For realistic conditions, the standard deviation of the deposition rate was determined experimentally. The deposition rate was determined from two time-series that were carried out on two different days at different reactor conditions. A different surface coverage of the reactor walls resulted in variations in the deposition rate. This effect was reduced by a pre-dip with a dense a-Si_xC_{1-x}:H-layer of a thickness of around 50 nm before starting the actual deposition process. As the stacks are deposited in one run, thus, layer by layer without any breaks, it seems to be likely that the deposition rate for each of the processes stays rather constant over the deposition of

the stack. A deposition rate of 51.8 nm/min and 122.9 nm/min with a standard deviation of 0.5 nm/min and 1.7 nm/min was determined for the low-index and the high-index layer, respectively. The standard deviation of the parameters was determined from linear fits of the deposited thickness versus the process time. The experimentally determined values for the standard thickness deviation per deposition time were subsequently taken into account in the simulations using a Monte-Carlo-approach. For this approach, the deposition rate was taken to have a Gaussian distribution around the experimentally determined value using the standard deviation obtained from the fit. For each filter configuration 10000 different thickness vectors were determined using this deposition rate with its standard deviation taking the deposition time as calculated for the fitted deposition rate. Subsequently, the reflectance and transmittance characteristics were determined for these altered thickness vectors.

For the analysis two filter structures, a Bragg-structure and an optimized filter structure, were investigated. Both consisted of 15 layers and should show a very high reflectance up to a wavelength of 1150nm followed by a high transmittance above this wavelength.

	Bragg		Optimized Filter	
	mean	standard deviation	mean	standard deviation
$\mathcal{T}_{\mathrm{av}}[\,\%]$	93.5	0.1	89.3	0.7
$\mathcal{R}_{\mathrm{av}}[\,\%]$	80.2	0.1	72.1	10.3
$\lambda_{\mathrm{max}}[\,\mathrm{nm}]$	1019.8	8.7	1192.4	10.9

Table 6.1: Results of the robustness analysis

The most important results are shown in Table 6.1. The comparison of the stability of the two types of filters on variations of the deposition rates shows that the optimized filter structure investigated here is much

more sensitive to process variations than the Bragg-structure. The mean transmittance for the Bragg-filter is with 93.5 % still very good, for the optimized filter this value is with 89.3 % slightly lower. This is not a dramatic difference, however, the benefit of the optimized filter structures typically arises from the better transmittance. This benefit is apparently not stable over the process variations. Furthermore, the mean reflectance is around 8 % lower for the optimized filter structures compared to the Bragg-structures. Additionally, the wavelength of maximum reflectance $\lambda_{\max}$ is with 1192.4 nm very close to the transmission region for the optimized filters.

These results indicate that the process variations of the used PECVD-deposition processes are too large to benefit from the theoretically improved characteristics of the optimized filter.

6.4 Upconversion in One-Dimensional Photonic Structures

The second concept for the combination of upconverter material and photonic structures investigated here, is to directly embed the upconverter material into photonic structures. This influences the upconversion processes in two different ways. First, the irradiance distribution within the structure is altered due to the presence of the photonic structure, which can lead to a local irradiance enhancement that is beneficial, due to the non-linearity of upconversion processes. Second, the transition rates for all spontaneous emissions are altered due to a varied LDOS. This effect can, in principle, further increase the UCQY as desired transitions can be enforced, whereas undesired ones, like the direct re-emission from the first excited state, can be suppressed. To identify the most promising

transitions to target, in a sensitivity analysis the influence of suppressing/enhancing transitions was investigated using the upconverter model described in Section 4.6 for all transitions that are possible within the model for a very broad range of variation factors ranging from 0.01 to 100.

Figure 6.13 shows the parameters, which influence the UCQY for the most dominant emission from the $^4I_{11/2}$ to the $^4I_{15/2}$ ground state. It shows that the most important lever is the suppression of the direct de-excitation of the $^4I_{13/2}$-level (γ_{21}). Furthermore, a suppression of the transitions from $^4I_{9/2}$ to $^4I_{15/2}$ (γ_{41}) and from $^4I_{11/2}$ to $^4I_{13/2}$ (γ_{32}) slightly increases the UCQY. If γ_{41} is decreased, a higher population of the $^4I_{9/2}$-state is achieved. As the $^4I_{11/2}$ - state is mainly populated by MPR from this level, this leads to a higher population of this level and subsequently to an increased UCQY for the emission from this level. An enhancement of γ_{32} leads to a de-excitation of the $^4I_{11/2}$-state through an intermediate transition, thus, a suppression of this emission also increases the population of the $^4I_{11/2}$-state. Furthermore, an increase of the transition rate from the $^4I_{11/2}$ to the $^4I_{15/2}$ (γ_{31}) can increase the UCQY. Thus, the aim of a photonic structure is to increase the local irradiance, to decrease the transition probability for the transition from the $^4I_{13/2}$ to the $^4I_{15/2}$ ground state, corresponding to a direct re-emission of photons at a wavelength of 1523 nm, and increase the transition probability for the transition from the $^4I_{11/2}$ to the $^4I_{15/2}$ ground state leading to the emission of a photon at a wavelength of 980 nm.

Two different approaches for one-dimensional photonic structures that could be beneficial for upconversion processes were investigated: a cavity structure, where the irradiance is increased by a rear-reflector and the emission is influenced by a microcavity, and an interdigitated Bragg-structure, where both the irradiance and the emission are influenced si-

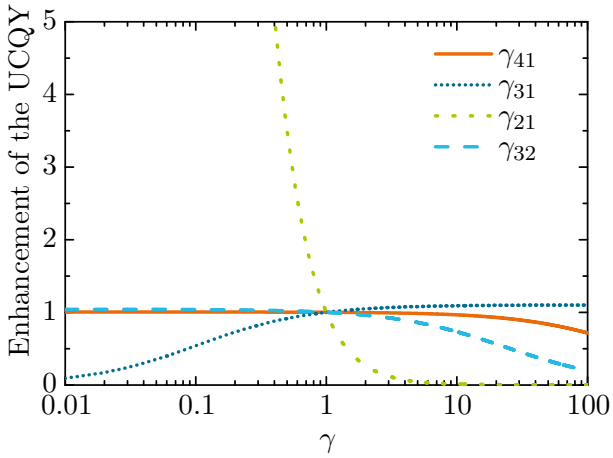

Figure 6.13: Influence of a variation of the transition rates on the UCQY for the most dominant transition. γ describes the variation factor for the transition rate. The orange solid line γ_{41}corresponds to the emission from the $^4I_{9/2}$-level to the $^4I_{15/2}$ ground state, an enhancement of this transition rate decreases the UCQY from the $^4I_{11/2}$-level as this level is typically populated by multi-phonon relaxation (MPR) from the $^4I_{9/2}$-level. The dark blue dotted line shows γ_{31}, which corresponds to the dominant upconversion emission from the $^4I_{11/2}$-level, an enhancement of this transition rate is beneficial. The green coarsely dotted line depicts γ_{21}, which corresponds to the emission from the first excited state ($^4I_{13/2}$). If this emission is suppressed, the UCQY can be drastically improved. The last line shown, the light blue dashed line denotes γ_{32}, thus, variations of the transition between the $^4I_{11/2}$-level to the $^4I_{13/2}$-level. This transition leads to a depopulation of $^4I_{11/2}$-level by an intermediate transition and is, therefore, detrimental.

multaneously by the layer thicknesses.

6.4.1 Cavity Structure

The results presented in this subsection were achieved as part of the diploma thesis of Sebastian Wolf [130], which I supervised. Within this work, the variations of the LDOS were determined using the S-Matrix approach. Using this approach, a propagation of energy within the x-y-plane is not possible. This does, therefore, not reproduce the exact variations in the LDOS as in a real system consisting of layers, there is still some emitted light that is guided to the edges. However, this simulation approach is much faster than the corresponding FDTD-simulations and shows the same trends (as shown in Figure 6.7), thus, it can be taken as an indicator for the quality of a certain structure.

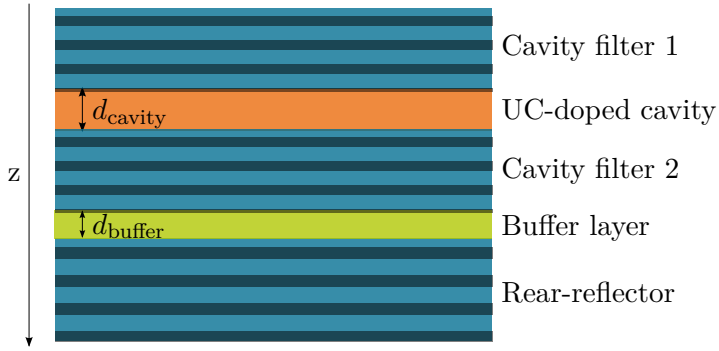

Figure 6.14: Sketch of the investigated cavity structure. The cavity is built by the two cavity filters which reflect photons in the emission wavelength of the upconverter. The upconverter layer (shown in orange) is embedded between these two filter structures. Below the structure, a rear-reflector is applied, separated by a buffer layer (shown in green) from the bottom cavity filter.

As a first system to influence upconversion processes, a cavity system with a rear-reflector was developed. This system aims for separating the effect on the absorption, basically the irradiance enhancement, from the effects on the emission. The local irradiance is enhanced by a rear-reflector for photons that can be absorbed by the upconverter material (photons at a wavelength of around 1523 nm). This filter is denoted with rear-reflector in Figure 6.14. To influence the emission as well, the upconverter layer is embedded into a cavity built by two filter structures (denoted with cavity filters in Figure 6.14), which show a high reflectance at the emission wavelength (around 980 nm) and additionally a high transmittance at the absorption wavelength of 1523 nm. This ensures that basically all photons in the absorption range of the upconverter reach the upconverter layer. The filter structures were optimized using the evolutionary algorithm described in Section 4.1.

Thus, two parameters were left for an optimization: the thickness of the cavity layer d_{cavity} and the thickness of the buffer layer d_{buffer} (as shown in Figure 6.14). The thickness of the buffer layer d_{buffer} mainly shifts the standing wave pattern resulting from the interference of the incident and the reflected wave. The cutout of the interference pattern is determined by the thickness of the cavity layer d_{cavity}. The dependence of the mean irradiance enhancement $\overline{\gamma_{\mathrm{E}}}$ on these two parameters is shown in Figure 6.15 for d_{buffer} ranging from 0 to 900 nm and d_{cavity} ranging from 200 to 1000 nm determined by S-Matrix simulations. The highest maximum for the irradiance enhancement resulting from the interference is found at a cavity layer thickness of $d_{\mathrm{cavity}} = 200\,\mathrm{nm}$, however, as the absorption of the upconverter material is rather small, the maximum around a cavity layer thickness of around 700 nm and a buffer layer thickness of 400 nm seems to be more promising. For the very thin cavity layer of around 200 nm the cut-out of the wave pattern within the cavity consists of either a single

maximum (as shown on the left in Figure 6.16) or a single minimum, resulting in very large or very small factors $\overline{\gamma_E}$. For larger cavity layer thicknesses of around 780 nm, the wave pattern consists of two maxima and a minimum in between. This is shown for cavity layer thickness of 780 nm on the right hand side of Figure 6.16.

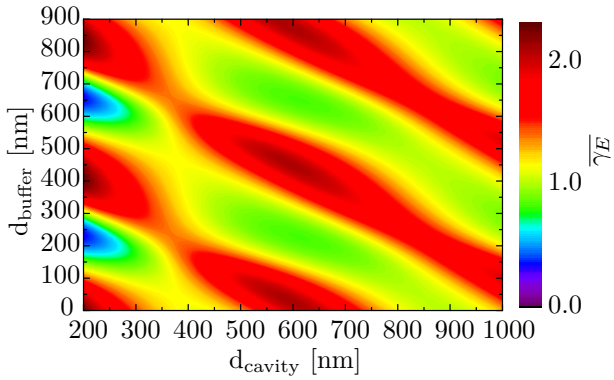

Figure 6.15: Mean irradiance enhancement plotted against the buffer layer d_{buffer} and cavity layer d_{cavity} thicknesses.

In the next step, the variation factors for the transition rates and their dependence on the cavity layer thickness were determined. First, the variation factor for the upconversion emission from the ${}^4I_{11/2}$ to the ${}^4I_{15/2}$ ground state was investigated over a rather broad range of d_{cavity} from 200 nm to 800 nm. It shows that the transition rates for this upconversion emission are reduced over the whole cavity layer for the thin cavity layers of 200 nm and 400 nm. For $d_{\text{cavity}} = 600$ nm one maximum builds up that slightly exceeds unity but in average, the transition rate is still reduced. Only for the largest value of $d_{\text{cavity}} = 800$ nm the transition rate is enhanced in average and shows two pronounced maxima. Therefore, the region around this cavity layer thickness was further investigated as

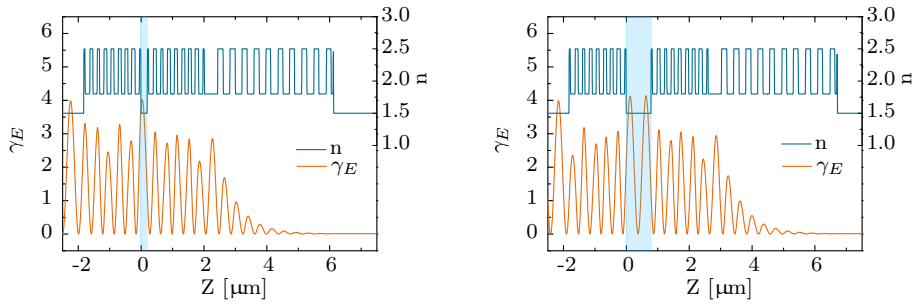

(a) 200 nm Cavity thickness (b) 780 nm Cavity thickness

Figure 6.16: Irradiance enhancement over the cavity for two different cavity layer thicknesses. The cavity is highlighted in light blue. On the left, a very thin cavity layer with a thickness of 200 nm is shown, where very high mean irradiance enhancement factors can be achieved as only one maximum is present within the cavity. Going to the thickness of 780 nm on the right, the mean irradiance enhancement is lower, as also a minimum is present within the cavity.

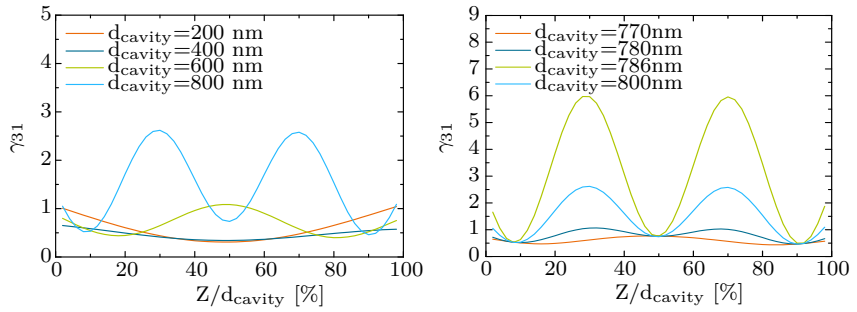

(a) Coarse Variation (b) Fine Variation

Figure 6.17: Variation of the transition rate γ_{31} over the cavity layer d_{cav} thickness for different cavity layer thicknesses in a coarse (left) and fine (right) variation.

shown on the right hand side of Figure 6.17. It shows that the transition rates vary dramatically with the thickness as for 770 nm only one, small maximum is achieved, from 780 nm on, two maxima build up which rapidly increase up to a thickness of 786 nm to maximum values of 6. For thicker layers, the effect reduces again, but slightly slower, for a thickness of 800 nm, still a maximum enhancement of 2.5 is achieved. These factors are rather independent of the buffer layer thickness, which can be explained as the dipole emitting at this frequency is surrounded by two filters which are highly reflective at the emission wavelength and is, therefore, not influenced by the structure outside.

Hence, for a cavity layer thickness of around 785 nm, the irradiance over the cavity layer as well as the transition rate for the upconversion emission is enhanced, indicating a very promising structure.

In the next step, the variation for the transition from the $^4I_{13/2}$-level to the ground state and, therefore, the reverse process of the excitation and its dependence on d_{buffer} is investigated as shown in Figure 6.18. It was found that this transition rate is mainly influenced by the thickness of the buffer layer as the cavity filters show a very low reflectance at this wavelength. For the current configuration, this transition rate is mainly reduced according to the S-Matrix results. This is beneficial for the upconversion process, as it means that the direct de-excitation of the first excited level is reduced leading to a higher population of this level and with this, a higher upconversion signal.

As discussed above, the absolute values for the transition rates obtained with the S-Matrix approach are to be taken with care, so they are only used to determine a suitable structure. This structure was found for a cavity layer thickness d_{cavity} of 785 nm and a buffer layer thickness d_{buffer} of 400 nm, where the irradiance enhancement as well as the transition probability for the transition from the $^4I_{11/2}$-state to the ground state are

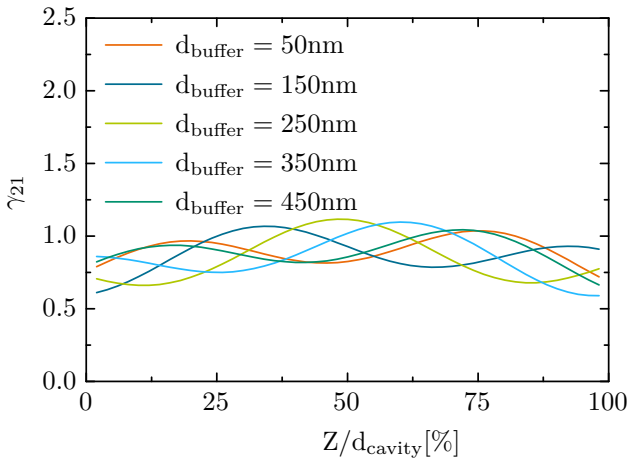

Figure 6.18: Variation of the transition rate γ_{21} versus the buffer layer thickness d_{buffer}.

varied in a beneficial way. The buffer layer thickness d_{buffer} was set to 400 nm to achieve a high irradiance enhancement without a detrimental effect on the transition rate from the first excited state.

For this optimized configuration, the variations of the transition probabilities were calculated again using a two-dimensional FDTD-simulation setup with absorbing boundaries in all directions to obtain the influence of the structure on the UCQY as shown in Figure 6.19.

Figure 6.19 shows the enhancement factors for the absorption, the luminescence and the UCQY for the optimized cavity structure with a cavity layer thickness of 785 nm and a buffer layer thickness of 400 nm over the position along the z-direction within the cavity. Averaged over the cavity, the absorption is enhanced by a factor of $\overline{\gamma_{Abs}} = 1.6$, the luminescence by a factor of $\overline{\gamma_{Lum}} = 1.9$ and the UCQY by a factor of $\overline{\gamma_{UCQY}} = 1.2$. These values denote a considerable enhancement in the upconversion signal, which is partially due to a higher absorption caused by the standing

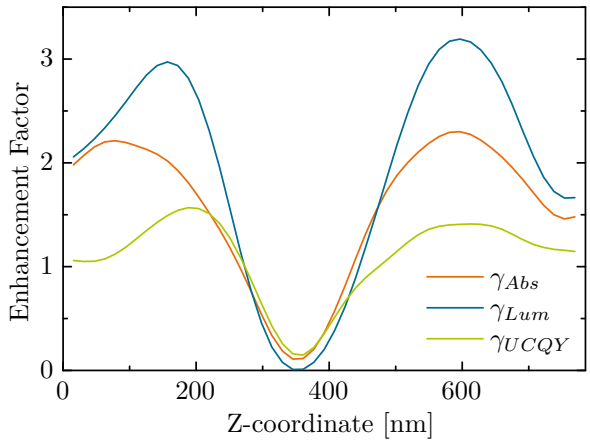

Figure 6.19: Enhancement of the absorption, the luminescence and the UCQY for an optimized cavity structure with a cavity layer thickness of 785 nm and a buffer layer thickness of 400 nm. The incident irradiance was set to 4337W/m^2.

wave pattern originating from the rear-reflector and also shows a substantial influence of the varied transition rates due to the cavity.

6.4.2 Interdigitated Bragg-Structure

The main drawback of the cavity structure described in the previous subsection is the low absorption due to the fact that the upconverter layer has to be very thin to benefit from the photonic effects of the structure. Furthermore, as the absorption of the material is rather low, it is difficult to quantify the effects on the UCQY in actual measurements. One approach to overcome these limitations is a multilayer structure, where the upconverter material is not only present in one layer but in every second layer of a suitable structure. Here, we investigated a structure consisting of four alternating layers to influence the absorption as well as the emission of the

upconverter material. To achieve this, there are three main effects that can be influenced by a photonic structure: the local irradiance, the emission probability from the first excited level, which is a detrimental process as it leads to a direct re-emission from the first excited state, and the emission probability from the second excited state, which should be enhanced as this corresponds to the most important upconversion emission.

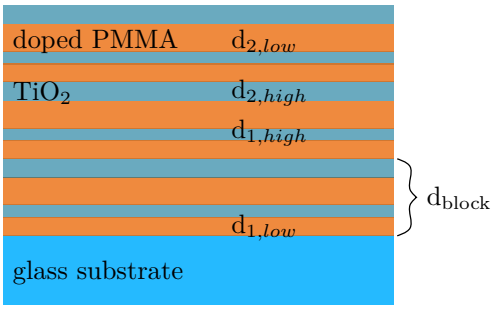

Figure 6.20: Sketch of an interdigitated Bragg-structure consisting of three blocks: The orange layers denote the doped PMMA-layers with upconverter inside, whereas the blue layers are TiO_2-layers, these layers are required as high-index layers.

As over 95 % of the photons are directly re-emitted, the suppression of this emission process is one of the most important levers. One possibility to do this is to place a photonic band gap around the emission frequency. However, as this corresponds to the absorption frequency of 1523 nm, a band gap in this range would simply lead to no absorption. This problem can be overcome under the assumption that the light to be upconverted is incident under a very small angular range whereas the emission takes place over the full solid angle. Thus, it should be possible to build a structure, where the rising edge of the reflectance peak, which corresponds to a band gap within the material can be tuned to lie very close to the emission wavelength. Thus, for the light incident under normal angle, the DOS

is actually enhanced due to the proximity of the band gap. For larger angles, however, the reflectance peak and with it the band gap shifts to lower wavelength, thus, for larger angles, the emission of photons at the emission wavelength is suppressed. If we additionally want to influence the upconversion emission, one possibility would be to add a second peak which has its falling edge close to the emission wavelength.

One possibility to obtain such a reflectance characteristics would be an interdigitated Bragg-structure, thus, a combination of two Bragg filters, which results in a system with a repeat unit consisting of four layers. This configuration limits the number of free parameters to three, the total thickness d_{block} of the repeat unit, the thickness ratio r between the two Bragg stacks, and the number of blocks N_{blocks}. The thicknesses of the four layers are then given by:

$$d_{1,high} = \frac{n_{low}}{n_{low} + n_{high}} \cdot r \tag{6.3}$$

$$d_{1,low} = \frac{n_{high}}{n_{low} + n_{high}} \cdot r \tag{6.4}$$

$$d_{2,high} = \frac{n_{low}}{n_{low} + n_{high}} \cdot (1 - r) \tag{6.5}$$

$$d_{2,low} = \frac{n_{high}}{n_{low} + n_{high}} \cdot (1 - r). \tag{6.6}$$

The position of the two reflectance peaks is determined by the total thickness d_{block} of the system. The separation into two different blocks opens up a second band gap as shown in Figure 6.21. In a simple Bragg filter as shown in Figure 6.9 band gaps only build up between the first and the second and between the third and the forth band and so on. For the interdigitated structure, additionally, band splitting between the second and the third band occurs. The ratio r between the two blocks determines the relative height of the peaks (the band gaps) and the number of blocks

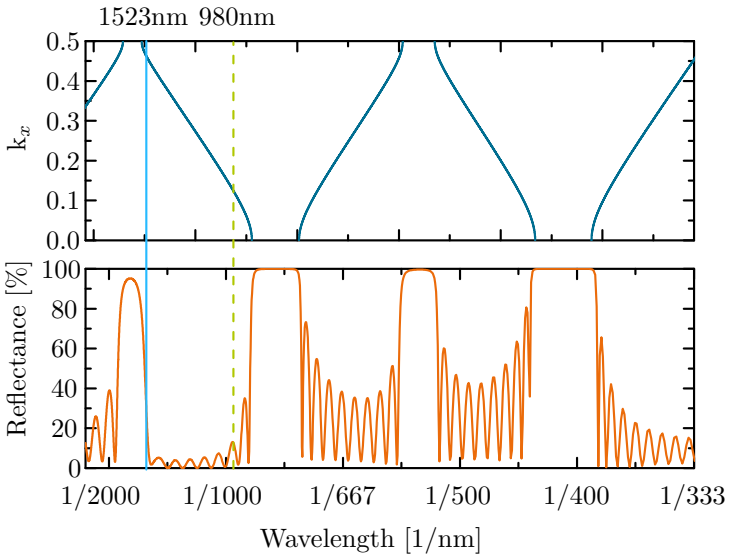

Figure 6.21: Reflectance characteristics of an interdigitated Bragg- structure compared to its photonic band structure for a system with a thickness d_{block} of 460 nm, a ratio r of 0.3 between the Bragg-structures, consisting of 10 blocks. The solid light blue line denotes the absorption wavelength of 1523 nm which is found close to the band edge. The dashed green line depicts the emission wavelength of 980 nm. This wavelength is also in the proximity of a band gap.

N_{blocks} determines the absolute height of the peaks. The order of the different layers influences the side-lobes in the reflectance characteristics.

The mean irradiance enhancement $\overline{\gamma_{\text{E}}}$ depends on the structure parameters and is inversely correlated to the reflectance at the absorption wavelength. From an optimization of this mean irradiance enhancement, a suitable structure for the embedding of upconverter material was determined. It was found that the system with a thickness d_{block} of 490 nm

and a ratio r of 0.1 between the Bragg-structures consisting of 10 blocks shows very good values for the mean irradiance enhancement $\overline{\gamma_{\mathrm{E}}}$. The dependence of γ_{E} on the position over the structure is shown in Figure 6.22. The refractive index of the stack is also shown here to emphasize that the highest irradiance enhancements can be found for this specific structure in the low-index layers. As these layers would contain the up-converter material, these characteristics would be very beneficial for the upconversion process.

For this structure, showing the highest values for the irradiance enhancement subsequently emission simulations were carried out using the S-Matrix approach. As described above, a dipole implemented in this method is not able to emit in the x-y-plane. Thus, the results are merely an indication for the suitability of the structure.

Figure 6.22 shows that the two most important transition rates, the direct re-emission from the first excited state leading to an emission of photons at a wavelength of 1523 nm and the most important upconversion emission at a wavelength of 980 nm are both influenced by the structure. The influence is found to be more dominant on the 1523 nm emission, this is to be expected as for the small ratio $r = 0.1$ between the Bragg stacks, the band gap around 1600 nm is much more pronounced than the one around 900 nm. Furthermore, as for the S-Matrix approach, the emission in the x-y-plane is not possible, the effect of the band gap shifting over the emission wavelength is not taken account for correctly. The effect on the upconversion emission at 980 nm is rather small, thus, the band edge seems to be too far away to considerably influence the emission at this wavelength.

Still, the structure seems to be useful to influence upconversion in a beneficial way, due to the comparably large irradiance enhancement for the incident light at a wavelength of 1523 nm and due to the fact that

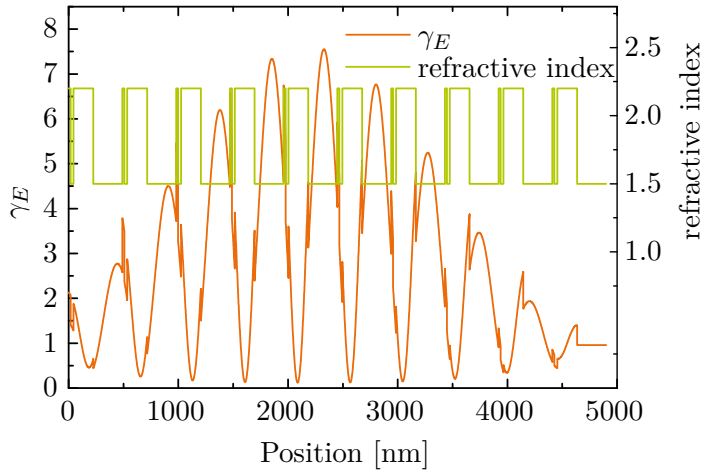

(a) Irradiance Enhancement

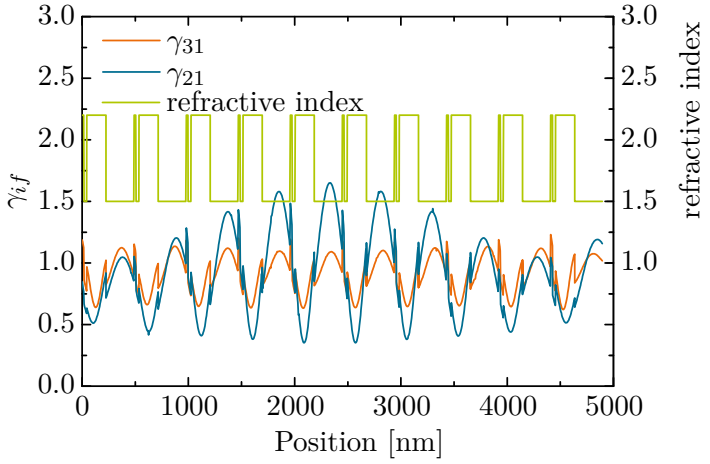

(b) Enhancement of the emission coefficients

Figure 6.22: Irradiance enhancement and enhancement of the emisison coefficients over an interdigitated Bragg-structure with a thickness d_{block} of 490 nm, a ratio r of 0.1 between the Bragg-structures and for 10 blocks.

the suppression of the direct re-emission for larger angles might occur, even if it is not visible in the simulations. However, as the effect on the upconversion emission wavelength is very small, the structure could be simplified to only one Bragg stack influencing the absorption.

6.5 Upconversion in a Grating Structure

As the flexibility of one-dimensional structures is rather limited, more complex structures, such as linear grating structures could be more promising. However, no three-dimensional structures, including crossed gratings could be investigated in this work, due to the high computational effort.

Instead, in this work, a linear grating structure within the upconverter material as a surface grating. Below the upconverter layer, a metallic mirror was placed to ensure that resonances can build up within the upconverter layer. The structure is sketched in Figure 6.23.

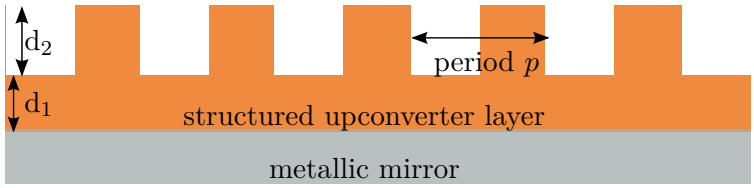

Figure 6.23: Sketch of the investigated upconverter grating structure against air with a structure period p, a thickness of the homogeneous layer d_1 and the thickness of the grating layer d_2.

For this structure, there are three parameters that can be tuned to increase the influence on upconversion processes. These parameters are the period p of the structure, the thickness of the homogeneous layer below the grating d_1 and the thickness of the grating part d_2. In principle, the fill factor of the grating would be an additional parameter that could be tuned,

but as it is rather complicated to tune that in a precise way experimentally, the fill factor was kept constant at 50 % for all simulations.

As the irradiance enhancement within the structure can be determined much faster than the LDOS as described in Chapter 4, a first optimization of the structure was carried out to maximize the irradiance enhancement within the grating. In order to reach this, the three parameters were varied from $p = 0.1$ µm to $p = 10$ µm, $d_1 = 0$ to $d_1 = 1$ µm and $d_2 = 100$ nm to $d_2 = 2$ µm and the irradiance enhancement within the grating was determined for each configuration. The structure period p was found to have the largest influence. Figure 6.24 shows the influence of the grating period on the upconversion quantum yield if the variations of the LDOS are neglected. Over the broad investigated range of 100 nm to 10 µm several peaks evolve which can be attributed to resonances in the grating part of the structure, resonances in the homogeneous medium or resonances in a artificial effective medium. Using these three simplifications, all major peaks in the plot can be explained. Due to the slightly larger width of the peak, a structure period of $p = 1.25$ µm was chosen for further investigations.

In addition to the structure period, the other two parameters were varied and the dependence of the mean irradiance enhancement on these two parameters was determined as shown in Figure 6.25. Here, a rather extended maximum is found for a thickness d_1 of 400 nm to 600 nm, which is rather independent of d_2. This maximum can be explained by a resonance within the layer below the grating for these structure parameters. A thickness d_1 of around 500 nm corresponds to a layer thickness of $\lambda/2$ in the medium with a refractive index of $n = 1.5$. The position of all other maxima depend on both thicknesses, thus, in these cases, the complete structure satisfies a resonance condition for the incident wavelength of 1523 nm.

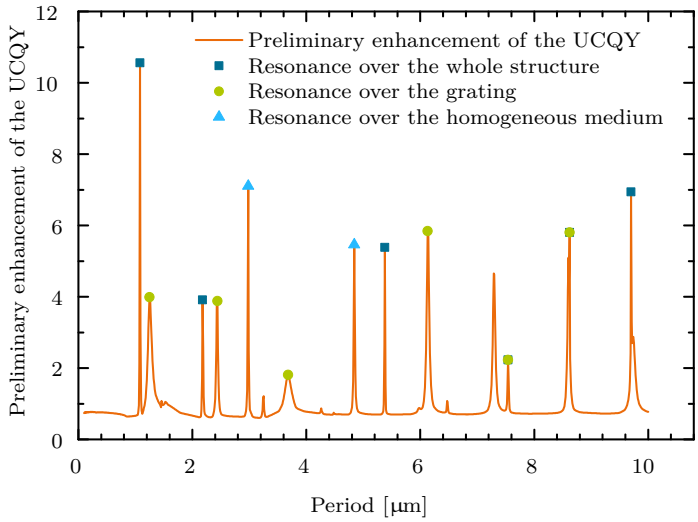

Figure 6.24: Variation of the preliminary enhancement of the UCQY over the period of a grating structure against air. This preliminary enhancement factor was determined from the irradiance distribution within the grating for an initial irradiance of $200\,\mathrm{W/m^2}$. The squares, dots and triangles denote resonances in the whole structure, the grating region or the homogeneous region, respectively.

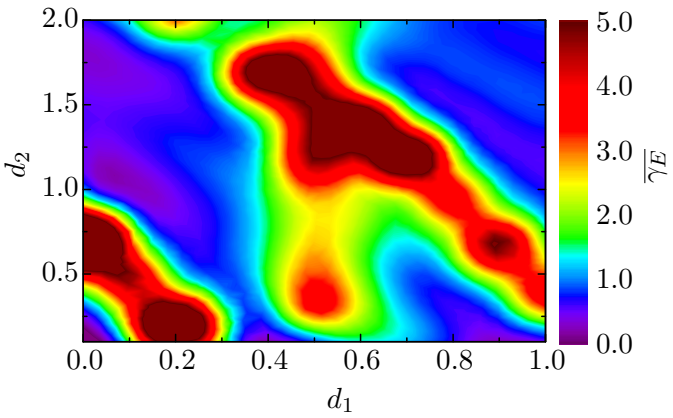

Figure 6.25: Plot of the mean irradiance enhancement factor in dependence of the thicknesses d_1 and d_2 of a grating structure against air shown for a grating period p of 1.25 µm.

From these optimizations of the irradiance enhancement, a suitable structure was found with layer thicknesses of $d_1 = 500 - 600$ nm and $d_2 = 400$ nm, values where the layer thicknesses are reasonably thick to obtain some absorption and with an aspect ratio that can still be produced. These parameters were taken as input parameters for another variation of the structure period as this parameter was found to show the largest influence on the structure performance. For d_1 the largest thickness still in the range of the peak of 600 nm was taken to increase the amount of material. In this next optimization step, the LDOS-enhancement was determined over a series of grating structures with different structure periods in a rather coarse mesh of $50 - 100$ nm. Furthermore, in these variations only the grating part of the structure was investigated, neglecting the homogeneous bottom layer. From these variations of the LDOS together with the irradiance enhancement, the actual influence of the structure on the upconversion processes could be determined from the coupling to the rate-equation model.

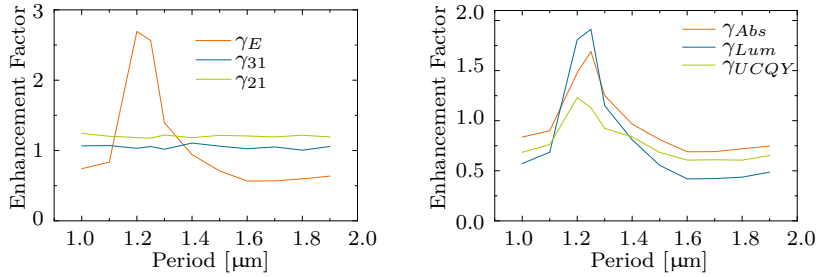

(a) Mean Input Parameters (b) Mean Enhancement Factors

Figure 6.26: Comparison of the dependence of the input parameters and the enhancement factors on the grating period.

Figure 6.26 shows that the mean irradiance enhancement has its maximum at a period of around p= 1.2 µm at a value of 2.7. The peak is also rather broad, which offers some flexibility for process variations. The mean enhancement factors for the transition rates γ_{if} do not show a strong dependence on the structure period. However, the direct re-emission from the ${}^4I_{13/2}$-state (γ_{21}) is in all cases stronger enhanced than the upconversion emission from the ${}^4I_{11/2}$-level (γ_{31}). This has a detrimental effect on the UCQY. The irradiance enhancement factors as well as the enhancement factors for the various transition rates were considered in the rate-equation model for the upconverter material for an incident irradiance of 4337 W/m^2. This high value for the incident irradiance is chosen as this was the irradiance used in the experiments. The results for the absorption, the upconversion luminescence and the UCQY are shown on the right hand side of Figure 6.26. It shows that the the irradiance enhancement mainly follows the absorption enhancement. For the optimized structure with a period of 1.25 µm, the absorption is increased by a factor of 1.7, the luminescence increases for the same structure period by a factor of 1.9. Thus, this luminescence enhancement does not only rely

on an absorption enhancement, the UCQY is also increased by a factor of 1.1. These effects are naturally higher for a lower initial irradiance.

Due to the rather low effect of the structure period on the transition rates and the more beneficial irradiance distribution, a structure period of $p = 1.25\ \mu\text{m}$ was chosen for a more detailed calculation. The other structure parameters d_1 and d_2 were kept at values of 600 nm and 400 nm, respectively. For this optimized structure, the LDOS was determined on a fine mesh to obtain a detailed picture of the transition variations, and from these, a local information about the changes in the absorption, the luminescence and the UCQY.

Figure 6.27 shows the variation of the irradiance enhancement γ_{E}, γ_{31} and γ_{21}, the most important factors that influence the upconversion process over the whole grating structure. The top right part of the figures corresponds to the air ridges where no upconverter is present. The irradiance increases by a mean factor of 2.09 over the grating structure and average values $\overline{\gamma_{31}} = 0.95$ and $\overline{\gamma_{21}} = 0.90$ were found. Thus, upconversion within this structure benefits from the local irradiance enhancement and the suppression of the direct re-emission from the first excited state.

Figure 6.28 shows the results from the rate-equation model for the input parameters shown in Figure 6.27 for an initial irradiance of $4337\ \text{W/m}^2$.

It shows that the absorption is enhanced according to the irradiance enhancement, with a mean enhancement of $\overline{\gamma_{Abs}} = 1.96$. The luminescence within the structure is enhanced by a mean value of $\overline{\gamma_{Lum}} = 3.0$. This results in a mean enhancement of the UCQY of $\overline{\gamma_{UCQY}} = 1.53$. In this case, the luminescence increases not only due to the irradiance enhancement, but, as described above also benefits from the suppression of the direct re-emission from the first excited state.

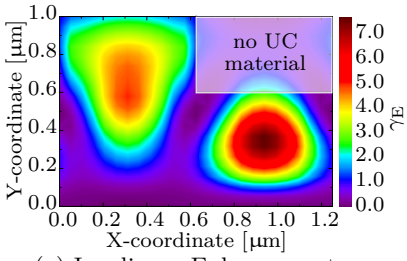

(a) Irradiance Enhancement γ_E

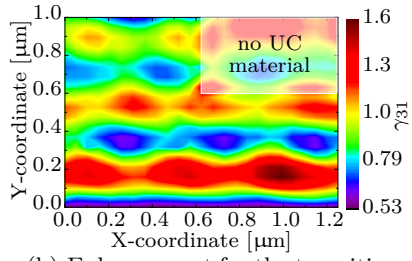

(b) Enhancement for the transition rate from the ${}^4I_{11/2}$ to the ${}^4I_{15/2}$-state γ_{31}

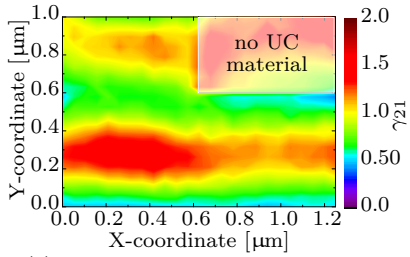

(c) Enhancement for the transition rate from the ${}^4I_{13/2}$ to the ${}^4I_{15/2}$-state γ_{21}

Figure 6.27: On the top left, the variation of the irradiance enhancement γ_E is plotted over the structure, the enhancement γ_{31} for the upconversion emission is shown on the top right and the enhancement γ_{21} for the emission from the first excited state is shown on the bottom.

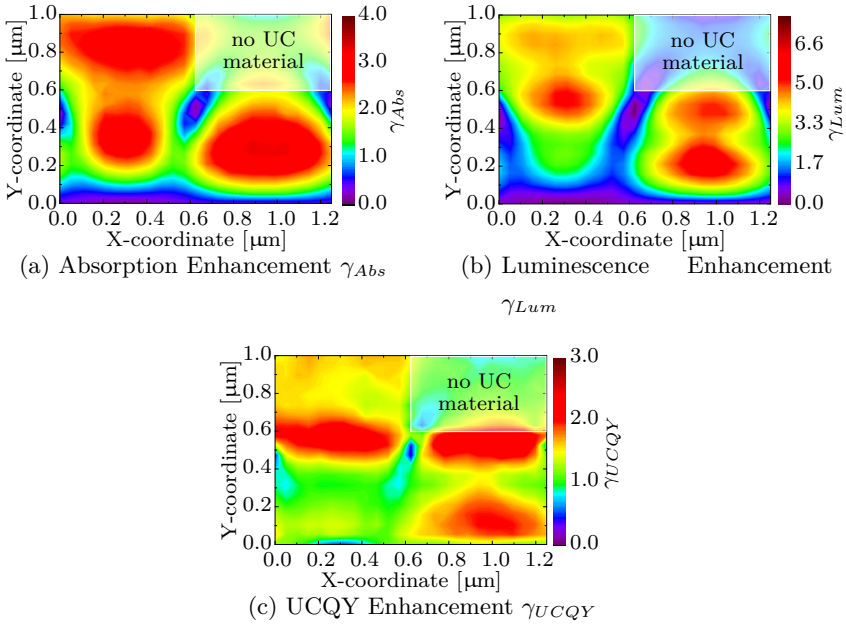

(a) Absorption Enhancement γ_{Abs} (b) Luminescence Enhancement γ_{Lum}

(c) UCQY Enhancement γ_{UCQY}

Figure 6.28: Influence of the grating on the absorption, the upconversion luminescence and the quantum yield for an initial irradiance of 4337W/m^2.

6.6 Upconversion in Grating Waveguide Structures

To further improve the effect of the photonic structure on upconversion processes, a more complex waveguide-structure was investigated, which consists of a rear-reflector, a homogeneous layer with a thickness d_1 and a linear grating with a thickness d_2, like the grating structure described in the previous section. However, in this case, the grating is not a surface grating but is filled either with a material with higher refractive index as described in the first subsection or is built by the embedding of air holes as described in the second subsection. This grating layer is covered

again with a layer of homogeneous medium with a thickness d_3. Similar structures were investigated in [175, 176]. The structure is sketched in Figure 6.29.

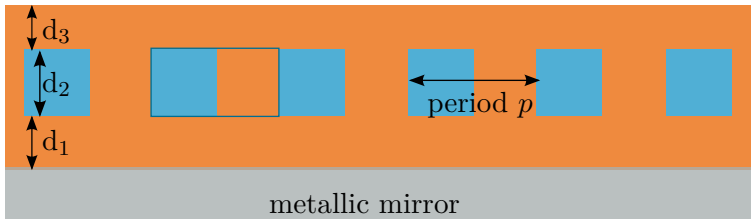

Figure 6.29: Sketch of the investigated upconverter grating waveguide structure where the blue regions can be either filled with a material of refractive index of $n_{high} = 2$ or consist of air inclusions.

6.6.1 Grating Waveguide Structure with Embedded High-Refractive Index Material

As for the grating structure, the irradiance distribution under illumination with the absorption wavelength of 1523 nm within the structure was investigated to decide whether the structure might be suitable for upconversion. This was carried out for all structure parameters denoted in Figure 6.29. As for the grating structure, the fill factor was kept constant at 50 %. The irradiance distributions can be taken into account in the rate-equation model, neglecting the influence of the variations in the LDOS. The results shown in this subsection were published in [17].

Figure 6.30 shows the optimization of the structure period p. The structure period p was varied over a very broad range from 0.1 µm to 10 µm. The orange squares in the plot denote integer multiples of a period of 0.87 µm. For these periods, a high incoupling efficiency of the grating

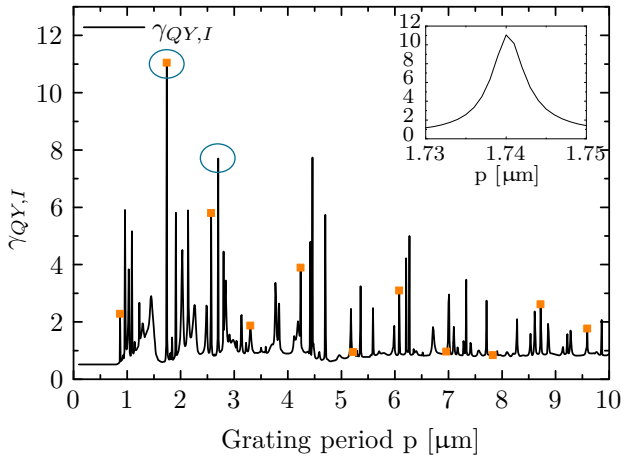

Figure 6.30: Enhancement of the upconversion quantum yield due to the irradiance enhancement within the structure. A first, dominant maximum is obtained for a grating period of 1.74 µm indicating a preliminary enhancement in the UCQY of a factor of 11. The inset shows the peak shape of this maximum. The orange squares denote integer multiples of 0.87 µm. This period corresponds to a resonance in the grating part of the structure. The circled structures correspond to the structure periods of 1.74 µm and 2.7 µm, which were investigated further.

for light with a wavelength of 1523 nm into the waveguide is expected, as the waveguide has a refractive index of 1.75 if it is considered as an effective medium. Due to the complexity of the investigated structure, more peaks evolve due to resonances in the different layers. These various resonances can interfere constructively or destructively resulting in the very complex pattern shown in Figure 6.30. A first maximum can be found for a structure period of 1.74 µm. Additionally, the peak that is found for a

structure period of 2.7 µm was investigated further. These two structure periods were chosen for further investigation under the assumption that their influence on the LDOS is expected to be very different: This assumption was based on the investigation of the one-dimensional band structure within the grating region. For this, the band structure was calculated for an infinitely extended structure with alternating refractive indices of $n_{low} = 1.5$ and $n_{high} = 2.0$, each with a thickness of half the structure period. The obtained band structures are shown in Figure 6.31.

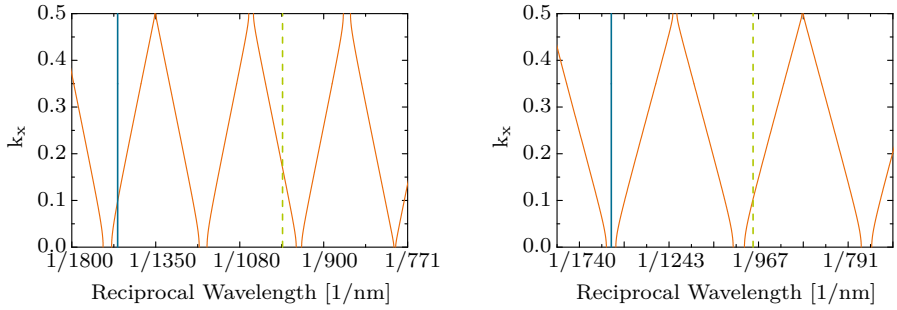

(a) Structure period $p = 2.7$ µm (b) Structure period $p = 1.74$ µm

Figure 6.31: Band structure for the grating part of the grating waveguide structure for two different structure periods of 2.7 µm and 1.74 µm. The blue line depicts the absorption wavelength of 1523 nm and the green dashed line the emission wavelength of 980 nm.

As shown in Figure 6.31, the absorption wavelength of 1523 nm (blue solid line) lies close to a one-dimensional band gap over the grating part in the structure with a period of 2.7 µm whereas it lies within a band gap for the structure with a period of 1.74 µm. For the absorption wavelength of 1523 nm this indicates an enhancement (a suppression) for the structure period of 2.7 µm (1.74 µm). From these considerations, it is expected that

the structure with a period of 1.74 µm will perform better. The emission wavelength of 980 nm (green dashed line) on the other hand lies close to a band edge for the structure with $p = 1.74$ µm and further away from the band gap for the structure with $p = 2.7$ µm. This can be taken as an indication for an enhancement of the DOS at a wavelength of 980 nm for the first structure whereas it is hardly affected in the second case.

For both structure periods with preliminary optimized parameters, a complete calculation of the LDOS was carried out to determine the effects on the upconversion processes. This resulted in a mean UCQY of only 26% of the initial value for the structure with p= 2.7 µm, which corresponds to a dramatic decrease in the upconversion performance despite the irradiance enhancement within the structure. This decrease could be attributed to an increase of the LDOS at the absorption wavelength of 1523 nm, which leads to an increased direct re-emission of photons at this wavelength and with this a decreased population of the first excited state resulting in less upconversion. The more promising results could be obtained for a structure with a period of 1.74 µm as shown in the following.

Figure 6.32 shows the spatial distribution of the irradiance enhancement over the grating region illuminated by the combined *s*- and *p*-polarized source for the structure presented in Fig. 6.29 for a structure with a period p= 1.74 µm and thicknesses of $d_1 = 390$ nm, $d_2 = 1.16$ µm and $d_3 = 1.4$ µm.

As shown in Figure 6.32, the irradiance is increased considerably within the structure. This effect, however, concentrates in the high-index region (shown on the left) of the grating where a maximum of $\gamma_{\mathrm{E}} = 11.5$ can be found compared to a maximum of $\gamma_{\mathrm{E}} = 2.9$ in the low-index region (shown on the right). Thus, it would be advantageous to have a high-refractive index upconverter. Additionally to the irradiance enhancement the two most important variation factors for the transition rates from the $^4I_{13/2}$-level to the $^4I_{15/2}$ ground state (γ_{21}) and from the $^4I_{11/2}$-level to the

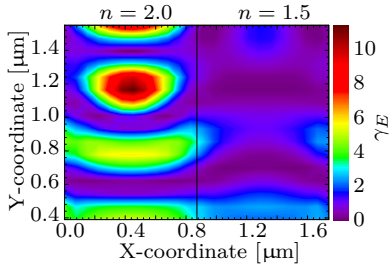

(a) Irradiance Enhancement

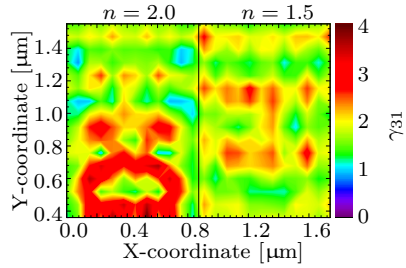

(b) Enhancement of the transition probability γ_{31}

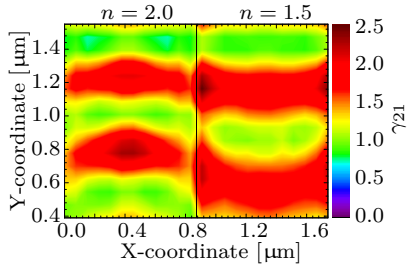

(c) Enhancement of the transition probability γ_{21}

Figure 6.32: Irradiance enhancement and enhancement of the two most important transition probabilities for the optimized grating waveguide structure shown over the grating part of the structure as depicted in Figure 6.29.

ground state (γ_{31}) are shown. For γ_{31}, these values vary from 0.9 to 4.1 in the high-index region, and from 1.1 to 2.9 in the low-index region. This factor is only slightly decreased over small spots, thus, overall the emission is considerably enhanced over the whole structure for this transition. For the direct re-emission (γ_{21}), values ranging from 0.9 to 2.5 are found in the high-index region and from 0.7 to 2.3 in the low-index region. These variation factors were not only determined for these two transitions but for

all possible transitions within Er^{3+} considered by the rate-equation model. These results were subsequently taken account for in the rate-equation model as described in Section 4.6 to obtain the absorption enhancement γ_{Abs}, the luminescence enhancement γ_{Lum} and the enhancement of the UCQY γ_{UCQY}.

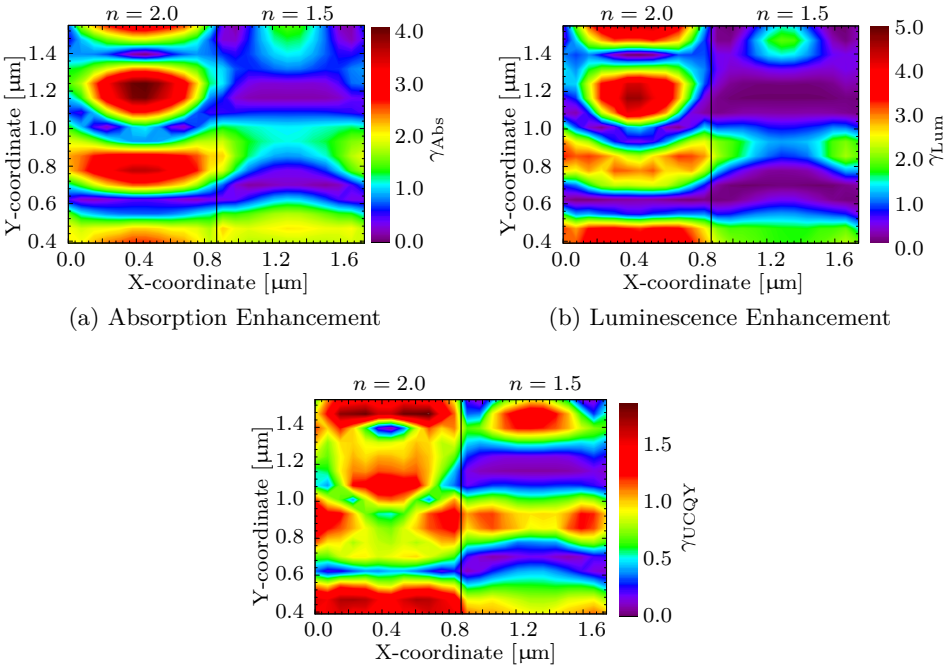

(a) Absorption Enhancement

(b) Luminescence Enhancement

(c) Enhancement of the UCQY

Figure 6.33: Enhancement of the absorption, the luminescence and the upconversion quantum yield

Figure 6.33 shows the absorption enhancement γ_{Abs} under illumination at a wavelength of 1523 nm which is increased up to a value of 4.1 in the high-index region and up to a value of 2.2 in the low-index region. The spatial distribution follows the distribution of the irradiance

shown in Figure 6.32. To quantify the effect on the upconversion processes, again the emission from the $^4I_{11/2}$-level which corresponds to the most dominant upconversion emission is considered. The luminescence- and UCQY-enhancement for this emission is also shown in Figure 6.33, which shows that the luminescence can be increased by up to a factor of 4.6 in the high-index region and by up to 2.3 in the low-index region. Averaged over the whole simulated region, the luminescence increases by a factor of 1.4. This enhancement of luminescence is mainly caused by the increased absorption. Comparing the two distributions for γ_{Abs} and γ_{Lum}, a clear correlation can be found. The UCQY, which can be determined from the luminescence and the absorption values, is enhanced by a factor of up to $\gamma_{UCQY} = 1.9$ in the high-index region and up to $\gamma_{UCQY} = 1.4$ in the low-index region. If the upconverter was evenly distributed over the whole grating regions, including the high- and the low-index regions, the UCQY is hardly affected.

Table 6.2 gives an overview over the different enhancement factors. The maximum values are given for the low and high refractive index region separately; the average was calculated for the whole structure

For all these analyses, the energy transfer processes were considered to be independent of the variations in the LDOS following the considerations in [78, 79]. If, however, a linear dependence is assumed as proposed in [80], an overall increase of the UCQY by a factor of 1.4 is achieved. This can easily be understood as energy transfer upconversion is the dominant upconversion process for β-$NaYF_4$:Er^{3+}, so any variations in energy transfer rates strongly influence the UCQY.

Table 6.2: Overview over maximum and averaged enhancement factors of the determined different quantities within the waveguide structure.

	γ_{E}	γ_{31}	γ_{Lum}	γ_{Abs}	γ_{UCQY}
$\mathrm{max}_{\mathrm{low}}$	2.9	2.9	2.3	2.2	1.4
$\mathrm{max}_{\mathrm{high}}$	11.5	4.1	4.6	4.1	1.9
average	2.0	1.9	1.4	1.4	1.0
$\mathrm{average}_{\mathrm{low}}$	1.0	1.8	0.9	1.0	0.8
$\mathrm{average}_{\mathrm{high}}$	3.0	2.0	2.0	1.8	1.1

6.6.2 Grating Waveguide Structure with Air Inclusions

As the results obtained from the previous subsection showed that the highest enhancement could be found in the high-index part of the structure, we investigated as well a structure where the high-index material is replaced by air inclusions making the upconverter the high-index region. The results shown in this subsections were published in [68]. For this, the structure parameters were scaled to account for the varied effective refractive index. The structure period p was set to 1 µm, and the layer thicknesses to $d_1 = 200\,\mathrm{nm}$, $d_2 = 1\,\mu\mathrm{m}$ and $d_3 = 100\,\mathrm{nm}$. In this case, only the region within the grating having a refractive index of $n = 1.5$ is investigated. Figure 6.34 shows the input for the rate-equation model, the irradiance enhancement γ_{E} within the structured region can be increased by a factor of up to 4.0 and in average is increased by a factor of 1.5. This increase is much lower than for the structure with embedded high-index material due to the lower quality of the waveguide, which is reduced due to the lower effective refractive index.

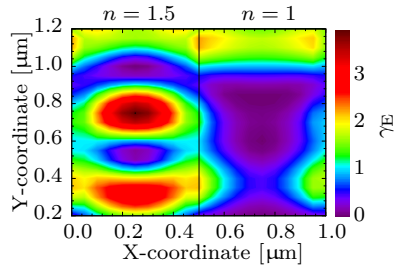

(a) Irradiance Enhancement γ_E

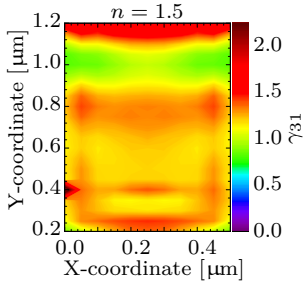

(b) Enhancement for the transition rate from the ${}^4I_{11/2}$ to the ${}^4I_{15/2}$-state γ_{31}

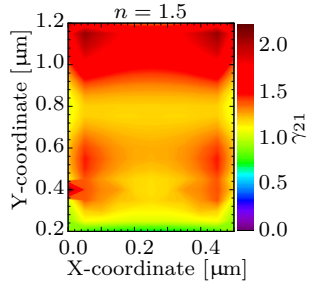

(c) Enhancement for the transition rate from the ${}^4I_{13/2}$ to the ${}^4I_{15/2}$-state γ_{21}

Figure 6.34: Most important input parameters used in the rate-equation model for a grating waveguide structure with air inclusions: The irradiance enhancement γ_E-distribution is shown on the top, on the bottom left, the enhancement factor γ_{31} is shown, which influences the upconversion emission and on the bottom right, the enhancement factor γ_{21} is shown that affects the emission from the first excited state.

The enhancement factor for the transition rate for the upconversion emission γ_{31} varies from 0.8 to 2.5 with a mean value of 1.2. It is increased at the top of the structure and stays relatively constant over the rest of the structure. The third parameter shown is again the enhancement factor for the transition rate from the first excited state to the ground state γ_{21} with a maximum of 2.2, a minimum of 0.7 and a mean value 1.3. This factor also shows the largest enhancement factors at the top of the structure.

These parameters were again taken into account in the rate-equation model for the upconverter and Figure 6.35 shows the results for the absorption enhancement γ_{Abs}, the luminescence from the ${}^4I_{11/2}$-state and the UCQY-enhancement for this transition. As for all structures, the absorption enhancement γ_{Abs} mainly follows the distribution of the irradiance enhancement γ_{E}. It shows a maximum of 2.2 and a mean value of 1.3. The luminescence enhancement γ_{Lum} has its maximum at the position of highest absorption but at the top of the structure, where γ_{Abs} is still rather high, there is almost no luminescence. This is due to the high values for γ_{21} which leads to a higher de-population of the first excited state. Over the structured region, γ_{Lum} has a maximum of 2.9 and a mean value of 1.2. The most important parameter, the enhancement of the UCQY γ_{iUCQY} is also increased at the position of highest absorption but it features an additional maximum at the bottom of the structure which is due to an enhancement of γ_{31} and a small value of γ_{21}. It shows a maximum of 1.8 and a mean value of 0.9. Thus, for this structure, the iUCQY is overall decreased by 10%, which is mainly due to the low quality of the waveguide.

If we compare the two different waveguide structures with embedded material with a refractive index of $n_{high} = 2$ and the one with air inclusions under the assumption that the refractive index of the upconverter is $n_{UC} = 1.5$, we find that the iUCQY is decreased by 20 % for the first structure, whereas it is decreased by 10 % for the second structure. Thus, if we

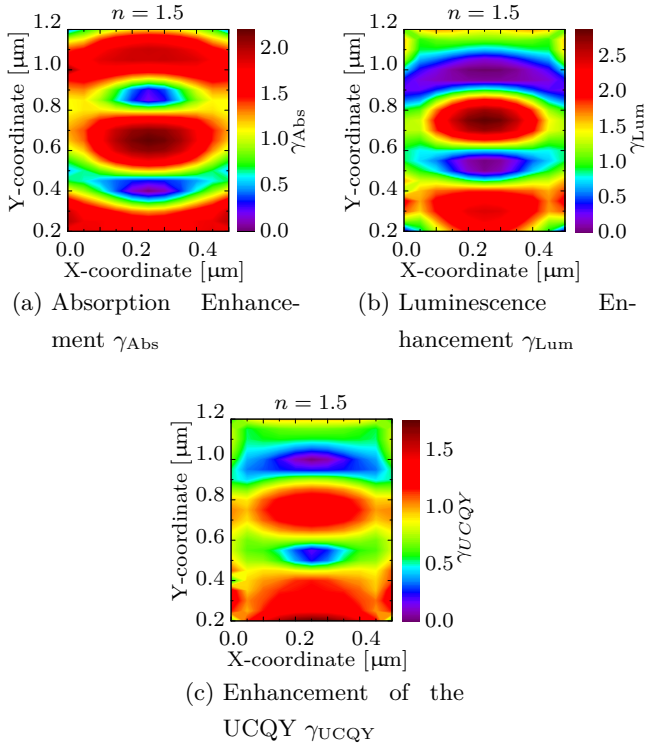

(a) Absorption Enhancement γ_{Abs}

(b) Luminescence Enhancement γ_{Lum}

(c) Enhancement of the UCQY γ_{UCQY}

Figure 6.35: Results obtained from the rate-equation model for a grating waveguide structure with air inclusions.

consider only upconverter material with a refractive index of $n_{UC} = 1.5$, neither of the structures can improve the UCQY in the investigated region. The reasons for this are that in the first structure, the irradiance is locally enhanced in the high-index region, leading to a reduction in the low index region. In the second structure, the irradiance enhancement is lower and it is not beneficial to have a buried grating structure.

7 Experimental Results

This chapter summarizes the experimental results that were achieved for the two different purposes: light guiding and directly influencing the upconversion process. In the first section, two different processes are described that were used to prepare filter structures based on amorphous silicon carbides with different refractive indices. In the second section, the results obtained for the direct incorporation of upconverter material into photonic structures is described. Here, two different structures were prepared and investigated by photoluminescence measurements: the cavity structure, where the upconverter is embedded between two filter structures with a high reflectance at the emission wavelength to enhance the emission probability. Additionally, a rear-reflector is applied to increase the local irradiance. The second structure that was investigated was the surface grating structure, where a linear grating is embossed into an upconverter layer deposited on top of a mirror. It is shown, that the luminescence can be increased by a factor of 1.8 *by the optimized cavity and by a factor of* 3.1 *by the optimized grating structure under laser illumination at a wavelength of* $1523\,\mathrm{nm}$ *under an initial irradiance of* $4337\,\mathrm{W/m^2} \pm 223\,\mathrm{W/m^2}$.

7.1 Filter Structures Based on Amorphous Silicon Carbide

The filter structures simulated in the section above were all based on a combination of two different layers with different refractive indices. One possibility to achieve homogeneous, thin layers with variable refractive indices is the use of a-Si_xC_{1-x}:H, where the refractive index can be tuned with the silicon to carbon ratio [155]. The peak reflectance for a filter structure depends on the number of layers and on the refractive index contrast. This means less layers are required to obtain a certain peak reflectance if the refractive index ratio between the two layers is higher. Therefore, it would be desirable to maximize the refractive index contrast, in principle, going from amorphous carbon to amorphous silicon. However, silicon-rich layers tend to have a island-like growth [156]. As thin homogeneous layers are required for the filter structures, the composition is restricted to stochiometric and carbon-rich layers.

All processes used in this work used a deposition set-temperature of 400 °C. This temperature is measured at the bottom of the sample holder, thus this corresponds to an actual sample temperature of around 280 °C [177]. This elevated temperature is required to enhance surface diffusion and thus, leads to a more homogeneous deposition. The heating cycle is carried out in a hydrogen atmosphere with a pressure of 0.3 m bar.

7.1.1 PECVD with Coupled Microwave and Radio-Frequency Plasma

For the first deposited layers, silicon as well as float-glass substrates were used. To remove the native oxide on the silicon surface, a cleaning cycle is carried out using an argon-powered hydrogen plasma before the deposition

was started. The process parameters of this cleaning cycle are shown in Table 7.1. As shown in simulations, the use of a third layer with an intermediate refractive index did not show any advantages (see Figure 6.12), thus, only two different processes were used. The first process resulted in a low-index layer at a refractive index of $n_{\text{low}} = 1.8$ whereas the second process led to a high-index layer with a refractive index of $n_{\text{high}} = 2.5$. These two processes differ only in their methane to silane gas flow ratios. The complete set of process parameters is given in Table 7.1. These processes were based on [162].

	Ar	H_2	CH_4	SiH_4	pressure	rf-power	MW-power
		[sccm]			[mbar]	[W]	[W]
cleaning	30	70	0	0	0.3	35	0
low-index	30	0	110	7	0.05	150	1000
high-index	30	0	50	50	0.05	150	1000

Table 7.1: Process parameters for the coupled microwave and radio-frequency plasma processes

The layer thicknesses and dispersion relation were determined from ellipsometry measurements. For all these measurements of the a-Si_xC_{1-x}:H-layers, a Tauc-Lorentz model was used [172, 173, 178]. This model describes the refractive index variations of the amorphous semiconductor very well.

To determine the deposition rates of the two different process, a set of samples were produced using these processes and varying deposition times. It was found that the layer thickness increases linearly with the deposition time in the investigated range. Using this assumption of a linear relation, the deposition rate of the low-index a-Si_xC_{1-x}:H layer was determined to be 18.8 nm/ min $\pm$ 0.28 nm/ min. The stoichiometric

high-index layer grows much faster with 70.2 nm/ min ± 0.86 nm/ min on the silicon substrate. On a glass substrate, the deposition rates were determined to be 51.6 nm/ min ± 0.90 nm/ min for the low-index layer and 98.5 nm/ min ± 1.08 nm/ min as shown in Figure 7.1.

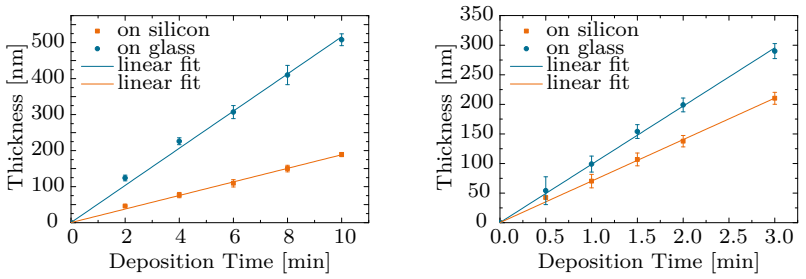

(a) low-index layer (b) high-index layer

Figure 7.1: Determination of the deposition rate for the low-index and the high-index layer deposited on silicon and glass. The low-index layer shows a much lower deposition rate due to the lower silicon ratio and the deposition rates are much larger for the layers deposited on glass compared to those on silicon.

The differences in the deposition rate for layers deposited on glass and on silicon can be attributed to different reasons: first, the substrates have very different thicknesses, the silicon wafer has a thickness of 250 µm compared to the 1 mm glass substrate, this influences the temperature and the bias voltage. Second, the bias voltage across the insulator is expected to differ from the bias voltage across the semiconductor resulting in different deposition rates. A third reason for the different deposition rates is the different surface morphology, the silicon substrate offering a crystalline structure compared to the amorphous nature of the glass surface. Thus, the deposition times had to be adapted to the kind of substrate used and it was not possible to deposit filter structures with the

same characteristics in the same deposition process on glass and on silicon.

Apart from the type of substrate, the reactor condition plays a role and slightly influences the deposition rate, this influence was minimized using a defined pre-dip, where a rather thick dense layer of a-Si_xC_{1-x}:H was deposited to cover the substrate holder and the reactor walls. This was carried out for all deposition processes to ensure defined reactor conditions. Additionally, the reactor chamber was etched back in defined intervals. The remaining small variations were determined by depositing reference layers for both processes and do an ellipsometry measurement prior to the actual filter deposition to adapt the deposition times, if neccessary.

Figure 7.2 shows an scanning electron microscope (SEM)-cross-section of a Bragg-structure consisting of eight layers on the left and the corresponding reflectance on the right. The structure was deposited on silicon. The peak at a wavelength of 1800 nm is clearly visible and rather broad due to the low number of layers forming the stack. The plateau region below the peak down to a wavelength of around 1100 nm with a reflectance of around 30 % is caused by the reflection at the rear surface of the silicon substrate. As silicon is transparent for photons in this wavelength range, these photons reach the rear surface and are reflected there. The value of around 30 % comes from the refractive index contrast of 3.5 for the silicon against air, which leads to a reflectance of 30.9 % according to Fresnel's equations. Looking at the SEM-image, the two layers with different silicon to carbon ratios are clearly distinguishable and show a columnar growth. Furthermore, the layers are homogeneous and nicely closed.

The filter structures were subsequently optimized in order to obtain a high reflectance up to a wavelength of 1150 nm for the UC-filter and from 1500 nm upwards for the SC-filter. As the refractive indices of the layers were fixed by the processes used, there were only two leverages for improvement. First, the number of layers was increased to reach reflectances

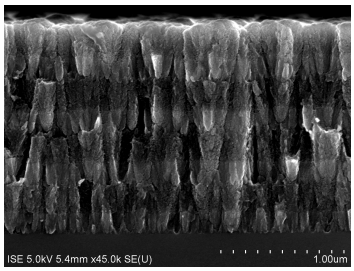

(a) SEM-picture

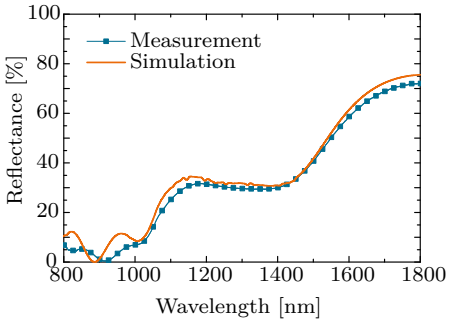

(b) Simulated and measured reflectance

Figure 7.2: SEM-image and Reflectance characteristics of a Bragg-stack consisting of 8 layers on silicon. The reflectance plateau between 1100 nm and 1400 nm originates from the reflection at the rear surface of the silicon substrate.

above 95 %. Figure 7.3 shows the measured reflectance for the two types of filter structures consisting of 20 layers for the UC-filter and 13 layers for the SC-filter. Second, the layer thicknesses were optimized using the evolutionary algorithm described in Subsection 6.3.2. Figure 7.3 shows the reflectance characteristics of both filter types optimized by this algorithm. Already in the optimized simulations for the UC-filter there is a slight splitting into two separate peaks instead of the single Bragg-peak. The process variations lead to a further splitting of these two peaks (as shown in Figure 7.3). However, still peak reflectances above 90 % could be reached with these configurations for both filter structures using only 13 layers for the SC-filter. Furthermore, the reflectance in the transmission regions is low: for the SC-filter, the reflectance oscillates around 15 % and for the UC-filter, the reflectance is below 10 % over a large range apart from the side-lobe at around 1250 nm.

SEM-images of the polished cross-sections of the filter structures shown

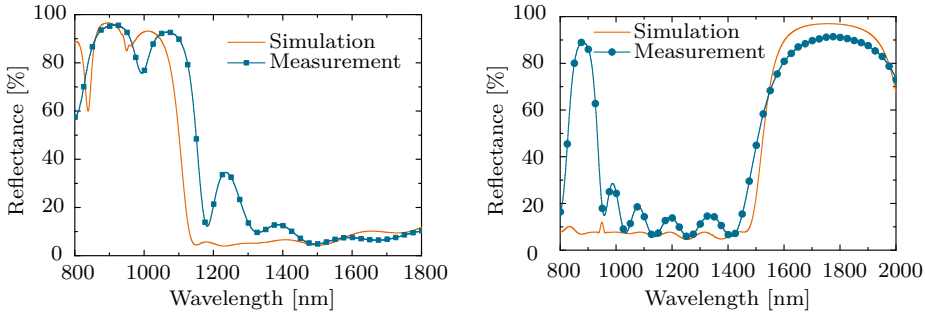

(a) UC-Filter (b) SC-Filter

Figure 7.3: Reflectance characteristics of the UC-filter consisting of 20 layers on the left and of the SC-filter consisting of 13 layers [164].

in Figure 7.3 are depicted in Figure 7.4. For the SC-filter, the SEM-image revealed a problem with the deposition process leading to the second peak at around 900 nm (see Figure 7.3). It shows that the low-index layers, shown in the lighter grey are thicker than desired. The reflectance of the stack could be reproduced by simulations using the layer thicknesses determined from the SEM-image. For the UC-filter, a similar trend is shown, the low-index layers are thicker than assumed in the simulations. This also leads to the splitting of the reflectance peak, which was found to be larger than in the simulations.

The main drawback of these processes was the homogeneity of the deposition, which was good over a small area, but over the sample area of $7.5\,\mathrm{cm} \cdot 2.5\,\mathrm{cm}$, variations were visible with the naked eye. In order to improve the homogeneity over a larger area, pulsed microwave sources were mounted replacing the continuous wave microwave sources.

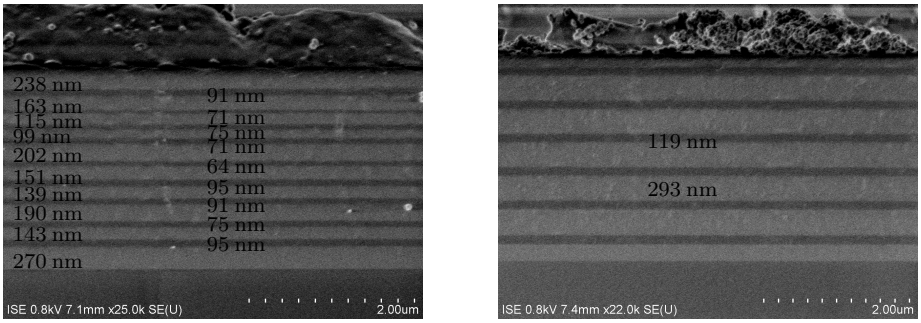

(a) UC-Filter (b) SC-Filter

Figure 7.4: SEM-pictures of the SC- and UC-filter deposited using coupled microwave and radio-frequency on a glass substrate [164].

7.1.2 PECVD Using a Pulsed Microwave Plasma

After replacing the continuous microwave sources with pulsed ones, new processes had to be developed based on the processes described above.

We tried to establish pure microwave-based processes, using only the two microwave sources without the additional rf-source. The microwave sources have a maximum power of 2000 W, each, and are pulsed, the pulse duration and the idle time between the pulses are variable. Here, we investigated a variation of the set power and the pulse duration. The idle time was kept at 17 ms and 18 ms for the two sources. The power was varied between 500 W and 1500 W and the pulse duration between 5 ms and 15 ms. The most stable processes for both layers could be obtained for a power of 1500 W and a pulse duration of 10 ms. The layers that were deposited using these processes showed refractive indices of $n_{\text{low}} = 1.6$ and $n_{\text{high}} = 2.3$, thus lower values than those that had been obtained with the previous processes. The main reason for this is probably an increased incorporation of hydrogen into the layer, leading to a less dense layer.

In the previously described processes, the additional rf-power led to more ionic bombardment of the sample surface, increasing the density. Although the absolute values were lower, the contrast between the two layers was still high enough to produce good filter structures using a reasonable number of layers. The layer thicknesses determined from simulations based on the layers obtained above, had to be adapted according to the refractive index of the new obtained layers.

The cleaning cycle with hydrogen that was carried out in conjunction with the previous processes, was not necessary anymore as all structures were deposited on glass substrates.

	Ar	H_2	CH_4	SiH_4	p	MW-Power	t_{pulse}	t_{idle}
		[sccm]			[mbar]	[W]	[ms]	[ms]
n_{low}	30	0	110	7	0.05	1500	10	17/18
n_{high}	30	0	40	60	0.05	1500	10	17/18

Table 7.2: Process parameters for the pulsed microwave plasma processes

The layers deposited with the pulsed microwave plasma described above, showed a much better homogeneity than those with the coupled rf-MW and continuous MW-plasma at the bottom. For the sample produced with the coupled rf-MW-process, the thickness variations of up to 15.7 % were obtained over the sample surface as determined by ellipsometry. This homogeneity could be improved by the pulsed MW-processes, where a maximum thickness variation of 3.4 % was found. This comparison is based on the samples obtained from the deposition time variations for both types of processes on glass substrates.

Like for the processes described above, a variation of the deposition time was carried out to determine the deposition rate for both processes. To investigate the process variations, this series was carried out on two

different days with different reactor conditions. To reduce the effect of the reactor condition, a pre-dip was carried out. As shown in Figure 7.5, the samples produced on the two different days agree very well, thus the pre-dip is a good mean to reduce the effects of the reactor condition. However, still test layers were deposited before a filter deposition to determine the exact deposition rate and adapt the deposition times.

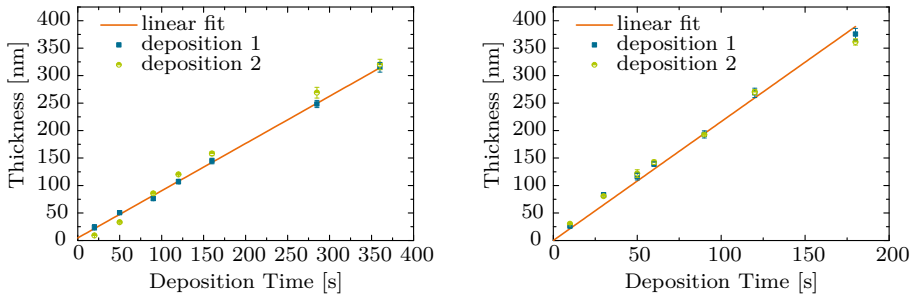

(a) low-index layer (b) high-index layer

Figure 7.5: Determination of the deposition rate for the low-index and the high-index layer deposited on glass for the pulsed MW processes.

From the variations of the deposition time for the two different processes, deposition rates were determined, the deposition rate for the low-index layer was pretty similar to those determined for the coupled rf-MW-processes with a value of 54.6 nm/ min ± 0.56 nm/ min. The high-index layer grows even faster with 127.6 nm/ min ± 1.52 nm/ min, this deposition rate is in principle still slow enough to ensure a good control over the layer thicknesses, which is sufficient for a well-controlled deposition of the Bragg-stacks.

Additionally to the Bragg-stacks with $\lambda/8$-layers, filter structures were further optimized for the application using the evolutionary algorithm

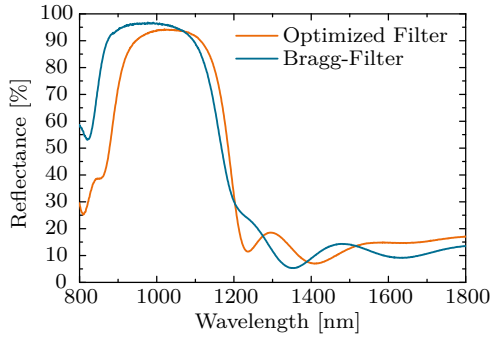

Figure 7.6: Comparison between the measured reflectance characteristics of an adapted Bragg-structure and an optimized filter structure.

described in Section 6.3.2. This optimization was based on a variation of the layer thicknesses. The benefit of these optimized filter structures was mainly their better transmittance in the respective regions. The oscillations in this region could be reduced in simulations going from the Bragg-condition to layers with arbitrary thicknesses. In order to benefit from this optimization, the deposition process has to be very well controlled with variations in the range of several nanometers. If we consider a Bragg-stack deposited using these layers, a thickness variation of 1.1 nm in the high-index layer and correspondingly of 1.4 nm in the low-index layer shifts the peak reflectance by 10 nm.

Figure 7.6 shows the reflectance characteristics of a Bragg-stack and an optimized filter structure consisting of 13 layers, each. It shows that the theoretical benefit of the optimized structure does not necessarily translate into superior reflectance characteristics in the measurement. The reason for this was investigated in a Monte-Carlo simulation approach which showed that the process variations for the currently used processes are too large to benefit from the optimization process (see Table 6.1). The opti-

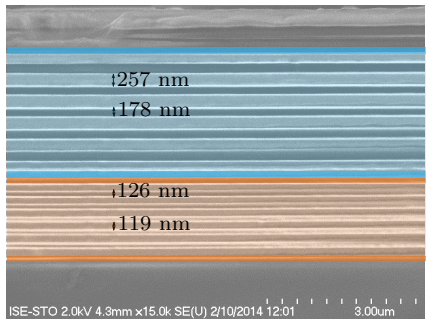

(a) SEM image of the combination of both filter types

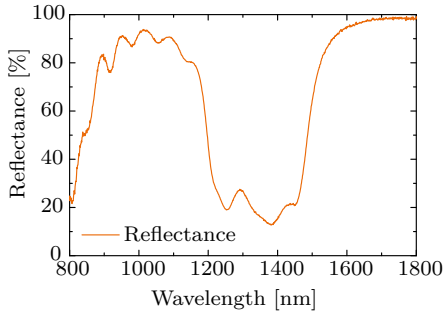

(b) Reflectance of the combination of both filter types

Figure 7.7: SEM-image and reflectance characteristics of the combination of both filter types. The layers colored in blue form the SC-filter, whereas the orange ones form the UC-filter. The layers in lighter color denote layers with a thickness of $\lambda_{\mathrm{des}}/4$, the darker ones those on top and bottom of each filter with a thickness of $\lambda_{\mathrm{des}}/8$.

mized filter structure was less stable against process variations than the Bragg-structure. In other words, the maximum found by the optimization was not as broad as the one of the Bragg-structure.

Still, very good reflectance and transmittance characteristics could be achieved for the two filter types using Bragg-based structures, the UC-filter and the SC-filter using only 13 layers with peak reflectances of above 90 % and a good transmittance in the other regions.

The reflectance of the combination of both filter types and an SEM-image of the combined structure is shown in Figure 7.7. The complete structure, thus, consists of 26 layers where each filter structure consists of 11 layers complying to the Bragg condition and 2 layers with optical thicknesses corresponding to $\lambda_{\mathrm{des}}/8$.

In conclusion, the filter structures for the system with silicon solar cells and upconverters sketched in Figure 2.3 can be prepared using a-Si_xC_{1-x}:H deposited by PECVD-processes. Peak reflectances above 95 % could be reached for both filter types, whereas the transmittance between the reflectance peaks is also above 80 %. A further optimization of the filter structures, however, was not possible due to the lower stability of the theoretically optimized structures to process variations.

A benefit of the filter structures on the performance of the system shown in Figure 2.3 could not be shown. Due to the low quantum yield of the NQDs an effect of the spectral concentration was not visible. Therefore, the filter structures were not required for the system. They could, however, be applied to directly incorporate the upconverter into photonic structures as shown in the next section.

7.2 Upconverter Within Photonic Structures

The second approach investigated in this work aims for a direct incorporation of the upconverter material into a photonic structure environment. This leads to a variation of the local irradiance and the local density of states. The effect was shown in simulations (see Section 6.4 to Section 6.6). With the simulations, the structure parameters had been optimized for the effect on the upconversion processes.

To experimentally verify the influence of photonic structures on upconversion mechanisms, two different structures were investigated: the cavity structure and the surface grating structure. Both structures were realized based on upconverter nanoparticles embedded in PMMA. The upconverter nanoparticles consisted of β-$NaYF_4$ doped with 25 % Er^{3+} surrounded by an un-doped shell. The doping concentration in the rate-equation model

that is used for comparison is 20 %, thus, close to the doping concentration of the nanoparticles. The nanoparticles were synthesized by my colleague Stefan Fischer during a visiting stay at the University of Victoria in the group of van Veggel. The suspension with these nanoparticles stabilized by PEG together with PMMA in toluene was prepared as described in 5.2.3. The concentration of the solution was set to the 10 wt% PMMA to toluene as this concentration offered good control over the layer thickness in the range from 350 nm to 850 nm. This covered the target thicknesses for the cavity structure as well as for the grating structures.

With these solutions, a variation of the rotation frequency ω was performed to be able to establish a model for the dependence of the thickness on the angular frequency. The thickness d of all deposited layers was determined from ellipsometry measurements using a Cauchy model on nine points distributed over the sample area. For comparison, some layers have also been scratched and measured by profilometry, which led to the same thicknesses in the range of measurement uncertainties. The resulting curve of thickness versus spinning frequency was fitted using the model described in 5.1 [169]. Figure 7.8 shows the dependence of the layer thickness on the angular frequency. The orange dots denote the measured thicknesses including the measurement uncertainty given by the standard deviation of the values at nine mesurement points each on three samples. The blue line shows the fit using the parameters shown in Equation 7.1.

According to this model, the thickness of the layer could be determined by:

$$d = \left((13184 \pm 2839) \cdot \omega_{rot}^{(-0.40185 \pm 0.02471)} \right) \text{ nm}. \tag{7.1}$$

Here, the angular frequency ω_{rot} is inserted in rotations per minute to obtain the thickness d in nm. The uncertainties are obtained from the

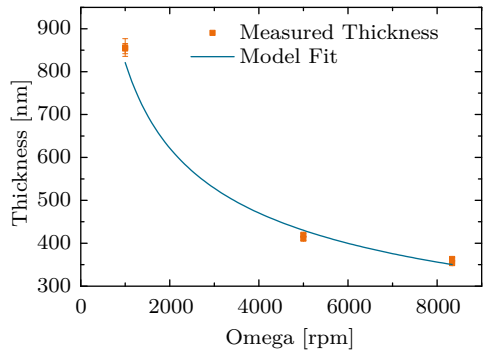

Figure 7.8: Thickness model fit for the doped PMMA layers.

fit. Similar variations of the angular frequency and model fits were carried out for the reference PMMA-layer.

7.2.1 Upconverter Within a Cavity

The first structure investigated was the cavity structure consisting of a rear-reflector to increase the local irradiance and a cavity to enhance the emission probability for the dominant emission process. The investigation of this structure was started in the diploma thesis of Sebastian Wolf [130]. The optimization of the structure parameters is described in Subsection 6.4.1. The thickness of the buffer layer was set to zero, as a similar irradiance enhancement could be achieved without the buffer layer (see Figure 6.15), thus, one cavity filter was deposited right on top of the rear reflector. The target thickness for the upconverter layer within the cavity was 800 nm. In principle, the two filter structures required for this structure were very similar to the ones used in the previous section. The cavity filter is very similar to the UC-filter whereas the rear reflector resembles the SC-filter.

As we were still aiming for upconversion from the infrared (1523 nm) to

the near-infrared (980 nm), absorption in the visible was not a major drawback, thus, the filter structures were also produced based on a-Si_xC_{1-x}:H deposited by PECVD using the same processes described above. The upconverter material, however, could not be deposited by PECVD and was deposited by spin-coating. Therefore, the deposition could not be carried out in one run. Instead, in a first step, the filter structures required above and below the upconverter layer were deposited on separate glass substrates by PECVD using the processes developed in the previous section. In the next step, doped PMMA-layers with half the desired thickness were spin-coated on both halves of the structure. The two halves of the structures were subsequently combined in a hot-emboss process, which was developed by Sebastian Wolf during his diploma thesis [130]. During this process, the samples were placed on top of a sheet of PTFE and the process was carried out under vacuum. The optimized process parameters were:

Phase	1	2	3	4	5
T [°C]	100	80	60	40	30
p [bar]	100	100	100	100	100
t [min]	12	3	3	3	3.

Depositing the upconverter layer only on one half did not lead to a proper combination of the two halves.

Using the silicon-carbide filters four different structures were realized to be able to separate the different effects. Additionally, a reference layer with identical thickness was deposited on glass. The first structure called rear-reflector (RR) consisted of the doped PMMA-layer deposited on the rear-reflector. This structure allows for determining the effect of the irradiance enhancement. For the second structure called rear-side structure (RSS), the upconverter layer was deposited onto a combination of both filter types

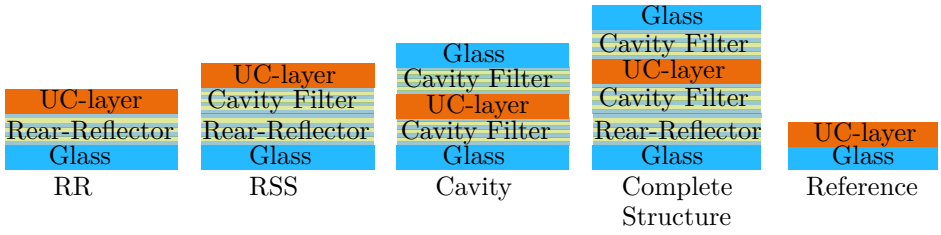

Figure 7.9: Sketch of the realized cavity structure samples. The upconverter layer is denoted in orange, the glass substrate in light blue and the filter structures in dark blue. The samples consisted from left to right of the upconverter layer deposited on a rear-reflector and on both filter types, of an upconverter layer enclosed by two filters forming the cavity and the same structure with a rear-reflector. As a last sample, a reference on glass was prepared.

forming the rear side of the complete structure. For the third structure, the cavity structure, the upconverter layer was embedded between the two cavity filters. Thus, this structure allows for investigating the effect on the emission properties. Finally, the last structure investigated was formed by a combination of the cavity and the rear-reflector. Here, both effects are exploited, the local irradiance enhancement due to the rear-reflector and the emission enhancement due to the cavity. All structures are sketched in Figure 7.9.

The first two structures shown in Figure 7.9, can be obtained by directly spin-coating the PMMA-solution including the nanoparticles onto the glass substrate covered with the respective filter structures.

The PMMA used here had a molecular weight of 120 kg/mol. This is important, as the molecular weight has an influence on the glass transition temperature. For the material used here, the glass transition temperature

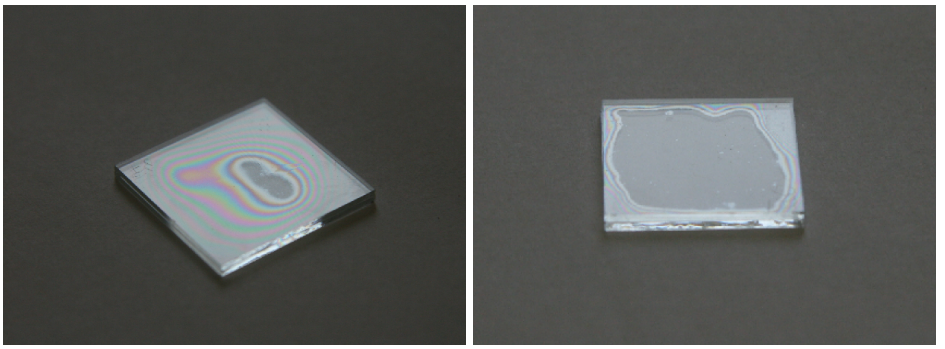

Figure 7.10: Comparison of a sample with air inclusions on the left and a well-combined sample on the right [130].

lies at around 105 °C under normal pressure. To proof a combination without air inclusions, reflectance measurements were taken of combined PMMA on glass samples. The reflectance of the samples combined with the process above showed a reflectance of around 8 %, which is basically the same reflectance as a single glass substrate. Looking at structures with an air gap in between the two halves, interference rings show up, which are not present in middle of the well-combined structures as shown in Figure 7.10.

Additionally, the effect of the hot-emboss process on the layer thicknesses was investigated. For this purpose, glass substrates were covered with 100 nm of the high-refractive index a-Si_xC_{1-x}:H. As described above, PMMA was spin-coated onto both halves. The same PMMA-layer was also deposited on a glass substrate without a-Si_xC_{1-x}:H to simplify the determination of the layer thickness with ellipsometry. The thickness was determined to be (490 ± 4) nm. These layers were subsequently combined using the process described above and the reflectance of the combined samples was measured. This measurement was subsequently compared to a TMM simulation of the same stack. The thickness of the PMMA-layer

was taken as a parameter to optimize the agreement between the simulation and the measurement. The best correspondence was found for a total layer thickness of 981 nm. This thickness corresponds very well to twice the thickness of the single layers. Thus, in the following, we assumed that this process does not considerably change the total thickness [130].

The reflectance of one of the used cavity filters and the rear-reflector is shown in Figure 7.11. For the cavity filter, a very high reflectance around 980 nm is required to realize the cavity as well as high transmittance at 1523 nm to ensure that the incident light reaches the upconverter. For the rear-reflector, only a high reflectance at the incident wavelength of 1523 nm is required.

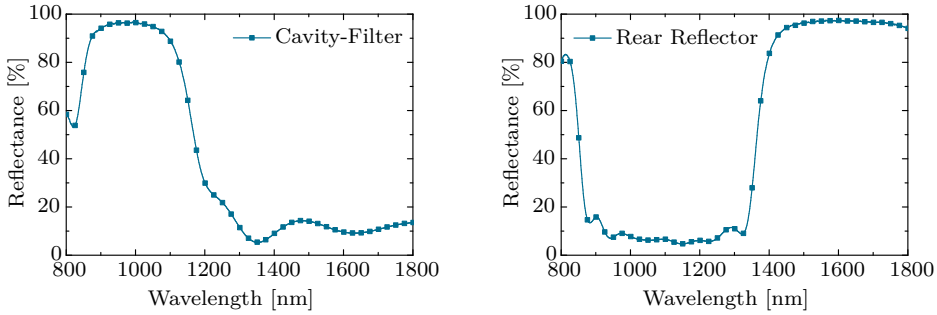

(a) Cavity-filter (b) Rear-reflector

Figure 7.11: Reflectance characteristics of the two filter types used for the cavity structure.

Using these filter structures and the developed hot-embossing process, the different structures sketched in Figure 7.9 were prepared. In total, six samples of the RR-structure, four of the RSS-structure, three Cavity-samples, three references and four complete structures were prepared. Figure 7.12 shows exemplary photographs of the different structures.

Subsequently, the photoluminescence of the samples was measured in

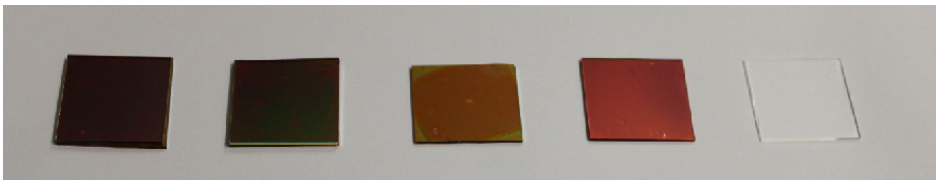

Cavity | Complete Structure | Rear-Side Structure | Rear Reflector | Reference

Figure 7.12: Photograph of the various cavity samples. From left to right, the cavity, the complete structure, the layer on the rear-reflector, on the rear side structure and the reference sample are shown.

the integrating sphere setup described in Subsection 5.3.2. The upconverter was illuminated using a laser emitting at a wavelength of 1523 nm with a power of 10 mW. This power corresponds to an irradiance of $4337\,\mathrm{W/m^2} \pm 223\,\mathrm{W/m^2}$ over the spot area. The error for the irradiance is determined from measurements of the spot size.

In order to obtain the luminescence over the whole wavelength range, the detected spectrum has to be corrected for the detector sensitivity. This sensitivity correction curve $f_{vis,NIR}$ had been obtained by measuring a reference lamp spectrum in the integrating sphere setup with the spectrograph and dividing the real lamp spectrum by the measured spectrum. All measured spectra were corrected using this correction function. A comparison between the corrected luminescence signals averaged over all samples is shown in Figure 7.13. It shows that the highest luminescence signal occurs for the complete structure, directly followed by the RR- and RSS-structure. All these samples show a considerable luminescence enhancement compared to the reference. For the cavity structure, however, a reduction of the signal is found. This might be due to reflections of the incident laser beam at the filter before it actually reaches the upconverter

material. All luminescence signals shown in Figure 7.13 were obtained by integrating 10 times over 20 s under excitation at a wavelength of 1523 nm and an irradiance of 4337 W/m^2 ± 223 W/m^2.

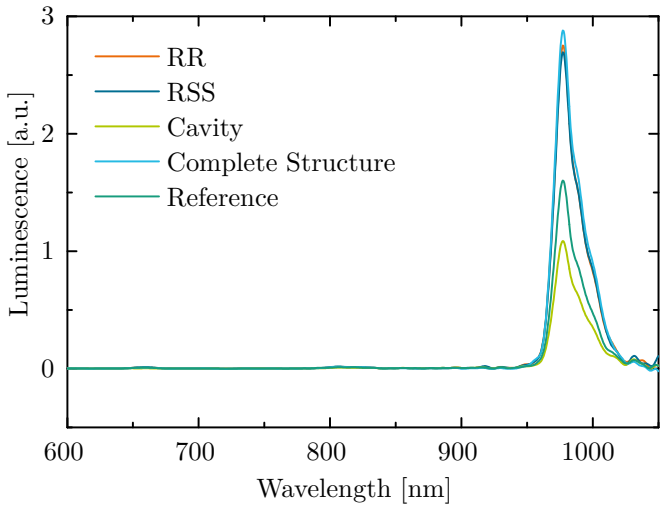

Figure 7.13: Comparison of the corrected luminescence signal of the various cavity structures. The highest signal is found for the complete structure shown in light blue, directly followed by the rear-reflector and the rear side structure (in orange and dark blue). The reference, shown in dark green, has its luminescence maximum at around a factor of 2 lower and the lowest luminescence signal occurs for the cavity sample (shown in light green)

In addition to the dominant emission peak at around 980 nm, two emissions from higher levels should be visible in the spectrum. The first one occurring at around 800 nm corresponding to the emission from the $^4I_{9/2}$-level to the ground state and the second one at around 650 nm corresponding to the emission from the $^4F_{9/2}$-level to the ground state. Both

peaks occur in the uncorrected spectra but are barely visible in the corrected spectra for two reasons. First, these peaks are expected to be much smaller than those at the dominant emission wavelength. Second, the a-Si_xC_{1-x}:H used for the filter structures shows some absorption up to a wavelength of around 800 nm. Due to this absorption, the emission from the higher levels is not further investigated.

To further quantify the results of the luminescence measurement, the luminescence signal was integrated over the peak area between a wavelength of 950 nm and 1020 nm for all measurements. The integrated luminescence was subsequently normalized to the luminescence of the reference samples to obtain a luminescence enhancement to allow for a direct comparison to the simulated values. Figure 7.14 shows the comparison between the measured and the simulated luminescence enhancement for the various structures. The simulations were adapted to take the imperfect filter characteristics into account and they were again normalized to the simulation result of the reference structure. Thus, the actual layer thicknesses of the filters were used in the simulation. Furthermore, they were carried out with an upconverter layer thickness of 800 nm as this was the mean layer thickness determined from ellipsometry on upconverter layers on glass substrates. The error bars for the simulation account for the uncertainty of the laser irradiance. Thus, the simulation was carried out for initial irradiances of 4337 $W/m^2 \pm 223$ W/m^2. For the measurements, the error bars denote the standard deviation over all produced samples of the same structure group.

The simulations are carried out for an influence of only the spontaneous emission (SPE) (blue bars) and for an additional linear influence on the energy transfer (ET)-processes (green bars). Additionally, the correlation coefficients between both simulation methods and the measurements were calculated. If only the SPE is influenced, a correlation coefficient of 0.52

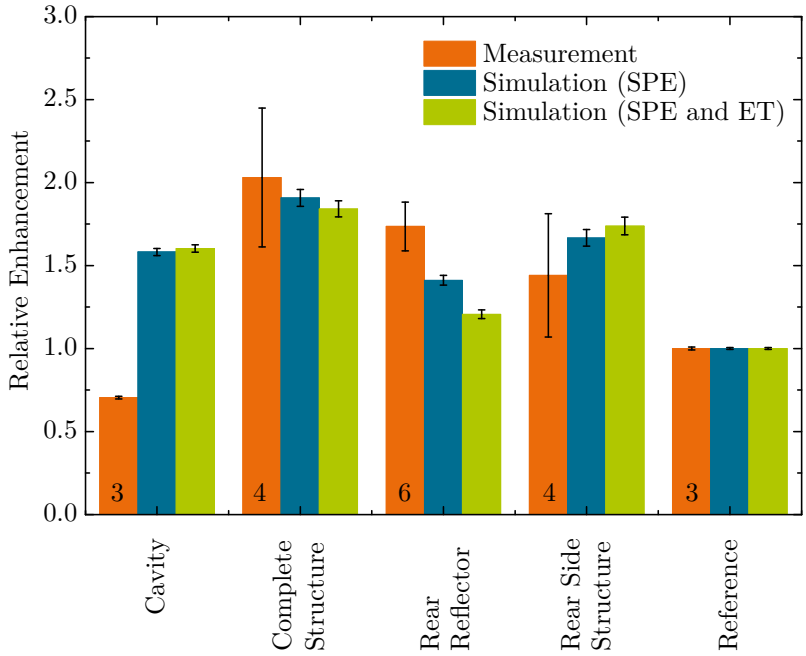

Figure 7.14: Comparison between the simulation and the experimental results for the different cavity structures. The numbers in the orange bars for the experimental results denote the number of samples produced in this category.

is obtained, compared to a value of 0.33 if an additional influence on the ET is considered. Unfortunately, it was not possible to determine the absorption with the setup currently used, due to the low absorption of the very thin layers of upconverter material. Therefore, it was also not possible to determine whether the luminescence enhancement is mainly due to an absorption enhancement or if the structure furthermore causes actual enhancements of the UCQY.

Table 7.3 gives an overview over the measured and simulated luminescence enhancement and over the simulated enhancement of the absorp-

Structure	$\overline{\gamma_{\mathrm{Lum}}}$ measured	$\overline{\gamma_{\mathrm{Lum}}}$ simulated	$\overline{\gamma_{\mathrm{Abs}}}$ simulated	$\overline{\gamma_{\mathrm{iUCQY}}}$ simulated
cavity	0.7 ± 0.01	1.58	1.30	1.22
complete structure	2.03 ± 0.41	1.91	1.38	1.38
Rear-reflector	1.74 ± 0.15	1.41	1.03	1.37
Rear side structure	1.44 ± 0.37	1.67	1.43	1.17

Table 7.3: Comparison of the simulated and measured luminescence, absorption and UCQY enhancement for the four different realized structures. All values are normalized to the reference simulation.

tion and the iUCQY. This shows the differences between the structures: whereas for the rear-reflector, the luminescence enhancement can be traced back to an enhancement of the UCQY, for the rear-side structure, the enhanced luminescence is mainly due to an enhanced absorption. The simulations predict a similar increase of the UCQY for the rear-reflector and the complete structure by a factor of 1.37 and of 1.38, respectively. For the cavity, an enhancement by a factor of 1.22 and of 1.17 for the rear side structure is predicted.

7.2.2 Upconverter in a Grating Structure

As described in Subsection 5.2.5, a h-PDMS-stamp was produced from an e-beam master produced at the FSU in Jena by project partners. The master consists of a 4″-silica wafer with 3×3 fields each at a size of 1 cm × 1 cm with linear grating structures of three different structure periods ($p_1 = 1.25\,\mu\mathrm{m}$, $p_2 = 1.5\,\mu\mathrm{m}$ and $p_3 = 1.6\,\mu\mathrm{m}$). This structure was subsequently metalized with 30 nm chromium to improve the durability of the master to the stamp production. An SEM-image of the different

structures on the master is shown in Figure 7.15. The stamp produced consists of two different layers, a thin top layer consisting of hard PDMS and a thick, soft bulk PDMS-layer. The hard layer is responsible for a good reproduction of the structure whereas the softer bulk material is needed to obtain a good contact between the stamp and the PMMA-layer into which the structure is embossed.

The stamp was produced as described in Subsection 5.2.5.

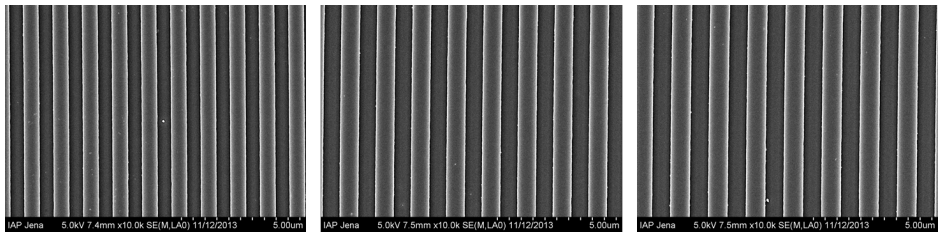

p_1=1.25µm p_2=1.5µm p_3=1.6µm

Figure 7.15: SEM image of the master structure used to produce the grating structures (Courtesy of M. Zilk (FSU Jena)).

The structure was transferred into thin PMMA-layers deposited by spin-coating as described above using again a hot-emboss process with the following parameters:

Phase	1	2	3
T [°C]	140	150	30
p [bar]	0	5	5
t [min]	5	30	20
Temperature ramp [s/K]	0	0	10

For the process, a stack of a brass plate, a glass plate, the glass substrates covered with the doped PMMA and the stamp bonded to glass was produced. The glass substrates had a size of 2.5 cm × 2.5 cm and were

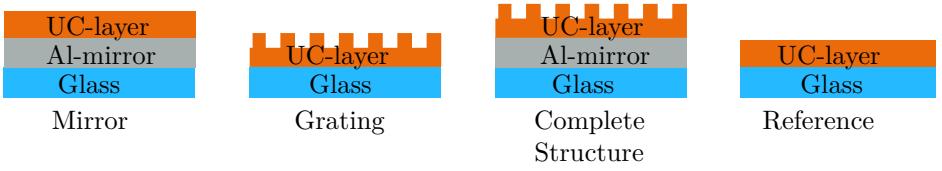

Figure 7.16: Sketch of the realized grating structure samples.

arranged in a way that each grating field on the master is positioned in the middle of one of the glass platelets. Thus, the nine fields on the master were transferred to nine samples.

The simulated structure consists of a rear-reflector, which had been simulated as a perfect metal, covered by a homogeneous upconversion layer of a thickness of 600 nm. This homogeneous layer is covered by a grating part with a thickness of 400 nm. In order to be able to separate the different effects, samples with and without metallic rear-reflector were produced as sketched in Figure 7.16.

Furthermore, three different structure periods were investigated, $p_1 = 1.25$ µm corresponding to the optimum value found by simulations, $p_2 = 1.5$ µm and $p_3 = 1.6$ µm, which show very similar rather low irradiance enhancement. The first structure period corresponds to a resonance in the grating region of the structure.

As a substrate for all samples, glass platelets were used. The mirror was deposited by evaporation of 2 µm of aluminum, where the bulk material shows a reflectance of 97.41 % at 1523 nm and 92.85 % at 980 nm [179]. Due to the low thickness of the layers, the reflectance measured with a Cary 500i spectrophotometer showed a reflectance of 91.1 % at a wavelength of 1523 nm and 79.8 % at 980 nm. These measured values are quite far from a perfect reflectance. Subsequently, an 800 nm thick layer of the doped PMMA was fabricated by spin-coating on all samples and the grating was

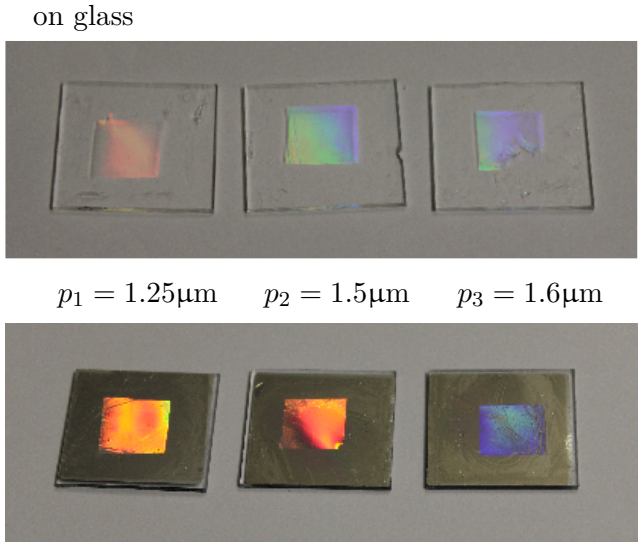

Figure 7.17: Photograph of the various grating samples.

hot-embossed into nine samples with and nine without the mirror layer. Assuming that the grating is filled completely during the hot-embossing process, this leads to a homogeneous layer with a thickness of 600 nm and the grating thickness of 400 nm as optimized by simulations. Figure 7.17 shows a photograph of all structures with embossed grating with the three different periods on glass and on the aluminum mirror.

To check how well the structure had been transferred into the doped PMMA-layer, atomic force microscope (AFM)-measurements were carried out. Figure 7.18 shows an AFM-image of a sample with an intended period of 1.25 µm. It shows very sharp edges and very well pronounced lines. Additionally, the depth of the grating was measured to be 372 nm, close to the intended 400 nm. Thus, the whole process chain including the stamp production and the embossing process seems to have worked very well. From the measurement, it looks like the valleys seem to have a lower

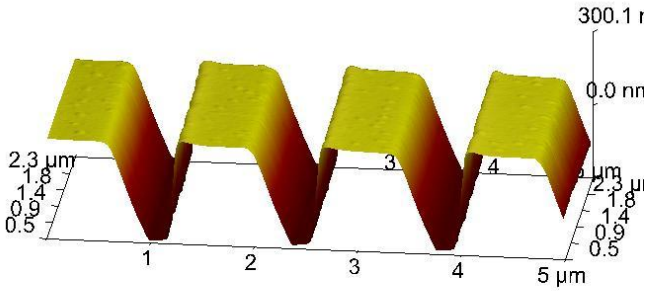

Figure 7.18: Atomic force microscopy image of a grating structure.

width, however, the fill factor of the master structure was very close to 50 %. This is expected to be a measurement artifact: it can be explained due to the limited reaction time of the tip, which was not sufficient to follow the very sharp edges.

On all samples produced, photoluminescence measurements were carried out using the integrating sphere setup described in Subsection 5.3.2. The laser power was set to 10 mW corresponding to an irradiance of 4337 W/m^2 $\pm$ 223 W/m^2 over the spot area. The excitation wavelength was 1523 nm and the spectra were obtained by integrating 10 times over 20 s. The samples were again placed into the integrating sphere using a centermount sample holder.

The luminescence is integrated over the peak from a wavelength of 950 nm to 1020 nm for the peak at 980 nm and normalized to the luminescence measured on the reference sample. The results of this normalization are shown as the orange bars in Figure 7.19. Additionally to the experimental results, the results obtained from the simulations are plotted. Here, two different approaches were investigated: the dark blue bars denote the simulation under the assumption that only the sponta-

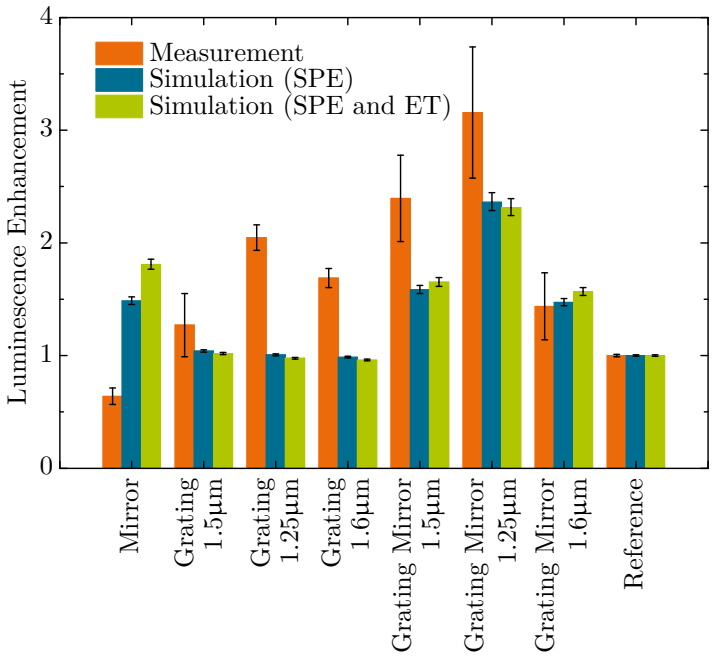

Figure 7.19: Comparison between the simulation and the experimental results for the different grating structures.

neous emission probability is varied by the variations of the LDOS. This corresponds to the simulation approach used throughout this work, following the arguments presented in [78, 79]. However, as this question is not completely solved, yet, further simulations were carried out with a linear influence of the LDOS on the energy transfer processes as described in [80]. These results are shown as green bars. Calculating the correlation between the experimental results and the two different simulation methods, a correlation coefficient of 0.64 is obtained for the correlation between the experimental results and the case where only the spontaneous emission is influenced compared to a factor of 0.47 for the case where the

energy transfer is also influenced linearly by the LDOS. The differences between the two simulation approaches are rather small, so this is by no means a proof for the independence of the energy transfer processes from the LDOS-variations. However, we took this as an indication that our simulation approach is correct.

The error bars shown for the simulations result from taking the standard deviation determined for the laser irradiance into account. All results are normalized to the values obtained from the measurement or the simulated luminescence of the reference sample, respectively.

Figure 7.19 shows that for the grating structures without the mirror, the trend of improvement by the different grating periods is not reproduced in the simulations. This is due to another simplification that was used for the simulations: the structures are simulated without any absorption and the refractive index was 1.5. Thus, for the simulations, there is no refractive index contrast between the upconverter grating and the glass below which leads to no reflection at the interface. Whereas in the real structure, this leads to a small but beneficial wave-guiding effect in the upconverter layer, this does not occur in the simulations. Therefore, no effect of the structure period is found and the luminescence basically equals that of the reference. To verify this hypothesis, the simulations for these structures should be repeated including the absorption of the nanoparticles and using a measured value for the refractive index of the doped PMMA layer which slightly deviates from the glass. Doing this, it should be possible to reproduce the trend showing for the measured enhancement for the different structure periods with the simulations.

For the mirror samples, the measured luminescence is even lower than for the reference. This is not reproduced by the simulations, where an enhancement by a factor of around 1.5 is predicted. Due to the reflection at the mirror, an interference pattern within the upconverter layer is

produced, leading to maxima and minima in the irradiance distribution. What differs between the simulation and the experiment is the quality of the mirror: a perfect metal is investigated in the simulations compared to the aluminum mirror in the measurements. Thus, any parasitic absorption does not occur in the simulations, furthermore, the reflectance at the incident wavelength is lower. As this reflectance was measured to have a value of still 91.1 %, this does not explain the significant drop in luminescence enhancement down to 63.9 % of the reference. Therefore, we assume that the main effect reducing the measured luminescence is absorption within the metal. However, imprinting the grating into these structure leads to a dramatic improvement. For these grating structures on aluminum, the simulations predict the trends of the luminescence enhancement very well. Actually, the experimentally determined luminescence enhancement is even larger than the values predicted by the simulation approach. One possible explanation for this behavior could be the excitation of surface plasmons on the aluminum surface. Additionally, the variations of the LDOS were determined only in the two-dimensional simulation setup instead of real three-dimensional space. Furthermore, the rate-equation model was developed for micro-crystalline material and does not necessarily describe the exact behavior of the nanoparticles. Considering all assumptions and simplifications made in the simulations, the correspondence between the simulation approach and the measured luminescence enhancement is very good for these structures.

In addition to the most dominant emission around 980nm, the emissions from higher levels can be investigated for this structure. This was not possible for the cavity structure shown above due to the onset of absorption in the a-Si_xC_{1-x}:H-layers. Here, we can quantify these results under the assumption that the absorption of the aluminum mirror does not change considerably down to a wavelength of 650nm. Figure 7.20 shows again the

comparison between measured and simulated luminescence enhancement using again the same simulation approaches.

Again, the orange bars represent the measurement, the blue and green bars the simulations. For the blue bars, the LDOS influences only the spontaneous emission whereas for the green bars, it additionally influences the energy transfer processes. Taking these comparisons into account for the correlation coefficient, this value rises to 0.87 for the LDOS-influence on the spontaneous emission only compared to a value of 0.73 if the energy transfer rate is also influenced.

As described in the previous chapters, from the rate-equation model, not only the luminescence enhancement but also the effect on the iUCQY can be determined. For the optimized grating structure, the quantum yield is increased by 37 % compared to the reference under an irradiance of $4337\,\mathrm{W/m^2}$. Thus, according to the simulations, the luminescence enhancement is not only due to an absorption enhancement, but a considerable enhancement of the UCQY is achieved.

The results for the other simulated structures normalized again to the simulated reference are given in Table 7.4. They show that for the grating structures, the absorption is rather decreased than increased leading to a still positive effect on the iUCQY whereas the luminescence is hardly affected or even decreased. For the mirror structure, the main effect is the absorption enhancement, which is basically responsible for the luminescence enhancement, the iUCQY is only slightly improved. For the grating structures on the mirror, both, the absorption as well as the quantum yield are considerably increased leading to the luminescence enhancement.

In conclusion, it was shown in this subsection that the upconversion luminescence for the most dominant emission around 980 nm can benefit considerably from incorporating the upconverter into photonic structures.

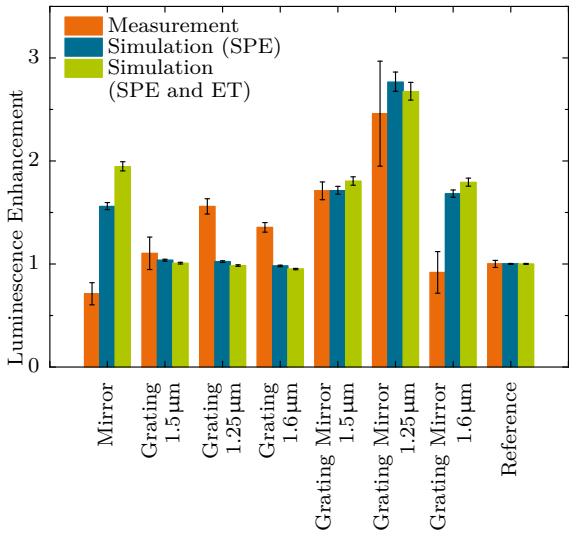

(a) Emission enhancement at 800 nm

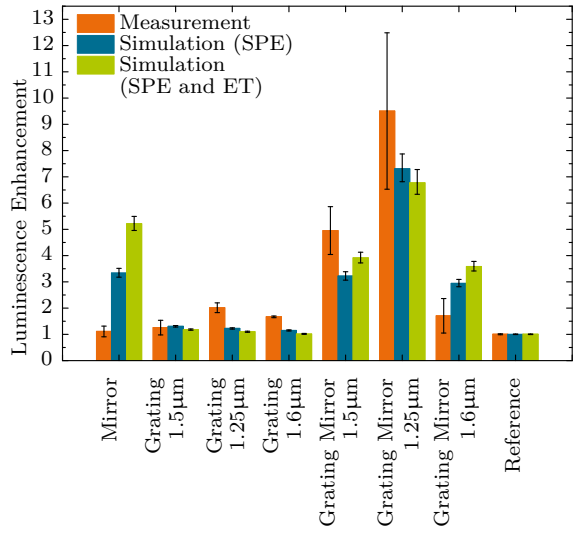

(b) Emission enhancement at 650 nm

Figure 7.20: Comparison of the simulated and measured luminescence enhancement for the emissions from energetically higher levels.

Structure	γ_{Lum}	$\overline{\gamma_{\mathrm{Lum}}}$	$\overline{\gamma_{\mathrm{Abs}}}$	$\overline{\gamma_{\mathrm{iUCQY}}}$
	measured	simulated		
grating (p=1.25 µm)	2.1 ± 0.1	1.0	1.0	1.0
grating (p=1.5 µm)	1.3 ± 0.3	1.0	1.0	1.0
grating (p=1.6 µm)	1.7 ± 0.1	1.0	1.0	1.0
mirror	0.6 ± 0.1	1.5	1.4	1.0
grating mirror (p=1.25 µm)	3.2 ± 0.6	2.4	1.7	1.4
grating mirror (p=1.5 µm)	2.4 ± 0.4	1.6	1.3	1.2
grating mirror (p=1.6 µm)	1.4 ± 0.3	1.5	1.3	1.1

Table 7.4: Comparison of the luminescence, absorption and UCQY enhancement for the seven different realized structures. All values are normalized to the reference simulation. It shows that, whereas for the grating structure, mainly the UCQY is affected and for the mirror mainly the absorption, for the grating mirror structures, both parameters are considerably increased.

The embossing of the grating increased the luminescence by a factor of 4.8 comparing the upconverter layer on a mirror before and after the embossing of the grating and by a factor of 3.1 compared to the reference for the optimized structure period of 1.25 µm. For the structures without the mirror, the increase is still considerable with a factor of 2.0. These very promising results for the luminescence enhancement are expected to be further improved by structuring the samples in two dimensions, thus, going from a linear to a crossed grating, based on theoretical analyses [180, 181].

It is very interesting to compare the results achieved in this work to what has already been reported in literature. A lot of work has already been carried out to enhance the photoluminescence of erbium at a wave-

length of 1530 nm. For example, the emission of erbium ions placed within a micro-cavity was investigated for quite some time, the first realization of an erbium-doped cavity was reported by Schubert *et al.* in 1992. There, erbium was ion-implanted into SiO_2 and an enhancement of the photoluminescence emission around 1530 nm by a factor of 50 was shown [124]. A similar structure was investigated in 1996 by Rigneault *et al.*, where erbium was excited at 488 nm and the emission around 545 nm was reported to increase by a factor of 26 [182]. Lipson *et al.* reported an enhancement by a factor of 20 for the emission at around 1530 nm under laser excitation at 488 nm [183]. In 2007, Almeida *et al.* also embedded erbium into a micro-cavity and found an enhancement of the emission at 1530 nm by a factor of 18 under excitation at a wavelength of 514.5nm.

In contrast, the observed enhancement factors for upconversion are considerably lower. An enhancement factor of 3.8 was found for a single erbium-ytterbium-co-doped upconverter particle in proximity to a metallic nanoparticle [53]. This enhancement was measured at an optimized position. In contrast, the optimized grating structure presented above achieved an enhancement by a factor of 3.2 over the much larger volume of the whole illuminated sample. A potential higher enhancement was reported by Niu *et al.* for a structure that also featured some grating-like characteristics. They investigated erbium-ytterbium co-doped β-$NaYF_4$-nanoparticles coated on top of an opal photonic crystal. They found a luminescence enhancement by a factor of around 27 for the emission at around 660 nm under excitation at 980 nm [77]. However, in their work the references is not clearly defined and part of the enhancement could be the result of a larger amount of nanoparticles being deposited on top of the rough opal surface, instead of the flat surface of the glass reference. With regard to the one dimensional structures like the optimized cavity structure also inverstigated in this work, an increase by a similar order

of magnitude was reported in literature. Johnson *et al.* reported an increase by a factor of around six for the dominant erbium upconversion emission at 980nm for a Bragg-stack consisting of 30 bilayers [75]. This enhancement factor was defined in comparison to the luminescence signal from the same stack at the angle, where the luminescence signal was the lowest. Here, again, the significance of the reference is a point of discussion, as in such a configuration the luminescence might be even decreased compared to the situation where no photonic structure is present at all, as I found in my theoretical work. Therefore, in this work, I compared the luminescence enhancement to single upconverter layers of the same thickness and obtained a factor of 2.0 for the optimized cavity structure.

In summary, one can state that also in comparison to literature good enhancement factors for the upconversion were achieved. However, defining suitable references and making results comparable between different works remains a challenge. The observed result can be described generally speaking by the theoretical models presented in this work, which is the major advantage in comparison to the literature, where no such comparison can be found.

8 Conclusion & Outlook

Within this work, photonic structures were produced for two approaches to beneficially influence upconversion processes.

First, photonic structures were applied as spectrally selective filter structures for a system combining spectral and geometric concentration. For this purpose, the photonic structures were simulated and produced based on the material system of amorphous silicon carbides. Within this system, the refractive index can be tuned with the silicon to carbon ratio [155], which offers a great flexibility without having to switch to another class of material. Based on existing coupled radio-frequency and microwave processes [162], processes for pulsed microwave deposition were developed. Using these different processes, filter structures with reflectances above 95 % and transmittances in the range of 85 % – 90 % in the respective spectral regions were produced. Furthermore, the stability of the filter characteristics to process variations was investigated. Here, it was shown that the stability of a Bragg-structure against process variations exceeds the stability of the adapted filter structures. Due to the variations in the currently used processes, the reflectance characteristics of the realized Bragg-structures were better than those of the realized optimized filters. A further improvement of the deposition parameters would be required to

further increase the process stability. This would offer the possibility to benefit from the optimized simulated filter structures.

The second approach implies the embedding of upconverter material directly in the photonic structure. This causes two different effects: first, the local irradiance can be significantly enhanced within the photonic structure; second, a variation of the local density of states alters the probability for spontaneous emission processes. These two effects were quantified by simulations and taken into account in a rate-equation model for the upconverter β-$NaYF_4$:20 % Er^{3+}. Using this simulation method, the structure parameters could be optimized within certain limits to increase the effect on the upconversion quantum yield and luminescence. In this context four different structures were investigated. First, a cavity-structure in which a rear-reflector increases the local irradiance and the most dominant upconversion emission at a wavelength of 980 nm is enhanced due to a resonance in the cavity. The main disadvantage of this structure is that the amount of upconverter material is given by the cavity thickness. The second approach, which could circumvent this problem was to embed the upconverter directly into an interdigitated Bragg-structure where the emission is enhanced due to a second reflectance peak close to the emission frequency. After a first optimization, it was found that the optimized structure hardly influenced the emission. Thus, it would be sufficient to embed the upconverter into a simple Bragg-structure instead of the more complex interdigitated Bragg. A further approach to increase the effect on the emission might be to change the high-index material used for this approach. During this work, we assumed a rather low-index TiO_2 as the high-index material. A higher-index material could improve the effects. The third structure investigated was a linear grating structure on a reflecting metallic mirror. For this structure, the three parameters: the structure height, the thickness of the underlying homogeneous layer

and the structure period, were optimized. Finally, a grating-waveguide structure was optimized. For the structures investigated in this work, the highest luminescence enhancement averaged over the structure for erbium doped β-$NaYF_4$ under an irradiance of $4337\,W/m^2$ could be obtained for the optimized grating structure where a luminescence enhancement by a factor of 3.0 could be obtained compared to the homogeneous reference. This also corresponded to the highest enhancement of the iUCQY, which was increased by a factor of 1.52 for this structure. For the optimized cavity, enhancement factors of 1.9 for the luminescence and 1.2 for the iUCQY could be achieved. For the grating-waveguide structure with air inclusions, only a luminescence enhancement by a factor of 1.2 could be achieved whereas the iUCQY is decreased by 10 %. This is due to the low quality of the waveguide. For the grating-waveguide structure with embedded higher-index material, the luminescence within the low-index layer is actually decreased by 10% and the iUCQY is decreased by 20%. Thus, this structure only makes sense if the upconverter can be embedded as higher-index material.

Two of the optimized structure types were also realized experimentally: the optimized cavity and the grating structure, as those were the most promising structures investigated in this work. The cavity filters were deposited by plasma-enhanced chemical vapor deposition of amorphous silicon carbides. The upconverter nanoparticles were embedded in polymethylmethacrylate and deposited by spin-coating. A luminescence enhancement by a factor of 1.8 could be achieved for the optimized structure. This result was also very well reproduced in simulations, which were adapted to the real deposited filter structures instead of perfectly optimized filter structures. Furthermore, the grating structure was produced experimentally. For this structure, a layer of aluminum was evaporated on glass platelets. The upconverter layer was again spin-coated on top of

this mirror. The grating structure was embossed into the spin-coated layer using a double-layer silicone stamp. For the optimized grating structures produced by this approach, a luminescence enhancement by a factor of 3.1 could be detected. Again, the trend of the various measurements on grating structures with different periods is very well reproduced by the simulations.

This is the first time that such a combined experimental and theoretical analysis was carried out on such a quantitative level taking the complete set of effects into account

In a next step, it would be very interesting to quantify the absorption of the upconverter within the various structures. This was not possible with our current setup as the sensitivity was not sufficient. With this information it would be possible to distinguish whether the luminescence enhancement is mainly due to more absorption or if it was possible to improve the upconversion quantum yield. Additionally, the predictions made by the rate-equation model for the variation of the upconversion quantum yield could be verified.

For Bragg-structures, the actual position of the reflection peak should be optimized to maximize the effect on the irradiance enhancement. Additionally, a further investigation of the interdigitated Bragg-structure would be interesting to find out, whether it is still possible to benefit from the emission enhancement if a second reflection peak is positioned perfectly. These optimized structures should then be prepared. Part of this work will be carried out in the master thesis of Clarissa Hofmann.

For the grating structures further optimization would be required, as complete calculations were only possible for a very limited amount of structures due to the high computational effort. Thus, the currently found optimum is not necessarily the best structure possible. Additionally, it the

structures should be simulated in a real three-dimensional setting. Furthermore, it would be interesting to investigate crossed gratings with the same structure period and height to see whether it is possible to further increase the effect for a two-dimensional structure.

For the grating waveguide structures, a realization of the currently optimized structures with the materials used in this work is not very promising. For the structure with air inclusions, the properties of the waveguide are not good enough and for the structure with embedded high-index material, the main effects occur in this material. This structure would become interesting again if an upconverter material with a refractive index higher than $n = 1.5$ could be used and embedded into a material with lower refractive index. In this case, the upconverter could be used as high-index material within the structure, meaning that a considerable improvement could be achieved.

Using this approach, the upconversion luminescence from thin layers can be considerably improved. If upconverter materials could be found that are able to absorb most photons in this wavelength range in such thin layers, the combination with photonic structures could help to make upconversion a useful approach to reduce transmission losses in solar cells.

Bibliography

[1] "BP Statistical Review of World Energy June 2013" (2013). http://www.bp.com/en/global/corporate/about-bp/energy-economics/statistical-review-of-world-energy-2013.html.

[2] "The Fourth Assessment Report of the Intergovernmental Panel on Climate Change" (2013). http://www.climatechange2013.org.

[3] "World Energy Outlook 2013" (2013). http://www.iea.org.

[4] Quaschning, V. "The Sun as an Energy Source" (2003). http://www.volker-quaschning.de/articles/fundamentals1/-index.php.

[5] Burger, B. "Stromerzeugung aus Solar-und Windenergie im Jahr 2013" (2014). http://www.ise.fraunhofer.de.

[6] Würfel, P. Physik der Solarzellen. Spektrum, Akad. Verlag (2000). ISBN 978-3827405982.

[7] Shockley, W. and Queisser, H.J. "Detailed Balance Limit of Efficiency of p-n Junction Solar Cells". Journal of Applied Physics, **32** (3) (1961), 510 –519. doi:10.1063/1.1736034.

[8] Green, M.A., Emery, K., Hishikawa, Y., Warta, W., and Dunlop, E.D. "Solar cell efficiency tables (Version 43)". Progress in Photovoltaics: Research and Applications, **22** (1) (2014), 1–9. doi: 10.1002/pip.2452.

[9] Richards, B. "Enhancing the performance of silicon solar cells via the application of passive luminescence conversion layers". Solar Energy Materials & Solar Cells, **90** (15) (2006), 2329 – 2337. doi: 10.1016/j.solmat.2006.03.035.

[10] Trupke, T., Shalav, A., Richards, B., Würfel, P., and Green, M. "Efficiency enhancement of solar cells by luminescent up-conversion of sunlight". Solar Energy Materials & Solar Cells, **90** (18-19) (2006), 3327 – 3338. doi:10.1016/j.solmat.2005.09.021.

[11] Richards, B. and Shalav, A. "Enhancing the Near-Infrared Spectral Response of Silicon Optoelectronic Devices via Up-Conversion". Electron Devices, IEEE Transactions on, **54** (10) (2007), 2679 –2684. doi:10.1109/TED.2007.903197.

[12] Fischer, S., Goldschmidt, J.C., Löper, P., Bauer, G.H., Brüggemann, R., Krämer, K., Biner, D., Hermle, M., and Glunz, S.W. "Enhancement of silicon solar cell efficiency by upconversion: Optical and electrical characterization". Journal of Applied Physics, **108** (4) 044912. doi:10.1063/1.3478742.

[13] Fischer, S., Ivaturi, A., Frohlich, B., Rudiger, M., Richter, A., Kramer, K., Richards, B., and Goldschmidt, J. "Upconverter Silicon Solar Cell Devices for Efficient Utilization of Sub-Band-Gap Photons Under Concentrated Solar Radiation". Photovoltaics, IEEE Journal of, **4** (1) (2014), 183–189. doi:10.1109/JPHOTOV.2013.2282744.

[14] Hallermann, F., Goldschmidt, J.C., Fischer, S., Löper, P., and von Plessen, G. "Calculation of up-conversion photoluminescence in Er^{3+} ions near noble-metal nanoparticles". In SPIE Photonics for Solar Energy Systems III, volume 7725, pp. 77250Y–77250Y–8 (2010). doi:10.1117/12.854426.

[15] Fischer, S., Hallermann, F., Eichelkraut, T., von Plessen, G., Krämer, K.W., Biner, D., Steinkemper, H., Hermle, M., and Goldschmidt, J.C. "Plasmon enhanced upconversion luminescence near gold nanoparticles - simulation and analysis of the interactions". Optics Express, **20** (1) (2012), 271–82. doi:10.1364/OE.20.000271.

[16] Fischer, S., Hallermann, F., Eichelkraut, T., von Plessen, G., Krämer, K.W., Biner, D., Steinkemper, H., Hermle, M., and Goldschmidt, J.C. "Plasmon enhanced upconversion luminescence near gold nanoparticles; simulation and analysis of the interactions: Errata". Optics Express, **21** (9) (2013), 10606–10606. doi:10.1364/OE.21.010606.

[17] Herter, B., Wolf, S., Fischer, S., Gutmann, J., Bläsi, B., and Goldschmidt, J.C. "Increased upconversion quantum yield in photonic structures due to local field enhancement and modification of the local density of states a simulation-based analysis". Optics Express, **21** (S5) (2013), A883–A900. doi:10.1364/OE.21.00A883.

[18] Goldschmidt, J., Löper, P., and Peters, M. "Solarelement mit gesteigerter Effizienz und Verfahren zur Effizienzsteigerung" (2007). German Patent 10 2007 045 546.3.

[19] Strümpel, C., McCann, M., Beaucarne, G., Arkhipov, V., Slaoui, A., Svrcek, V., del Cañizo, C., and Tobias, I. "Modifying the solar spectrum to enhance silicon solar cell efficiency–An overview of

available materials". Solar Energy Materials & Solar Cells, **91** (4) (2007), 238 – 249. doi:DOI: 10.1016/j.solmat.2006.09.003.

[20] Bloembergen, N. "Solid State Infrared Quantum Counters". Physical Review Letters, **2** (1959), 84–85. doi:10.1103/PhysRevLett.2.84.

[21] Auzel, F. "Upconversion and Anti-Stokes Processes with f and d Ions in Solids". Chemical Reviews, **104** (1) (2004), 139–174. doi: 10.1021/cr020357g. PMID: 14719973.

[22] Pollnau, M., Gamelin, D.R., Lüthi, S.R., Güdel, H.U., and Hehlen, M.P. "Power dependence of upconversion luminescence in lanthanide and transition-metal-ion systems". Physical Review B, **61** (2000), 3337–3346. doi:10.1103/PhysRevB.61.3337.

[23] Gamelin, D. and Güdel, H. "Upconversion Processes in Transition Metal and Rare Earth Metal Systems". In H. Yersin (Editor), Transition Metal and Rare Earth Compounds, *Topics in Current Chemistry*, volume 214, pp. 1–56. Springer Berlin / Heidelberg (2001). doi:10.1007/3-540-44474-2_1.

[24] Suyver, J.F., Aebischer, A., García-Revilla, S., Gerner, P., and Güdel, H.U. "Anomalous power dependence of sensitized upconversion luminescence". Physical Review B, **71** (2005), 125123. doi: 10.1103/PhysRevB.71.125123.

[25] Förster, T. "Zwischenmolekulare Energiewanderung und Fluoreszenz". Annalen der Physik, **437** (1-2) (1948), 55–75. doi: 10.1002/andp.19484370105.

[26] Auzel, F.E. "Materials and devices using double-pumped-phosphors with energy transfer". Proceedings of the IEEE, **61** (6) (1973), 758–786. doi:10.1109/PROC.1973.9155.

[27] Hüfner, S. Optical spectra of transparent rare earth compounds. Elsevier (2012). ISBN 978-0-12-360450-7.

[28] Fischer, S., Steinkemper, H., Löper, P., Hermle, M., and Goldschmidt, J.C. "Modeling upconversion of erbium doped microcrystals based on experimentally determined Einstein coefficients". Journal of Applied Physics, **111** (1) 013109. doi:10.1063/1.3674319.

[29] Thoma, R.E., Insley, H., and Hebert, G.M. "The Sodium Fluoride-Lanthanide Trifluoride Systems". Inorganic Chemistry, **5** (7) (1966), 1222–9. doi:10.1021/ic50041a032.

[30] Krämer, K.W., Biner, D., Frei, G., Güdel, H.U., Hehlen, M.P., and Lüthi, S.R. "Hexagonal Sodium Yttrium Fluoride Based Green and Blue Emitting Upconversion Phosphors". Chemistry of Materials, **16** (7) (2004), 1244–1251. doi:10.1021/cm031124o.

[31] Snoeks, E., van den Hoven, G.N., Polman, A., Hendriksen, B., Diemeer, M.B.J., and Priolo, F. "Cooperative upconversion in erbium-implanted soda-lime silicate glass optical waveguides". Journal of the Optical Society of America B, **12** (8) (1995), 1468–1474. doi:10.1364/JOSAB.12.001468.

[32] Mertens, H. and Polman, A. "Plasmon-enhanced erbium luminescence". Applied Physic Letters, **89** (21) (2006), 211107. doi:10.1063/1.2392827.

[33] Polman, A. "Erbium implanted thin film photonic materials". Journal of Applied Physics, **82** (1) (1997), 1–39. doi:10.1063/1.366265.

[34] Wang, F. and Liu, X. "Recent advances in the chemistry of lanthanide-doped upconversion nanocrystals". Chemical Society Reviews, **38** (2009), 976–989. doi:10.1039/B809132N.

[35] Haase, M. and Schäfer, H. "Upconverting Nanoparticles". Angewandte Chemie International Edition, **50** (26) (2011), 5808–5829. doi:10.1002/anie.201005159.

[36] Stouwdam, J.W., Hebbink, G.A., Huskens, J., and van Veggel, F.C. "Lanthanide-doped nanoparticles with excellent luminescent properties in organic media". Chemistry of Materials, **15** (24) (2003), 4604–4616. doi:10.1021/cm034495d.

[37] Heer, S., Kömpe, K., Güdel, H.U., and Haase, M. "Highly Efficient Multicolour Upconversion Emission in Transparent Colloids of Lanthanide-Doped $NaYF_4$ Nanocrystals". Advanced Materials, **16** (23-24) (2004), 2102–2105. doi:10.1002/adma.200400772.

[38] Li, Z. and Zhang, Y. "An efficient and user-friendly method for the synthesis of hexagonal-phase $NaYF_4$:Yb, Er/Tm nanocrystals with controllable shape and upconversion fluorescence". Nanotechnology, **19** (34) (2008), 345606. doi:10.1088/0957-4484/19/34/345606.

[39] Wang, M., Mi, C.C., Liu, J.L., Wu, X.L., Zhang, Y.X., Hou, W., Li, F., and Xu, S.K. "One-step synthesis and characterization of water-soluble $NaYF_4$:Yb,Er/polymer nanoparticles with efficient up-conversion fluorescence". Journal of Alloys and Compounds, **485** (1-2) (2009), L24–7. doi:10.1016/j.jallcom.2009.05.138.

[40] Johnson, N.J., Sangeetha, N.M., Boyer, J.C., and van Veggel, F.C. "Facile ligand-exchange with polyvinylpyrrolidone and subsequent silica coating of hydrophobic upconverting β-NaYF4: Yb3+/Er3+ nanoparticles". Nanoscale, **2** (5) (2010), 771–777. doi:10.1039/B9NR00379G.

[41] Wang, F., Han, Y., Lim, C.S., Lu, Y., Wang, J., Xu, J., Chen, H., Zhang, C., Hong, M., and Liu, X. "Simultaneous phase and size

control of upconversion nanocrystals through lanthanide doping". Nature, **463** (7284) (2010), 1061–1065. doi:10.1038/nature08777.

[42] Martín-Rodríguez, R., Valiente, R., Pesquera, C., González, F., Blanco, C., Potin, V., and de Lucas, M.M. "Optical properties of nanocrystalline-coated Y_2O_3:Er^{3+}, Yb^{3+} obtained by mechanochemical and combustion synthesis". Journal of Luminescence, **129** (9) (2009), 1109 – 1114. doi:10.1016/j.jlumin.2009.05.012.

[43] Boyer, J.C., Johnson, N.J.J., and van Veggel, F.C.J.M. "Upconverting Lanthanide-Doped $NaYF_4$ PMMA Polymer Composites Prepared by in Situ Polymerization". Chemistry of Materials, **21** (10) (2009), 2010–2012. doi:10.1021/cm900756h.

[44] Zako, T., Nagata, H., Terada, N., Sakono, M., Soga, K., and Maeda, M. "Improvement of dispersion stability and characterization of upconversion nanophosphors covalently modified with PEG as a fluorescence bioimaging probe". Journal of Materials Science, **43** (15) (2008), 5325–5330. doi:10.1007/s10853-008-2776-x.

[45] Goldschmidt, J.C. "Novel solar cell concepts". Ph.D. Thesis, University of Konstanz, München (2010).

[46] Trupke, T., Green, M.A., and Würfel, P. "Improving solar cell efficiencies by up-conversion of sub-band-gap light". Journal of Applied Physics, **92** (7) (2002), 4117–4122. doi:10.1063/1.1505677.

[47] Johnson, C.M. and Conibeer, G.J. "Limiting efficiency of generalized realistic c-Si solar cells coupled to ideal up-converters". Journal of Applied Physics, **112** (10) (2012), 103108. doi:10.1063/1.4766386.

[48] Gibart, P., Auzel, F., Guillaume, J.C., and Zahraman, K. "Below Band-Gap IR Response of Substrate-Free GaAs Solar Cells Using

Two-Photon Up-Conversion". Japanese Journal of Applied Physics, **35** (1996), 4401–4402. doi:10.1143/JJAP.35.4401.

[49] Strümpel, C., McCann, M., del Canizo, C., Tobias, I., and Fath, P. "Erbium-doped up-converters of silicon solar cells: assessment of the potential". In 20th European Photovoltaic Solar Energy Conference and Exhibition, pp. 43–6 (2005).

[50] Goldschmidt, J.C., Löper, P., Fischer, S., Janz, S., Peters, M., Glunz, S.W., Willeke, G., Lifshitz, E., Krämer, K., and Biner, D. "Advanced Upconverter Systems with Spectral and Geometric Concentration for high Upconversion Efficiencies". In Proceedings IUMRS International Conference on Electronic Materials, pp. 307–11 (2008). doi:10.1109/COMMAD.2008.4802153.

[51] Dulkeith, E., Morteani, A.C., Niedereichholz, T., Klar, T.A., Feldmann, J., Levi, S.A., van Veggel, F.C.J.M., Reinhoudt, D.N., Möller, M., and Gittins, D.I. "Fluorescence Quenching of Dye Molecules near Gold Nanoparticles: Radiative and Nonradiative Effects". Physical Review Letters, **89** (2002), 203002. doi:10.1103/PhysRevLett.89.203002.

[52] Hallermann, F., Rockstuhl, C., Fahr, S., Seifert, G., Wackerow, S., Graener, H., Plessen, G.v., and Lederer, F. "On the use of localized plasmon polaritons in solar cells". Physica Status Solidi A: Applications and Materials Science, **205** (12) (2008), 2844–2861. doi:10.1002/pssa.200880451.

[53] Schietinger, S., Aichele, T., Wang, H.Q., Nann, T., and Benson, O. "Plasmon-Enhanced Upconversion in Single $NaYF_4$:Yb^{3+}/Er^{3+} Codoped Nanocrystals". Nano Letters, **10** (1) (2010), 134–138. doi:10.1021/nl903046r. PMID: 20020691.

[54] Paudel, H.P., Zhong, L., Bayat, K., Baroughi, M.F., Smith, S., Lin, C., Jiang, C., Berry, M.T., and May, P.S. "Enhancement of Near-Infrared-to-Visible Upconversion Luminescence Using Engineered Plasmonic Gold Surfaces". The Journal of Physical Chemistry C, **115** (39) (2011), 19028–19036. doi:10.1021/jp206053f.

[55] Verhagen, E., Kuipers, L., and Polman, A. "Enhanced nonlinear optical effects with a tapered plasmonic waveguide". Nano Letters, **7** (2) (2007), 334–337. doi:10.1021/nl062440f.

[56] Aisaka, T., Fujii, M., and Hayashi, S. "Enhancement of upconversion luminescence of Er doped Al_2O_3 films by Ag island films". Applied Physics Letters, **92** (13) 132105. doi:10.1063/1.2896303.

[57] Liu, N., Qin, W., Qin, G., Jiang, T., and Zhao, D. "Highly plasmon-enhanced upconversion emissions from Au@β-NaYF4:Yb,Tm hybrid nanostructures". Chemical Communications, **47** (2011), 7671–7673. doi:10.1039/C1CC11179E.

[58] Andriamiadamanana, C., Ferrier, A., Lombez, L., Joudrier, A.L., Naghavi, N., Ghenuche, P., Bardou, N., Pellouard, J.L., Collin, S., Pelle, F., and Guillemoles, J.F. "Plasmonic enhancement of up-conversion in ultrathin layers". In SPIE Physics, Simulation, and Photonic Engineering of Photovoltaic Devices, volume 8256, pp. 825608–825608–8 (2012). doi:10.1117/12.908541.

[59] Mertens, H., Koenderink, A.F., and Polman, A. "Plasmon-enhanced luminescence near noble-metal nanospheres: Comparison of exact theory and an improved Gersten and Nitzan model". Physical Review B, **76** (2007), 115123. doi:10.1103/PhysRevB.76.115123.

[60] Baba, T. "Slow light in photonic crystals". Nature Photonics, **2** (8) (2008), 465–473. doi:10.1038/nphoton.2008.146.

[61] Krauss, T.F. "Slow light in photonic crystal waveguides". Journal of Physics D: Applied Physics, **40** (9) (2007), 2666. doi:10.1088/0022-3727/40/9/S07.

[62] Dereux, A., Girard, C., and Weeber, J.C. "Theoretical principles of near-field optical microscopies and spectroscopies". The Journal of Chemical Physics, **112** (2000), 7775. doi:10.1063/1.481383.

[63] Joulain, K., Carminati, R., Mulet, J.P., and Greffet, J.J. "Definition and measurement of the local density of electromagnetic states close to an interface". Physical Review B, **68** (2003), 245405. doi:10.1103/PhysRevB.68.245405.

[64] de Abajo, F.G. and Kociak, M. "Probing the photonic local density of states with electron energy loss spectroscopy". Physical Review Letters, **100** (10) (2008), 106804. doi:10.1103/PhysRevLett.100.106804.

[65] Herter, B., Wolf, S., Fischer, S., Peters, M., Bläsi, B., and Goldschmidt, J. "Effects of photonic structures on upconversion". In SPIE Photonics Europe, pp. 84381D–84381D. International Society for Optics and Photonics (2012). doi:10.1117/12.922490.

[66] Wolf, S., Herter, B., Fischer, S., Höhn, O., Martín-Rodríguez, R., Aeberhard, U., and Goldschmidt, J. "Exploiting Photonic Structures to improve the Efficiency of Upconversion by Field Enhancement and a Modification of the Local Density of Photonic States". In 27th European Photovoltaic Solar Energy Conference and Exhibition. Frankfurt (2012). doi:10.4229/27thEUPVSEC2012-1AO.8.3.

[67] Goldschmidt, J.C., Fischer, S., Steinkemper, H., Herter, B., Rist, T., Wolf, S., Blasi, B., Hallermann, F., von Plessen, G., Kramer, K.W.,

Biner, D., and Hermle, M. "Increasing upconversion by metal and dielectric nanostructures". In SPIE Physics, Simulation, and Photonic Engineering of Photovoltaic Devices, volume 8256, pp. 825602–1–9 (2012). doi:10.1117/12.910915.

[68] Herter, B., Wolf, S., Fischer, S., Gutmann, J., Bläsi, B., and Goldschmidt, J. "Photonic structures for enhanced upconversion". In SPIE Solar Energy+ Technology, pp. 88240A–88240A. International Society for Optics and Photonics (2013). doi:10.1117/12.2023845.

[69] Liscidini, M. and Andreani, L.C. "Highly efficient second-harmonic generation in doubly resonant planar microcavities". Applied Physics Letters, **85** (11) (2004), 1883–1885. doi:10.1063/1.1786657.

[70] Rodriguez, A., Soljacic, M., Joannopoulos, J.D., and Johnson, S.G. "$\chi(2)$ and $\chi(3)$ harmonic generation at a critical power in inhomogeneous doublyresonant cavities". Optics Express, **15** (12) (2007), 7303–7318. doi:10.1364/OE.15.007303.

[71] Hayat, A. and Orenstein, M. "Photon conversion processes in dispersive microcavities: Quantum-field model". Physical Review A, **77** (2008), 013830. doi:10.1103/PhysRevA.77.013830.

[72] Rivoire, K., Lin, Z., Hatami, F., Masselink, W.T., and Vučković, J. "Second harmonic generation in gallium phosphide photonic crystal nanocavities with ultralow continuous wave pump power". Optics Express, **17** (25) (2009), 22609–22615. doi:10.1364/OE.17.022609.

[73] Rivoire, K., Buckley, S., and Vuckovic, J. "Multiply resonant photonic crystal nanocavities for nonlinear frequency conversion". Optics Express, **19** (22) (2011), 22198–22207. doi:10.1364/OE.19.022198.

[74] Johnson, C.M., Reece, P.J., and Conibeer, G.J. "Slow-light-enhanced upconversion for photovoltaic applications in one-dimensional photonic crystals". Optics Letters, **36** (20) (2011), 3990–3992. doi:10.1364/OL.36.003990.

[75] Johnson, C., Reece, P., and Conibeer, G. "Theoretical and experimental evaluation of silicon photonic structures for enhanced erbium up-conversion luminescence". Solar Energy Materials & Solar Cells, **112** (0) (2013), 168 – 181. doi:10.1016/j.solmat.2013.01.026.

[76] Yang, Z., Zhu, K., Song, Z., Zhou, D., Yin, Z., and Qiu, J. "Effect of photonic bandgap on upconversion emission in $YbPO_4$:Er inverse opal photonic crystals". Applied Optics, **50** (3) (2011), 287–290. doi:10.1364/AO.50.000287.

[77] Niu, W., Su, L.T., Chen, R., Chen, H., Wang, Y., Palaniappan, A., Sun, H., and Yoong Tok, A.I. "3-Dimensional photonic crystal surface enhanced upconversion emission for improved near-infrared photoresponse". Nanoscale, **6** (2014), 817–824. doi:10.1039/C3NR04884E.

[78] de Dood, M.J.A., Knoester, J., Tip, A., and Polman, A. "Förster transfer and the local optical density of states in erbium-doped silica". Physical Review B, **71** (2005), 115102. doi:10.1103/PhysRevB.71.115102.

[79] Blum, C., Zijlstra, N., Lagendijk, A., Wubs, M., Mosk, A.P., Subramaniam, V., and Vos, W.L. "Nanophotonic Control of the Förster Resonance Energy Transfer Efficiency". Physical Review Letters, **109** (2012), 203601. doi:10.1103/PhysRevLett.109.203601.

[80] Andrew, P. and Barnes, W.L. "Förster Energy Transfer in an Optical

Microcavity". Science, **290** (5492) (2000), 785–788. doi:10.1126/science.290.5492.785.

[81] Joannopoulos, J.D., Johnson, S.G., Winn, J.N., and Meade, R.D. Photonic Crystals: Molding the Flow of Light. Princeton University Press, 2nd edition (2008). ISBN 978-0691124568.

[82] Einstein, A. "Zur Quantentheorie der Strahlung". Physikalische Zeitschrift, **18** (1917), 121–128.

[83] Demtröder, W. Experimentalphysik 3 Atome, Moleküle und Festkörper. Springer-Verlag Berlin (2005). ISBN 978-3642039102.

[84] Haken, H. and Wolf, H.C. Molekülphysik und Quantenchemie-Einführung in die experimentellenund theoretischen Grundlagen. Springer-Verlag Berlin, Heidelberg, New York (1994). ISBN 978-3540303145.

[85] Fox, M. Quantum Optics. Oxford University Press (2006). ISBN 978-0198566731.

[86] Loudon, R. The Quantum Theory of Light. Oxford University Press, 3rd edition (2000). ISBN 978-0198501763.

[87] Rayleigh, L. "XXVI. On the remarkable phenomenon of crystalline reflexion described by Prof. Stokes". Philosophical Magazine Series 5, **26** (160) (1888), 256–265. doi:10.1080/14786448808628259.

[88] Purcell, E.M. "Spontaneous emission probabilities at radio frequencies". Physical Review, **69** (1946), 681+. doi:10.1103/physrev.69.37.

[89] Bykov, V. "Spontaneous emission in a periodic structure". Soviet Journal of Experimental and Theoretical Physics, **35** (1972), 269.

[90] Bykov, V.P. "Spontaneous emission from a medium with a band spectrum". Soviet Journal of Quantum Electronics, **4** (7) (1975), 861. doi:10.1070/QE1975v004n07ABEH009654.

[91] Ohtaka, K. "Energy band of photons and low-energy photon diffraction". Physical Review B, **19** (10) (1979), 5057. doi:10.1103/PhysRevB.19.5057.

[92] Yablonovitch, E. "Inhibited Spontaneous Emission in Solid-State Physics and Electronics". Physical Review Letters, **58** (20) (1987), 2059–2062. doi:10.1103/PhysRevLett.58.2059.

[93] John, S. "Strong Localization of Photons in Certain Disordered Dielectric Superlattices". Physical Review Letters, **58** (23) (1987), 2486–2489. doi:10.1103/PhysRevLett.58.2486.

[94] Joannopoulos, J.D., Villeneuve, P.R., and Fan, S. "Photonic crystals: putting a new twist on light". Nature, **386** (6621) (1997), 143–149. doi:10.1038/386143a0.

[95] Joannopoulos, J., Villeneuve, P.R., and Fan, S. "Photonic crystals". Solid State Communications, **102** (2) (1997), 165–173. doi:10.1016/S0038-1098(96)00716-8.

[96] Kittel, C. Introduction to Solid State Physics. John Wiley & Sons, Ltd (2005). ISBN 978-0471415268.

[97] Krauss, T.F. and De La Rue, R.M. "Photonic crystals in the optical regime-past, present and future". Progress in Quantum Electronics, **23** (2) (1999), 51–96. doi:10.1016/S0079-6727(99)00004-X.

[98] Birner, A., Wehrspohn, R.B., Gösele, U.M., and Busch, K. "Silicon-based photonic crystals". Advanced Materials, **13** (6) (2001), 377–

388. doi:10.1002/1521-4095(200103)13:6<377::AID-ADMA377>3.0.CO;2-X.

[99] Maxwell Garnett, J. "Colours in metal glasses, in metallic films, and in metallic solutions. II". Philosophical Transactions of the Royal Society of London. Series A, Containing Papers of a Mathematical or Physical Character, **203** (1904), 385–420. doi:10.1098/rspa.1905.0039.

[100] Bruggeman, D.A.G. "Berechnung verschiedener physikalischer Konstanten von heterogenen Substanzen. I. Dielektrizitätskonstanten und Leitfähigkeiten der Mischkörper aus isotropen Substanzen". Annalen der Physik, **416** (8) (1935), 665–679. doi:10.1002/andp.19354160802.

[101] Busch, K. and John, S. "Photonic band gap formation in certain self-organizing systems". Physical Review E, **58** (3) (1998), 3896–3908. doi:10.1103/PhysRevE.58.3896.

[102] Klingshirn, C.F. Maxwell's Equations, Photons and the Density of States. Graduate Texts in Physics. Springer Berlin Heidelberg (2012). ISBN 978-3-642-28361-1. doi:10.1007/978-3-642-28362-8_2.

[103] Barnett, S.M. and Loudon, R. "Sum Rule for Modified Spontaneous Emission Rates". Physical Review Letters, **77** (1996), 2444–2446. doi:10.1103/PhysRevLett.77.2444.

[104] Barnett, S.M. and Loudon, R. "Sum rule for environmentally modified spontaneous emission rates". Quantum and Semiclassical Optics: Journal of the European Optical Society Part B, **10** (4) (1998), 591. doi:10.1088/1355-5111/10/4/002.

[105] Dirac, P.A. "The quantum theory of the emission and absorption of radiation". Proceedings of the Royal Society of London. Series A, Containing Papers of a Mathematical and Physical Character, **114** (767) (1927), 243–265. doi:10.1098/rspa.1927.0039.

[106] John, S. and Quang, T. "Spontaneous emission near the edge of a photonic band gap". Physical Review A, **50** (2) (1994), 1764–1769. doi:10.1103/PhysRevA.50.1764.

[107] Epstein, L. "The design of optical filters". Journal of the Optical Society of America, **42** (11) (1952), 806–808. doi:10.1364/JOSA.42.000806.

[108] Aguayo-Ríos, F., Villa-Villa, F., and Gaspar-Armenta, J. "One-dimensional photonic crystals of inhomogeneous thin films: band structure of rugate filters". Optics Communications, **244** (1) (2005), 259–267. doi:10.1016/j.optcom.2004.09.043.

[109] Ishikura, N., Fujii, M., Nishida, K., Hayashi, S., Diener, J., Mizuhata, M., and Deki, S. "Broadband Rugate filters based on porous silicon". Optical Materials, **31** (1) (2008), 102–105. doi:10.1016/j.optmat.2008.01.016.

[110] Yablonovitch, E., Gmitter, T., Meade, R., Rappe, A., Brommer, K., and Joannopoulos, J. "Donor and acceptor modes in photonic band structure". Physical Review Letters, **67** (24) (1991), 3380. doi:10.1103/PhysRevLett.67.3380.

[111] Meade, R.D., Brommer, K.D., Rappe, A.M., and Joannopoulos, J. "Existence of a photonic band gap in two dimensions". Applied Physics Letters, **61** (4) (1992), 495–497. doi:10.1063/1.107868.

[112] Anderson, C.M. and Giapis, K.P. "Larger two-dimensional photonic band gaps". Physical Review Letters, **77** (14) (1996), 2949. doi: 10.1103/PhysRevLett.77.2949.

[113] Lin, S.y., Fleming, J., Hetherington, D., Smith, B., Biswas, R., Ho, K., Sigalas, M., Zubrzycki, W., Kurtz, S., and Bur, J. "A three-dimensional photonic crystal operating at infrared wavelengths". Nature, **394** (6690) (1998), 251–253. doi:10.1038/28343.

[114] Fleming, J.G. and Lin, S.Y. "Three-dimensional photonic crystal with a stop band from 1.35 to 1.95μm". Optics Letters, **24** (1) (1999), 49–51. doi:10.1364/OL.24.000049.

[115] Jiang, P., Ostojic, G.N., Narat, R., Mittleman, D.M., and Colvin, V.L. "The fabrication and bandgap engineering of photonic multilayers". Advanced Materials, **13** (6) (2001), 389–393. doi:10.1002/1521-4095(200103)13:6<389::AID-ADMA389>3.0.CO;2-L.

[116] Hwang, J.K., Ryu, H.Y., and Lee, Y.H. "Spontaneous emission rate of an electric dipole in a general microcavity". Physical Review B, **60** (1999), 4688–4695. doi:10.1103/PhysRevB.60.4688.

[117] Dowling, J.P. and Bowden, C.M. "Atomic emission rates in inhomogeneous media with applications to photonic band structures". Physical Review A, **46** (1992), 612–622. doi:10.1103/PhysRevA.46.612.

[118] Sprik, R., van Tiggelen, B.A., and Lagendijk, A. "Optical emission in periodic dielectrics". Europhysics Letters, **35** (4) (1996), 265. doi:10.1209/epl/i1996-00564-y.

[119] Enoch, S., Gralak, B., and Tayeb, G. "Enhanced emission with angular confinement from photonic crystals". Applied Physics Letters, **81** (9) (2002), 1588–1590. doi:10.1063/1.1504166.

[120] John, S. and Wang, J. "Quantum electrodynamics near a photonic band gap: Photon bound states and dressed atoms". Physical Review Letters, **64** (20) (1990), 2418. doi:10.1103/PhysRevLett.64.2418.

[121] Hermann, C. and Hess, O. "Modified spontaneous-emission rate in an inverted-opal structure with complete photonic bandgap". Journal of the Optical Society of America B, **19** (12) (2002), 3013–3018. doi:10.1364/JOSAB.19.003013.

[122] Noda, S., Fujita, M., and Asano, T. "Spontaneous-emission control by photonic crystals and nanocavities". Nature Photonics, **1** (8) (2007), 449–458. doi:10.1038/nphoton.2007.141.

[123] Englund, D., Fattal, D., Waks, E., Solomon, G., Zhang, B., Nakaoka, T., Arakawa, Y., Yamamoto, Y., and Vuckovic, J. "Controlling the Spontaneous Emission Rate of Single Quantum Dots in a Two-Dimensional Photonic Crystal". Physical Review Letters, **95** (2005), 013904. doi:10.1103/PhysRevLett.95.013904.

[124] Schubert, E.F., Vredenberg, A.M., Hunt, N.E.J., Wong, Y.H., Becker, P.C., Poate, J.M., Jacobson, D.C., Feldman, L.C., and Zydzik, G.J. "Giant enhancement of luminescence intensity in Er-doped Si/SiO_2 resonant cavities". Applied Physics Letters, **61** (12) (1992), 1381 –1383. doi:10.1063/1.107544.

[125] Lopez, H.A. and Fauchet, P.M. "Erbium emission from porous silicon one-dimensional photonic band gap structures". Applied Physics Letters, **77** (23) (2000), 3704 –3706. doi:10.1063/1.1331082.

[126] Gaponenko, S., Bogomolov, V., Petrov, E., Kapitonov, A., Yarotsky, D., Kalosha, I., Eychmueller, A., Rogach, A., McGilp, J., Woggon, U., and Gindele, F. "Spontaneous emission of dye molecules, semiconductor nanocrystals, and rare-earth ions in opal-based photonic

crystals". Journal of Lightwave Technology, **17** (11) (1999), 2128 –2137. doi:10.1109/50.803003.

[127] Romanov, S.G., Fokin, A.V., and Rue, R.M.D.L. "Eu^{3+} emission in an anisotropic photonic band gap environment". Applied Physics Letters, **76** (13) (2000), 1656–1658. doi:10.1063/1.126126.

[128] Lodahl, P., Floris van Driel, A., Nikolaev, I.S., Irman, A., Overgaag, K., Vanmaekelbergh, D., and Vos, W.L. "Controlling the dynamics of spontaneous emission from quantum dots by photonic crystals". Nature, **430** (7000) (2004), 654–657. doi:10.1038/nature02772.

[129] Zhang, F., Deng, Y., Shi, Y., Zhang, R., and Zhao, D. "Photoluminescence modification in upconversion rare-earth fluoride nanocrystal array constructed photonic crystals". Journal of Materials Chemistry, **20** (2010), 3895–3900. doi:10.1039/C000379D.

[130] Wolf, S. "Photonische Strukturen zur Effizienzsteigerung der Hochkonversion". Diploma Thesis, University of Freiburg (2012).

[131] Macleod, H.A. Thin-film optical filters. Taylor & Francis, 4th edition (2010). ISBN 978-1420073027.

[132] Haupt, R.L. and Haupt, S.E. Practical Genetic Algorithms. Wiley-Interscience, 2 edition (2004). ISBN 978-0471188735.

[133] Li, L. "Formulation and comparison of two recursive matrix algorithms for modeling layered diffraction gratings". Journal of the Optical Society of America A, **13** (5) (1996), 1024–1035. doi: 10.1364/JOSAA.13.001024.

[134] Whittaker, D.M. and Culshaw, I.S. "Scattering-matrix treatment of patterned multilayer photonic structures". Physical Review B, **60** (1999), 2610–2618. doi:10.1103/PhysRevB.60.2610.

[135] Bödicker, F.M.J. "Modellierung des strahlenden Emissionsverhaltens in einer photonischen Solarzelle". Bachelor's Thesis, Technical University Darmstadt (2012).

[136] John W. Eaton, D. and Søren Hauberg. GNU Octave Manual Version 3. Network Theory Limited (2008). ISBN 978-0954612061.

[137] Octave community. "GNU/Octave" (2013). http://www.gnu.org/-software/octave/.

[138] Nikolaev, I.S., Vos, W.L., and Koenderink, A.F. "Accurate calculation of the local density of optical states in inverse-opal photonic crystals". Journal of the Optical Society of America B, **26** (5) (2009), 987–997. doi:10.1364/JOSAB.26.000987.

[139] Johnson, S.G. and Joannopoulos, J.D. "Block-iterative frequency-domain methods for Maxwell's equations in a planewave basis". Optics Express, **8** (3) (2001), 173–190. doi:10.1364/OE.8.000173.

[140] Burckhardt, C.B. "Diffraction of a Plane Wave at a Sinusoidally Stratified Dielectric Grating". Journal of the Optical Society of America, **56** (11) (1966), 1502–1508. doi:10.1364/JOSA.56.001502.

[141] Kogelnik, H. "Coupled Wave Theory for Thick Hologram Gratings". Bell System Technical Journal, **48** (9) (1969), 2909–2947. doi:10.1002/j.1538-7305.1969.tb01198.x.

[142] Moharam, M.G. and Gaylord, T.K. "Diffraction analysis of dielectric surface-relief gratings". Journal of the Optical Society of America, **72** (10) (1982), 1385–1392. doi:10.1364/JOSA.72.001385.

[143] Moharam, M.G., Grann, E.B., Pommet, D.A., and Gaylord, T.K. "Formulation for stable and efficient implementation of the rigorous coupled-wave analysis of binary gratings". Journal of the

Optical Society of America A, **12** (5) (1995), 1068–1076. doi: 10.1364/JOSAA.12.001068.

[144] Bräuer, R. and Bryngdahl, O. "Electromagnetic diffraction analysis of two-dimensional gratings". Optics Communications, **100** (1-4) (1993), 1 – 5. doi:10.1016/0030-4018(93)90546-H.

[145] Lalanne, P. and Jurek, M.P. "Computation of the near-field pattern with the coupled-wave method for transverse magnetic polarization". Journal of Modern Optics, **45** (7) (1998), 1357–1374. doi:10.1080/09500349808230634.

[146] Bläsi, B. "Holographisch hergestellte Antireflexoberflächen für solare und visuelle Anwendungen". Ph.D. Thesis, University of Freiburg (2000).

[147] Peters, M. "Photonic Concepts for Solar Cells". Ph.D. Thesis, University of Freiburg (2009).

[148] Hugonin, J. and Lalanne, P. "RETICOLO CODE 2D for the diffraction by stacks of lamellar 2D crossed gratings". Technical report, Institut d'Optique, Orsay (2004).

[149] Yee, K. "Numerical solution of initial boundary value problems involving maxwell's equations in isotropic media". Antennas and Propagation, IEEE Transactions on, **14** (3) (1966), 302 –307. doi: 10.1109/TAP.1966.1138693.

[150] Taflove, A. and Hagness, S.C. Computational Electrodynamics: The Finite-Difference Time-Domain Method. Artech House, Norwood, MA (1995). ISBN 978-1580538329.

[151] Berenger, J.P. "A perfectly matched layer for the absorption of electromagnetic waves". Journal of Computational Physics, **114** (2) (1994), 185 – 200. doi:10.1006/jcph.1994.1159.

[152] Katz, D., Thiele, E., and Taflove, A. "Validation and extension to three dimensions of the Berenger PML absorbing boundary condition for FD-TD meshes". Microwave and Guided Wave Letters, IEEE, **4** (8) (1994), 268–270. doi:10.1109/75.311494.

[153] Oskooi, A.F., Roundy, D., Ibanescu, M., Bermel, P., Joannopoulos, J., and Johnson, S.G. "Meep: A flexible free-software package for electromagnetic simulations by the FDTD method". Computer Physics Communications, **181** (3) (2010), 687 – 702. doi:10.1016/j.cpc.2009.11.008.

[154] Bermel, P., Rodriguez, A., Joannopoulos, J.D., and Soljacic, M. "Tailoring Optical Nonlinearities via the Purcell Effect". Physical Review Letters, **99** (2007), 053601. doi:10.1103/PhysRevLett.99.053601.

[155] Bullot, J. and Schmidt, M.P. "Physics of Amorphous Silicon-Carbon Alloys". Physica Status Solidi B, **143** (2) (1987), 345–418. doi:10.1002/pssb.2221430202.

[156] Drevillon, B. "A spectroscopic ellipsometry study of the nucleation and growth of plasma-deposited amorphous silicon". Thin Solid Films, **130** (1-2) (1985), 165 – 170. doi:10.1016/0040-6090(85)90305-0.

[157] Sussmann, R. and Ogden, R. "Photoluminescence and optical properties of plasma-deposited amorphous Si_xC_{1-x} alloys". Philosophical Magazine Part B, **44** (1981), 137–158. doi:10.1080/01418638108222373.

[158] Jones, A.C. and Hitchman, M.L. (Editors). Chemical Vapour Deposition. The Royal Society of Chemistry (2009). ISBN 978-0-85404-465-8. doi:10.1039/9781847558794.

[159] Pascual, E., Andújar, J.L., Fernández, J.L., and Bertran, E. "Optical and structural characterization of hydrogenated amorphous silicon carbide thin films prepared by r.f. plasma chemical vapour deposition". Diamond and Related Materials, **4** (10) (1995), 1205 – 1209. doi:10.1016/0925-9635(95)00296-0.

[160] Petrich, M.A., Gleason, K.K., and Reimer, J.A. "Structure and properties of amorphous hydrogenated silicon carbide". Physical Review B, **36** (18) (1987), 9722–9731. doi:10.1103/PhysRevB.36.9722.

[161] Sah, W.J., Tsai, H.K., and Lee, S.C. "Physical and electronic structure of amorphous silicon carbon hydrogen alloy". Applied Physics Letters, **54** (7) (1989), 617 –619. doi:10.1063/1.100896.

[162] Janz, S., Peters, M., Künle, M., Gradmann, R., and Suwito, D. "Amorphous SiC layers for electrically conductive Rugate filters in silicon based solar cells". In SPIE Photonics for Solar Energy Systems III, volume 7725, pp. 77250I–77250I–8 (2010). doi:10.1117/12.854351.

[163] McCurdy, P.R., Truitt, J.M., and Fisher, E.R. "Pulsed and continuous wave plasma deposition of amorphous, hydrogenated silicon carbide from SiH_4/CH_4 plasmas". Journal of Vacuum Science & Technology A, **17** (5) (1999), 2475–2484. doi:10.1116/1.582105.

[164] Herter, B., Peters, M., Janz, S., Hermle, M., and Goldschmidt, J. "One-Dimensional SiC Photonic Structures to Enhance the Efficiency of Systems with Silicon Solar Cells and Upconverters". In

26th European Photovoltaic Solar Energy Conference and Exhibition, pp. 349–352 (2011). doi:10.4229/26thEUPVSEC2011-1DV.1.2.

[165] Mortimer, C.E. and Müller, U. Chemie Das Basiswissen der Chemie. Georg Thieme Verlag, 8 edition (2003). ISBN 978-3134843118.

[166] Biros, J., Larina, T., Trekoval, J., and Pouchly, J. "Dependence of the glass transition temperature of poly (methyl methacrylates) on their tacticity". Colloid and Polymer Science, **260** (1) (1982), 27–30. doi:10.1007/BF01447672.

[167] Mark, J.E. (Editor). Polymer Data Handbook. Oxford University (1999). ISBN 978-0195181012.

[168] Shin, H.S., Jung, Y.M., Oh, T.Y., Chang, T., Kim, S.B., Lee, D.H., and Noda, I. "Glass Transition Temperature and Conformational Changes of Poly(methyl methacrylate) Thin Films Determined by a Two-Dimensional Map Representation of Temperature-Dependent Reflection and Absorption FTIR Spectra". Langmuir, **18** (15) (2002), 5953–5958. doi:10.1021/la020258y.

[169] Walsh, C.B. and Franses, E.I. "Ultrathin PMMA films spin-coated from toluene solutions". Thin Solid Films, **429** (1-2) (2003), 71–76. doi:10.1016/S0040-6090(03)00031-2.

[170] Zhu, X., Liu, G., Guo, Y., and Tian, Y. "Study of PMMA thermal bonding". Microsystem Technologies, **13** (3-4) (2007), 403–407. doi:10.1007/s00542-006-0224-x.

[171] Odom, T.W., Love, J.C., Wolfe, D.B., Paul, K.E., and Whitesides, G.M. "Improved pattern transfer in soft lithography using composite stamps". Langmuir, **18** (13) (2002), 5314–5320. doi:10.1021/la020169l.

[172] Jellison, G.E. and Modine, F.A. "Parameterization of the optical functions of amorphous materials in the interband region". Applied Physics Letters, **69** (3) (1996), 371 –373. doi:10.1063/1.118064.

[173] Jellison, G.E. and Modine, F.A. "Erratum: "Parameterization of the optical functions of amorphous materials in the interband region" [Appl. Phys. Lett. 69, 371 (1996)]". Applied Physics Letters, **69** (14) (1996), 2137–2137. doi:10.1063/1.118155.

[174] Boyer, J.C. and van Veggel, F.C.J.M. "Absolute quantum yield measurements of colloidal $NaYF_4$: Er^{3+}, Yb^{3+} upconverting nanoparticles". Nanoscale, **2** (2010), –. doi:10.1039/C0NR00253D.

[175] Nishii, J., Kintaka, K., and Nakazawa, T. "High-Efficiency Transmission Gratings Buried in a Fused-SiO_2 Glass Plate". Applied Optics, **43** (6) (2004), 1327–1330. doi:10.1364/AO.43.001327.

[176] Wang, S.S. and Magnusson, R. "Multilayer waveguide-grating filters". Applied Optics, **34** (14) (1995), 2414–2420. doi:10.1364/AO.34.002414.

[177] Suwito, D. "Intrinsic and doped amorphous silicon carbide films for the surface passivation of silicon solar cells". Ph.D. Thesis, University of Konstanz (2011).

[178] Ferlauto, A.S., Ferreira, G.M., Pearce, J.M., Wronski, C.R., Collins, R.W., Deng, X., and Ganguly, G. "Analytical model for the optical functions of amorphous semiconductors from the near-infrared to ultraviolet: Applications in thin film photovoltaics". Journal of Applied Physics, **92** (5) (2002), 2424–2436. doi:10.1063/1.1497462.

[179] Polyanskiy, M.N. "Refractive index database" (2014). http://refractiveindex.info.

[180] Forberich, K., Gombert, A., Pereira, S., Crewett, J., Lemmer, U., Diem, M., and Busch, K. "Lasing mechanisms in organic photonic crystal lasers with two-dimensional distributed feedback". Journal of Applied Physics, **100** (2) 023110. doi:10.1063/1.2210589.

[181] Riechel, S., Kallinger, C., Lemmer, U., Feldmann, J., Gombert, A., Wittwer, V., and Scherf, U. "A nearly diffraction limited surface emitting conjugated polymer laser utilizing a two-dimensional photonic band structure". Applied Physics Letters, **77** (15) (2000), 2310–2312. doi:10.1063/1.1310207.

[182] Rigneault, H., Jacquier, B., Moretti, P., Jurdyc, A., Belarouci, A., Auffret, A., and Robert, S. "Optical properties of dielectric microcavities implanted with rare earth atoms". In Materials Science Forum, volume 239, pp. 717–720. Trans Tech Publ (1996). doi:10.4028/www.scientific.net/MSF.239-241.717.

[183] Lipson, M., Chen, T., Chen, K., Duan, X., and Kimerling, L. "Erbium in Si-based light confining structures". Materials Science and Engineering: B, **81** (1-3) (2001), 36–39. doi:10.1016/S0921-5107(00)00685-1.

List of Abbreviations

Acronym	Description
β-$NaYF_4$	hexagonal sodium yttrium tetrafluoride
β-$NaYF_4$:Er^{3+}	hexagonal sodium yttrium tetrafluoride doped with trivalent erbium
a-Si_xC_{1-x}:H	hydrogenated amorphous silicon carbide
AFM	atomic force microscope
BP	British petrol
CCD	charge coupled device
CH_4	methane
CO_2	carbon dioxide
CVD	chemical vapor deposition
DNA	deoxyribonucleic acid
DOS	density of states
EELS	electron energy loss spectroscopy
EMA	effective medium approximation
EQE	external quantum efficiency

Acronym	Description
Er	erbium
ESA	excited state absorption
ET	energy transfer
ETU	energy transfer upconversion
eUCQY	external upconversion quantum yield
fcc	face centered cubic
FDTD	finite-difference time-domain
FRET	Förster resonant energy transfer
FSU	Friedrich-Schiller-University
GaAs	gallium arsenide
GNU	GNU's not unix (operating system similar to unix)
HPLC	high-performance liquid chromatography
IEA	international energy agency
IR	infrared
iUCQY	internal upconversion quantum yield
LDOS	local density of states
Meep	MIT electromagnetic equation propagation
MFC	mass flow controller
MMA	methylmethacrylate
MPB	MIT photonic bands
MPR	multi-phonon relaxation
MW	microwave

Acronym	**Description**
NIR	near infrared
NMR	nuclear magnetic resonance
NP	nanoparticle
NQD	nanocrystalline quantum dot
PBC	periodic boundary conditions
PDMS	polydimethylsiloxane
PECVD	plasma-enhanced chemical vapor deposition
PEG	polyethylene glycol
PML	perfectly matched layer
PMMA	polymethylmethacrylate
PTFE	polytetrafluorethylene
PVD	physical vapor deposition
RCWA	rigorous coupled wave analysis
rf	radio frequency
RR	rear-reflector
RSS	rear-side structure
S-Matrix	scattering matrix
SC	spectral concentration
sccm	standard cubic centimeter per minute
SEM	scanning electron microscope
SiH_4	silane
SNOM	scanning near field optical microscopy
SPE	spontaneous emission
TMM	transfer matrix method

Acronym	**Description**
UC	upconversion
UCQY	upconversion quantum yield
Yb	ytterbium

List of Roman Symbols

Symbol	Unit	Description
A_{fi}	1/s	Einstein coefficient for the spontaneous emission for a transition from level f to i
Abs	1/s	absorption
B		ratio between the electric field components at boundary a and at boundary b
B_{fi}	m^3/Js^2	Einstein coefficient for the stimulated emission for a transition from level i to f
B_{if}	m^3/Js^2	Einstein coefficient for the absorption for a transition from level i to f
C	S	ratio between the magnetic field components at boundary a and the electric field component at boundary b

Symbol	Unit	Description
E	V/m	electric field component
E_0	V/m	electric field amplitude
F		fitness value for the evolutionary algorithm
F_p		normalized amplitude of mode p
I	W/m^2	irradiance
Lum	1/s	luminescence
N		complex refractive index of a medium
N_f		occupation of the final state
N_g		number of generations for the evolutionary algorithm
N_i		occupation of the initial state
S	a.u.	measured luminescence signal
T	K	absolute temperature
W	1/s	transition probability
Δt	s	time step
Δx	m	distance between lattice points (x-direction)
Δy	m	distance between lattice points (y-direction)
Δz	m	distance between lattice points (z-direction)

Symbol	Unit	Description
$\hat{M}_i$		transfer matrix
$\hat{S}^i$		scattering matrix of layer i for the scattering matrix approach
$\hat{\mathcal{M}}^i$		amplitude propagation matrix in layer i for the scattering matrix approach
$\hat{f}^i$		phase propagation matrix in layer i for the scattering matrix approach
$\mathcal{A}$		absorptance
$\mathcal{C}$	g/l	concentration
$\mathcal{E}$	J	energy
$\mathcal{R}$		reflectance
$\mathcal{T}$		transmittance
$\vec{B}$	T	magnetic induction
$\vec{D}$	C/m^3	electric displacement
$\vec{E}$	V/m	electric field strength
$\vec{H}$	A/m	magnetic field strength
$\vec{S}$	W/m^2	Poynting vector
$\vec{a}^i$		forward traveling wave in layer i for the scattering matrix approach

Symbol	Unit	Description
$\vec{b}^i$		backward traveling wave in layer i for the scattering matrix approach
$\vec{j}$	A/m^2	electric current density
$\vec{k}$	$1/m$	wave vector
$\vec{n}$		occupation vector in the rate-equation model
$\vec{r}$	m	position vector
d	m	layer thickness
f		final state
f_{BE}		occupation probability determined by the Bose-Einstein distribution
$f_{vis,NIR}$		spectral mismatch correction function
g_f		degeneracy of the final state
g_i		degeneracy of the initial state
i		intitial state
m		band index
n		real part of the refractive index of a medium
p	m	structure period
r		Fresnel reflection coefficient

Symbol	Unit	Description
s		scaling factor
t	s	time
u	J/(m^{3}Hz)	spectral energy density per volume
v	m/s	velocity
x	m	direction x in a carthesian coordinate system
y	m	direction y in a carthesian coordinate system
z	m	direction z in a carthesian coordinate system

List of Greek Symbols

Symbol	Unit	Description
Δ_{ell}		measured variable for an ellipsometry measurement describing the phase change
Φ	1/s	photon flux
Ψ_{ell}		measured variable for an ellipsometry measurement describing the amplitude ratio for *s*- and *p*-polarization
δ	m	phase thickness
ϵ		electric permittivity
ϵ_r		relative permittivity
η	S	tilted optical addmittance
η_p	S	tilted optical addmittance for p-polarization
η_s	S	tilted optical addmittance for s-polarization

Symbol	Unit	Description
γ		enhancement factor
γ_{Abs}		absorption enhancement factor
γ_{E}		irradiance enhancement factor
γ_{Lum}		luminescence enhancement factor
γ_{iUCQY}		enhancement factor of the internal upconversion quantum yield
γ_{if}		enhancement factor for the transition probability from state i to state f
λ	m	wavelength
μ_r		relative permeability
ω	1/s	angular frequency
$\overline{\gamma_{\mathrm{Abs}}}$		mean absorption enhancement factor
$\overline{\gamma_{\mathrm{E}}}$		mean irradiance enhancement factor
$\overline{\gamma_{\mathrm{Lum}}}$		mean luminescence enhancement factor
$\overline{\gamma_{\mathrm{iUCQY}}}$		mean enhancement factor of the internal upconversion quantum yield
ϕ	°	angle of incidence against the periodicity of the grating structure for RCWA-calculations

Symbol	**Unit**	**Description**
$\rho(\omega)$	$\mathrm{J/m^3}$	density of states
$\rho(\omega, \vec{r})$	$\mathrm{J/m^3}$	local density of states
ρ_Q	$\mathrm{C/m^3}$	charge density
θ	$^\circ$	polar angle

List of Natural Constants

Symbol	Value	Unit	Description
ϵ_0	$8.854 \cdot 10^{-12}$	F/m	vacuum permittivity
$\hbar$	$6.582119 \cdot 10^{-16}$	eVs	reduced Planck's constant
μ_0	$1.257 \cdot 10^{-6}$	H/m	vacuum permeability
c	$2.998 \cdot 10^{8}$	m/s	vacuum speed of light
k_B	$8.6173 \cdot 10^{-5}$	eV/K	Boltzmann constant

Publications

Journal Publications

- B. Herter, M. Peters, S. Janz, M. Hermle, J.C. Goldschmidt, *Photonic Structures for a Solar Cell Upconversion System*, **Future Photovoltaics**, 6, 55–61, **2011**
- B. Herter, S. Wolf, S. Fischer, J. Gutmann, B. Bläsi, J.C. Goldschmidt *Increased upconversion quantum yield in photonic structures due to local field enhancement and modification of the local density of states – a simulation-based analysis*, **Optics Express**, 21, A883-A900, **2013**

Conferences

- B. Herter, M. Peters, S. Janz, M. Hermle, J.C. Goldschmidt, *One-Dimensional SiC Photonic Structures to Enhance the Efficiency of Systems with Silicon Solar Cells and Upconverters*, **Proceedings of the 26th EU PVSEC**, Hamburg, Germany, **2011**
- J.C. Goldschmidt, S. Fischer, H. Steinkemper, B. Herter, T. Rist, S. Wolf, B. Bläsi, F. Hallermann, G. von Plessen, K.W. Krämer, D.

Biner, M. Hermle, *Increasing Upconversion by metal and dielectric Nanostructures*, **Proceedings of SPIE Vol 8256**, 825602, San Francisco, USA, **2012**

- B. Herter, S. Wolf, S. Fischer, M. Peters, B. Bläsi, J.C. Goldschmidt, *Effects of photonic structures on upconversion*, **Proceedings of SPIE Vol 8438**, 84381D, Brussels, Belgium, **2012**
- S. Wolf, B. Herter, S. Fischer, O. Höhn, R. Martin-Rodriguez, U. Aeberhardt, J.C. Goldschmidt, *Exploiting Photonic Structures to Improve the Efficiency of Upconversion by Field Enhancement and a Modification of the Local Density of States*, **Proceedings of the 27^{th} EU PVSEC**, Frankfurt, Germany, **2012**
- B. Herter, S. Wolf, S. Fischer, J. Gutmann, B. Bläsi, J.C. Goldschmidt, *Photonic Structures for Enhanced Upconversion*, **Proceedings of SPIE Vol 8824**, 88240A, San Diego, USA, **2013**
- J.C. Goldschmidt, U. Aberhard, R. Capek, M.G. Debije, W. Evers, S. Fischer, B. Fröhlich, M. Hermle, B. Herter, A. Ivaturi *Developing Efficient Upconverter Silicon Solar Cell Devices* **Optical Nanostructures and Advanced Materials for Photovoltaics**, PT3C.2, Tucson, USA, **2013**
- S. Fischer, B. Fröhlich, A. Ivaturi, B. Herter, S. Wolf, K.W. Krämer, B.S. Richards, J.C. Goldschmidt, *Upconverter Materials and Upconversion Solar Cell Devices: Simulation and Characterization regarding the broad Solar Spectrum*, **Proceedings of SPIE Vol 8981**, 89810B, San Francisco, USA, **2014**
- C. Hofmann, B. Herter, J. Gutmann, J. Löffler, S. Fischer, S. Wolf, R. Piper, N. Ekins-Daukes, N. Treat, J.C. Goldschmidt, *Organic Upconverters Embedded in a Bragg-Structure*, to be published, Brussels, Belgium, **2014**

- J.C. Goldschmidt, S. Fischer, B. Fröhlich, J. Gutmann, B. Herter, C. Hofmann, J. Löffler, F.C.J.M. van Veggel, S. Wolf, *Photon management with luminescent materials and photonic structures*, to be published , Brussels, Belgium, **2014**

Oral Presentations

- B. Herter, S. Wolf, S. Fischer, J. Gutmann, B. Bläsi, J.C. Goldschmidt, *Increased Upconversion Quantum Yield in Photonic Structures due to Field Enhancement and a Modification of the Local Density of States*, Talk presented at **Workshop on Advanced Systems for Photon Management for Photovoltaics**, Freiburg, Germany, **2013**

Acknowledgment

First of all, I would like to thank Prof. Dr. Gerhard Willeke for the supervision of this PhD thesis.

I am grateful to Prof. Dr. Elke Scheer for being the second assessor of this thesis.

I would like to thank Dr. Stefan W. Glunz and Dr. Martin Hermle for the opportunity to work in their division and department, respectively.

Special thanks goes to the head of our team, Dr. Jan Christoph Goldschmidt, for his feedback and support.

Special thanks also goes to my master students, Sebastian Wolf and Clarissa Hofmann, who contributed a great deal to this thesis and started a lot of interesting discussions. Furthermore, it was a great pleasure working with you.

Further, I would like to thank my colleague Stefan Fischer for his knowledge on upconversion, the rate-equation model, for the fabrication of the upconverter nanoparticles and for discussing all kinds of questions. Special thanks also goes to Johannes Gutmann for many theoretical discussions, for his support in Mathematica and Origin questions. Further, I would like to thank Johannes Eisenlohr in particular for hours we spent at the SEM trying to get good pictures and for many discussions on theoretical and

simulation-related issues. I would also like to thank Sabrina Jüchter for advice on the preparation of the grating structures, for many interesting discussions and many tea breaks that increased our productivity.

Many students contributed to this work, I would like to especially thank Aile Ge-Ernst for endless hours of PECVD and measurements. Furthermore, I would like to thank Bissera Dimitrova for her chemist's advice on a lot of questions and for spin-coating and characterization of the doped PMMA-layers. Thank you also to Viktoria Ehret for photoluminescence measurements, to Christoph Ries and Taimur Aftab for all kinds of measurements and to Anthony Kosar for proof-reading this thesis. Thanks to everyone who was part of the Novel team for the great working atmosphere. It was a great pleasure to work with each and every one of you. I would also like to thank especially, those, I shared an office with during these last years for the great working atmosphere. Furthermore, I would like to thank Stefan Janz, Bernd Steinhauser and Veit Preidel for sharing their knowledge on PECVD. Additionally, many thanks goes to Christian Schetter and Harald Steidl for technical support.

I would like to thank the whole microstructured surfaces group for a great collaboration, especially, Benedikt Bläsi for all his knowledge on wave optics and simulations. Special thanks also goes to Oliver Höhn for his knowledge on all kinds of simulation issues, which led to very interesting discussions, and for programming the evolutionary algorithm. I would further like to thank Florian Bödicker for coding the scattering matrix implementation used in this work. Further, I would like to thank Marius Peters for introducing me to the world of optical simulations. Special thanks also goes to Hubert Hauser, Nico Tucher and Patrick Schneider for the planning and the fabrication of the silicone stamp and to Moritz Pickl for the AFM measurements.

I would also like to thank our project partners in Jena, in particular

Matthias Zilk for the production of the master structure, the SEM images and for very informative discussions on the scattering matrix method.

Further, I would like to thank all project partners in the EU-project Nanospec for the great collaboration, it was a pleasure to work with you. I would like to especially mention Dr. Urs Aeberhardt, Dr. Rosa Martin-Rodriguez, Sean MacDougall, Prof. Dr. Bryce Richards, Prof. Dr. Andries Meijerink, Dr. Karl Krämer and Prof. Dr. Efrat Lifshitz.

I would also like to thank Prof. Dr. Gavin Conibeer for giving me the opportunity to work in his group in Sydney for three months, it was a great experience. In this context, I would also like to thank Craig Johnson for very interesting discussions and Pengfei Zhang and Sanghun Woo for working with me on the Langmuir-Blodgett deposition of upconverter nanoparticles.

Thanks as well to all my friends, for their support, for the distraction from work and for proof reading.

Last but not least, I would like to thank my family for their encouragement and support. Especially, I would like to thank my parents who are always there for me and who supported and encouraged my during all my studies and this thesis.